SELF-ASSEMBLY OF ORGANIC NANOSTRUCTURES

A Dissertation

by

ALBERT WAN

Submitted to the Office of Graduate Studies of
Texas A&M University
in partial fulfillment of the requirements for the degree of

DOCTOR OF PHILOSOPHY

August 2011

Major Subject: Chemistry

SELF-ASSEMBLY OF ORGANIC NANOSTRUCTURES

A Dissertation

by

ALBERT WAN

Submitted to the Office of Graduate Studies of
Texas A&M University
in partial fulfillment of the requirements for the degree of

DOCTOR OF PHILOSOPHY

Approved by:

Chair of Committee,	James D. Batteas
Committee Members,	D. Wayne Goodman
	Paul S. Cremer
	Jaime C. Grunlan
Head of Department,	David H. Russell

August 2011

Major Subject: Chemistry

ABSTRACT

Self-Assembly of Organic Nanostructures. (August 2011)

Albert Wan, B.S., National Chung-Hsing University;

M.S., National Tsing-Hua University

Chair of Advisory Committee: Dr. James D Batteas

This dissertation focuses on investigating the morphologies, optical and photoluminescence properties of porphyrin nanostructures prepared by the self-assembly method. The study is divided into three main parts. In the first part, a large variety of porphyrin nanostructures, including nanoplates, nanofibers, nanoparticles and nanowires, were obtained through direct acidification of tetra(*p*-carboxyphenyl)porphyrin (TCPP) in aqueous solution. Protonation of the carboxylate groups of TCPP resulted in the formation of nanoplates through the J-aggregation of the porphyrin. Further protonating the core nitrogens of TCPP formed the porphyrin diacids, which organized into well-defined structures through their interactions with counter-anions in the solution. The structures of the resulting assemblies were found to be counterion dependent.

In the second part of this work, we explored the optical memory effect of the porphyrin thin film. We found that the morphology and the emission of the porphyrin thin film on Si can be changed by varying the pH of its surrounding solution. The changes in morphology and light emission of the thin film resulted from the protonation or deprotonation of TCPP's core nitrogens. By selectively deprotonating the TCPP dications in a confined region utilizing the water meniscus between an AFM tip and the surface, fluorescence patterns can be generated on the thin film. The fluorescence patterns can be easily erased by re-protonating the porphyrin.

In the third part of this study, porphynoid nanoparticles were deposited on a surface energy gradient, and then characterized by AFM in order to investigate how the surface energy influences their morphologies. The surface energy gradient was prepared by selectively oxidizing a self-assembly monolayer of octadecyltrichlorosilane (OTS) by UV-ozone. The nanoparticles disassemble into smaller nanoparticles with narrower size distribution on the surface with higher surface energy. Lastly, we engaged in characterizing the morphologies of polymer nanocomposites prepared by layer-by-layer assembly for wettability control. The surface roughness of the nanocomposite in air and in salt solutions was also measured to study the correlation between the wettability of the polymer surface and its surface roughness.

ACKNOWLEDGEMENTS

I would like to thank my research advisor, Dr. James Batteas, for giving me the opportunity to join his group and teaching me for the last five years. I want to acknowledge him for supporting my research and showing great patience to help me in many ways. I also want to thank him for putting so much effort into correcting my writing. I want to thank Dr. Bergbreiter for bringing me into Texas A&M, teaching me the organic knowledge in my first year of graduate study, and providing me the opportunity to collaborate with his research group for the past three years. Thank you to my committee members, Dr. Cremer, Dr. Goodman, Dr. Liang and Dr. Grunlan for their help and advice. I would also like to thank other Faculty members in the Chemistry department, including Dr. Clearfield, Dr. Marcetta Darensbourg, Dr. North and Dr. Son for their advice and help.

Many thanks go to the former and present Batteas group members, Dr. Yang-Hsiang Chan, Dr. Jixin Chen, Dr. Liu, Dr. Hong, Dr. Liang, Ammon, Chi-yuan, Agustin, Ryan, Amanda, Brad, Arika, Carrie, Ainsley, Laura and other members for the help in lab. I want to thank my collaborators, including Shawn Liao, Hui Fu, Dr. Zhi-Ping Luo, Dr. Angel Marti, Dr. Drain, Dr. Goldberg, Daniel, Zach and Jamie. I would also like to thank many people who have helped me from other research groups in our department, including Dr. Tai-yen Chen, Jaibir, Dr. Tinglu Yang, Tzu-Pin, Iou-h, Hawlie, Jeff Yang and others.

I would like to thank my former advisors Dr. Chuin-Tih Yeh, Dr. Ru-Jen Cheng and Dr. Chung-Yuan Mou, for their support in my pursuing a Ph.D. degree in the United States.

I would like to express my deepest appreciation to my wife, Alison, for always being there to love me and support me. Without her sacrifice, I would not have reached this far and lived a balanced life. I also want to thank my parents and my family who always believe in me and encourage me. Thank you!

TABLE OF CONTENTS

Page

CHAPTER Page

LIST OF FIGURES

LIST OF TABLES

TABLE Page

CHAPTER I

INTRODUCTION

1.1. Overview

The increasing energy demand drives research efforts to focus on developing new technologies and searching alternative resources that generate environmentally clean energy. Converting sunlight to energy for daily use is desirable since the sun is a constant, viable resource and has sustained entire life systems on earth for millions of years. Solar cells convert solar radiation to electricity, but currently their market is limited by their cost. In order to lower their cost, new generation solar cells such as dye-sensitized solar cells have been developed in recent years; however, their efficiency remains low.[1-5] The dye-sensitized solar cell is based on the sensitization of highly porous TiO_2 by a monolayer of dyes. The low efficiency of the cell is mainly due to the poor light harvesting ability of the dyes.

Porphyrin is one of the candidates for sensitizing materials in dye-sensitized solar cells. Porphyrin absorbs light in the visible range and is able to efficiently transfer its excited electron.[6-10] However, the porphyrin's narrow absorption band limits the power conversion efficiency of this type of dye-sensitized solar cells.[11-15] One way to enhance the light harvesting properties of the porphyrin materials is to organize its molecules into well-ordered supramolecular structures. Supramolecular structures confine the porphyrin molecules and split their exciton energy states through dipole-dipole interactions, thus leading to a broader light absorption range.[16-25] An example of this is found in

---

This dissertation follows the style of *Journal of the American Chemical Society.*

photosynthetic bacteria. The chlorophylls in the bacteria self-organize into nanorods or ring-like arrays with proteins to improve their light harvesting ability for energy conversion in photosynthesis.[26-32]

Self-assembly provides a route to fabricate well-ordered organic materials in a cost effective way. The assembly utilizes many noncovalent interactions, including van der Waals forces, hydrogen bonding, π-π interactions, and metal-ligand coordination to assemble molecules into supramolecular structures. Self-assembly of porphyrin nanostructures has not been investigated until recent years. Although various porphyrin-based structures such as nanoparticles,[33-39] nanorods,[40-42] nanosheets,[43] and nanotubes[44,45] have been obtained, the influence of molecular arrangement on the optoelectronic properties and the morphology of the assembly is not fully understood. In fact, in most literature, there is a lack of information about the arrangement of the molecules within the porphyrin nanostructures. It is desirable to develop new methodology to assemble porphyrins into well-ordered structures with controlled shapes and sizes and to investigate the correlation between their morphologies and their chemical and physical properties. Porphyrin self-assembly may have applications in photodynamic therapy, sensors, optical devices and catalysis, as well as photovoltaic devices.

1.2. Background

The development of clean alternatives that generate energy has become an immensely important topic since the demand of global energy has increased. In the 20th century, the energy demand increased 16-fold as the population quadrupled. This exponential growth of energy demand and causes fossil fuel supply to be consumed at an alarming rate.[46,47] Currently about 13 terawatts (TW) of energy is required to sustain the lifestyle of 6.5 billion people worldwide. As more than a billion new consumers from several developing countries such as China and India emerge, an additional 10 TW of energy will be needed by the year 2050. Moreover, burning fossil fuel, presently the main route of energy production, has caused serious environmental problems. Since the beginning of the Industrial Revolution in the early 19th century, the burning of fossil fuel has increased the levels of CO_2 in the atmosphere from 280 to 390 ppm.[48-52] The large increase of CO_2 contributes to additional absorption and emission of thermal radiation (greenhouse effect) and can result in climate changes.[53-59] Therefore, the development of new technology based on clean energy generation is desirable in order to meet the growing energy demand and to reduce pollution from oil combustion.

One way to fulfill the energy demand in an environmentally friendly manner is to utilize renewable energy that is produced from clean energy sources. Renewable energy comes from natural sources, including hydropower, biofuels, wind, geothermal and sunlight. Among the different sources of renewable energy, solar energy is currently the most viable but the least utilizable choice. Solar energy provides for nature, sustains our life on earth, and in fact produces enough energy every hour to power the entire human race for a year. Although solar energy is such a great resource, the energy produced from solar power is less than 0.01% of our current total energy demand.[60] This is mainly due to the high cost of the electricity produced from photovoltaic systems. The cost of electrical power produced by photovoltaic systems is around 50 p/kWh, which is much higher than the cost of the electricity produced from fossil fuels (11 p/kWh).[61] The high cost of electricity from photovoltaic systems can be attributed to their expensive semiconducting material (silicon) and high implementation fee.

In order to lower the cost of solar cells, new types of cells such as dye-sensitized solar cells have been developed. The first dye-sensitized solar cells were designed by Grätzel *et. al*. and were based on the sensitization of highly porous TiO_2 by a monolayer of dyes.[62] To create dye-sensitized solar cells, small organic dye molecules are used as the charge donator while TiO_2 is typically used as the charge acceptor.[3,62-66] Light illumination generates electron-hole pairs (excitons) at the sensitizer layer, and then charge separation is carried out by electron transfer or energy transfer from the sensitizer to the charge acceptor (Figure 1.1). An electron can be transported by hopping from charge acceptors to an electrode to produce a current in the system. Although dye-sensitized solar cells are much cheaper than the conventional solar cells, their applications are limited by their low power conversion efficiency (η= 7-11%).[1-5,67] The efficiency of dye-sensitized solar cells can be improved by enhancing the light harvesting properties of the sensitizers. Many research groups engage in synthesizing new organic complexes or assemblies of organic molecules with broad absorption wavelength covering the spectrum of sun light.

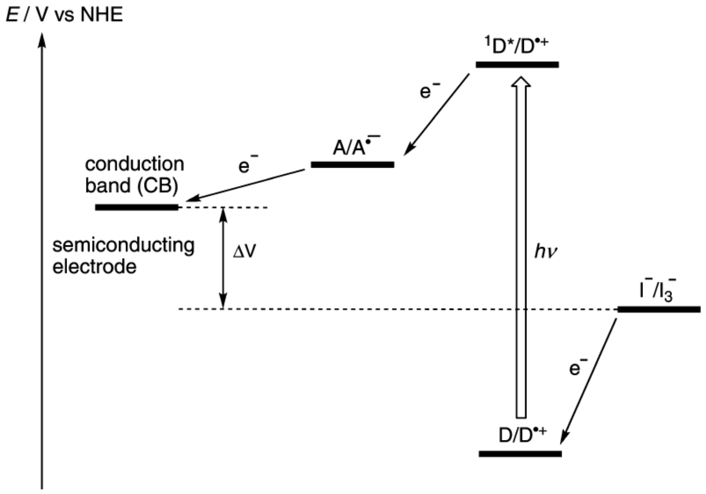

Figure 1.1 The schematic diagram illustrating the current-generation process within dye-sensitized solar cells. (Reproduced from ref. [1] with the permission of the copyright holders.)

The search for cost effective materials that fit in small electronic devices and for energy conversion has led to a major research focus on the assembly of organic nanostructures in recent years. Various intermolecular interactions such as π-π stacking, hydrogen bonding and metal-ligand coordination have been used to construct supramolecular architectures, including nanoparticles, nanorods, nanobelts, nanotubes, and nanotapes, etc.[68-74] The chemical and physical properties of molecular assemblies can be modulated by the molecular arrangement or the intermolecular interactions between the molecules. In natural photosynthetic systems, it has been discovered that chlorophylls assemble into well-ordered structures broadening their absorbing spectral range to convert sun light more efficiently to chemical energy. For example, in green photosynthetic bacteria, bacteriochlorophyll (BChl) molecules pack densely forming nanorods as the chlorosomal antennae.[27-28, 31] In purple bacteria, porphyrinoid compounds form ring-like array with protein around the photosynthesis center.[29-30, 32]

1.3. Porphyrins

Porphyrins are attractive molecular building blocks for self-assembly due to their optical, electronic, and catalytic properties.[75-78] Porphyrins absorb light in the visible light spectral range and are able to efficiently transport excitation energy. Porphyrin molecules are also active components in various biological processes. In nature, biological porphyrins are the active sites of numerous proteins, whose functions range from oxygen transfer (hemoglobin and myoglobin),[79-82] electron transfer (cytochrome c and cytochrome oxidase),[83,84] and energy conversion (chlorophyll).[26-32] They also have applications in catalysts,[85-95] sensors,[96-103] and photodynamic therapy (PDT).[104-110] The basic structure of the porphyrin macrocycle consists of a 16-atom ring containing four nitrogen atoms in the center, constructed by four pyrrolic subunits and four methine bridges, as shown in Figure 1.2. The porphyrin aromatic system contains a total of 22 π-electrons, with only 18 of them delocalized according to Hückel's rule of aromaticity. The functionality of the porphyrin can be largely changed by replacing the two hydrogens in the center of the macrocycle with various metals, or by changing its peripheral substituents.

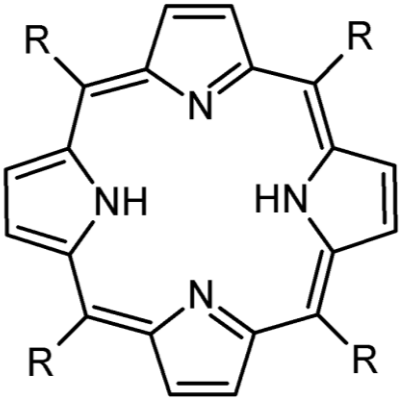

Figure 1.2. The structure of a porphyrin. R represents its peripheral substituents.

Porphyrins play a main role in photosynthetic mechanisms, and thus draw a major focus specifically on their photon-electron transfer processes. The possibility that researchers can tailor the physical and chemical properties at the molecular level involving dipole moments, polarizability, non-linear optical response, light harvesting and catalytic properties make porphyrins great candidates for extremely versatile building blocks for self-assembly. Therefore, self-assembly of porphyrin nanostructures with well-defined shapes and sizes has become a major research topic for its potential applications in optoelectronic devices, data storage, and solar cells.

The absorption spectrum of porphyrins has been intensively studied due to their importance in biological systems and their large variety of applications including photovoltaic

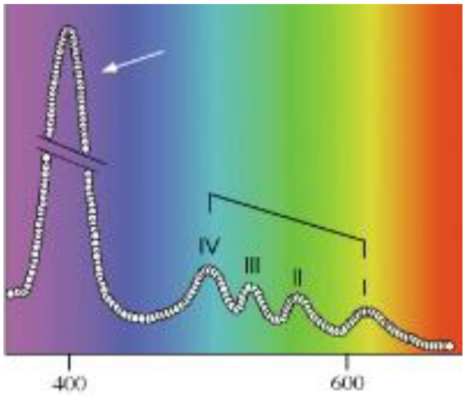

Figure 1.3. Typical UV-visible spectrum of porphyrins.

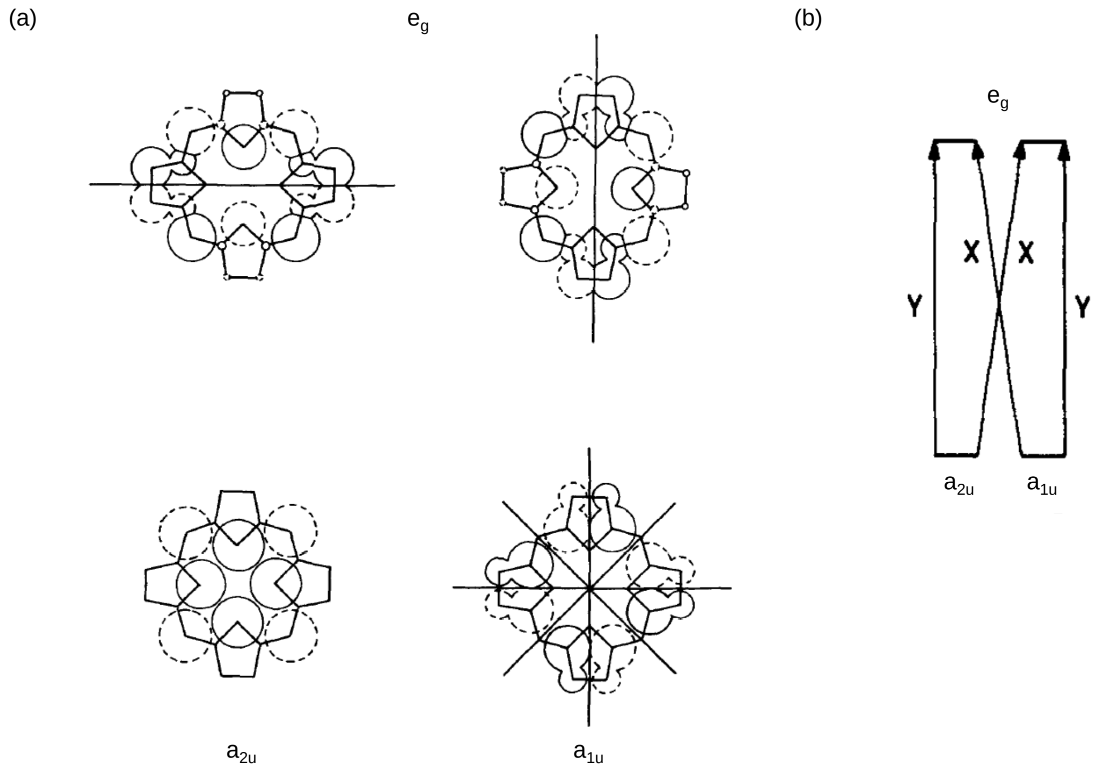

Figure 1.4. (a) The Frontier Orbitals relevant to the Gouterman Four-Orbital Model. (b) Orbital diagram illustrating possible electronic transitions of porphyrins. Note that although the HOMOs are shown to be degenerate, the actual relative energies depend on the substituents of the porphyrin rings. (Reproduced from ref. [119] with the permission of the copyright holders.)

devices, sensors, and photodynamic therapy.[111-118] The electronic absorption spectrum of the porphyrin typically consists of a strong transition in the near UV region (B band or Soret band) and multiple weak transitions within the visible regions (Q bands) (Figure 1.3).[118-121] Both the Soret band and Q bands arise from the π-π^* transitions of the frontier orbitals of the porphryin. The Soret band and Q bands result from the transitions to the second excited state ($S_0 \rightarrow S_2$) and the first excited state ($S_0 \rightarrow S_1$), respectively. The electronic transition of the porphyrin can be further explained by the four-orbital theory, which was proposed by Gouterman in the 1960s.[119,121] According to Gouterman's theory, the porphyrin absorption bands are due to the transitions between two HOMOs and two LUMOs (Figure 1.4a). Mixing can split these two states resulting in a higher energy e_{1u} state with greater oscillator strength and a lower energy e_{1u} state with less oscillator strength. The Soret band and Q bands of porphyrins attribute to the transitions from the ground state to the higher energy state, and from ground state to the lower energy state, respectively. According to group theory, the electronic transition which attributes to the Soret band is transition allowed, whereas the transition attributed to Q bands are forbidden. Therefore, the Soret band is much stronger than the Q bands in the porphyrin absorption spectrum. Moreover, the absorption spectrum of porphyrins can greatly change when a metal ion is inserted within the macrocycle, or when the core nitrogen atoms are protonated or deprotonated.

Aggregation of porphyrinoid compounds induces dipole-dipole interactions between the molecules, which typically shifts and broadens their absorption in the UV-visible (UV-vis) spectrum.[122-125] This is utilized by chlorophylls in photosynthetic bacteria as they self-organize into arrays with proteins, or self-assemble into well ordered nanostructures around the photosynthetic centers to enhance their light harvesting abilities for photon-electron energy conversion.[26-32] The changing of light absorption due to their aggregation can be explained by the exciton theory which was proposed by Kasha *et. al.*.[126] In this theory, the exciton model is defined as the treatment of the resonance interaction between excited states of weakly coupled aggregate systems. Exciton theory depends on the interactions between the excited electronic states of the molecules in a molecular aggregate. Various types of spectral effects for strong-coupling, intermediate-coupling and weak coupling excitons have been observed.

The electronic transitions dye molecule dimers have been studied by the exciton formalism by Levinson et al,[127] and their possible exciton band structures and selection rules have been proposed by Kasha *et. al.* as shown in Figure 1.5. The selection rule for the light absorption of dimers is based on criteria assuming that only in-phase arrangement of dipoles give allowed exciton states. In-phase arrangement is necessary since the wavelength of the light used for the electronic excitation of molecules is much larger than the dimensions of the ordinary molecules. Therefore, molecules of a dimer should be simultaneously under an in-phase perturbation caused by light. As a result, when two molecules form a dimer, the excited energy states of the ordinary molecules split. The newly excited energy state transition is allowed as molecules in a dimer are parallel aligned (Figure 1.5a). The new, lower excited energy state transition is allowed as molecules are head-to-tail aligned (Figure 1.5b). In the case of the oblique dimer, electronic transitions into both excited states are allowed, but the transitions are mutually perpendicular polarization for light absorption to the excited states of the dimer (Figure 1.5c). This selection rule can be applied to polymers or large aggregates which consist of multiple molecules. Typically a blue-shift and a red-shift of the electronic transition band in the absorption spectrum can be attributed to the transition of the parallel aggregation and head-to-tail aggregation of ordinary molecules, respectively. As a result, the absorption spectroscopy an important tool for understanding the arrangement of porphyrin molecules in porphyrin aggregates.

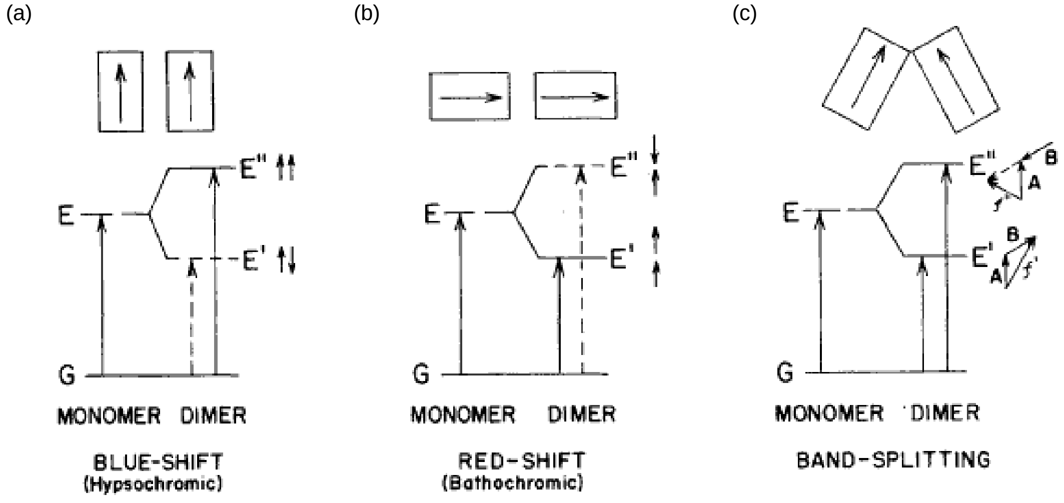

Figure 1.5. Schematic diagram for exciton band structures in molecular dimers with (a) parallel transition dipoles, (b) head-to-tail transition dipoles, (c) oblique transition dipoles. (Reproduced from ref. [126] with the permission of the copyright holders.)

1.4. Self-Assembly of Porphyrin Nanostructures

Aggregation of porphyrins enhance their light harvesting properties, however, for practical applications such as photovoltaic and optoelectronic devices, it is desirable to synthesize porphyrin supramolecular structures in a controllable manner. Self-assembly of organic nanomaterials provides a route to the fabrication of well ordered nanostructures by utilizing organic molecules as building blocks. Self-assembly, as a “bottom up” approach, can involve a range of interactions, from non-covalent such as van der Waals, electrostatic, hydrogen bonding, and hydrophobic forces, to directed covalent bonding though approaches such as metal-ligand coordination to carryout supermolecular assembly of materials. Compared to their monomers, aggregates of organic molecules may exhibit unique optical and electrical properties modulated by controlling the morphologies (size, shape) of the aggregates or by adjusting the molecular arrangement.[68,128,129] Hence research efforts are directed toward not only tuning the structures of the building blocks in order to control their interactions, but also exploring new techniques of organizing the molecules into highly ordered nanostructures.

Self-assembly of porphyrin nanostructures has drawn much interest in recent years; however, the research is still in its infancy. Along these lines there have been numerous studies of the optical and electronic properties of self-organized porphyrin nanostructures created via non-covalent molecular interactions, including nanoparticles,[33,38] nanodiscs,[130] nanorods,[40,131-133] nanowires,[134-136] nanotubes,[44,45] etc. Porphyrin nanostructures can be obtained by various approaches, such as solvent mixing techniques (with or without surfactant), vapor deposition, recrystallization, coordination polymerization and direct acidification.

Solvent mixing techniques, a reprecipitation method, is the most frequently used method to fabricate organic nanomaterials.[33, 38, 43, 136, 137] This method was first utilized by Drain *et. al.* to synthesize porphyrin nanoparticles.[33,38] Drain *et. al.* reported that both hydrophilic and hydrophobic *meso*-arylporphyrin nanoparticles were prepared with the assistance of (polyethelyen) glycol (PEG) as the stabilizing reagent (Figure 1.6a). In a typical process, the organic molecule is first dissolved in a good solvent that easily dissolves the molecules then a small amount of the solution is mixed with large amount of a bad solvent which causing the precipitation of the molecular aggregates. This allows the molecules to form suspension of the nanostructures in the mixture. Examples of porphyrin nanostructures utilizing solvent mixing techniques include porphyrin nanosheets of tin 5-(4-pyridyl)-10, 15, 20-triphenylporphyrin reported by Shelnutt *et. al.* (Figure 1.6b),[43] and hollow hexagonal nanoprisms of zinc *meso*-tetra(4-pyridyl) porphyrin [ZnT(4-Py)P] reported by Hu *et. al.* (Figure 1.6c).[137] In some instances surfactant was added in the system to modulate the sizes or shapes of the porphyrin assemblies. For example, Hupp et al reported that by tuning the ratio of an amphiphilic Sn porphyrin and a triblock copolymer Pluronic F127 used as the surfactant during the reprecipitation, the aspect ratio of the resulting porphyrin nanowires can be controlled (Figure 1.7).[136] The structures of the porphyrin assemblies are also affected by other factors such as reaction temperature, types of solvent, and the concentration of the initial porphyrin monomers.

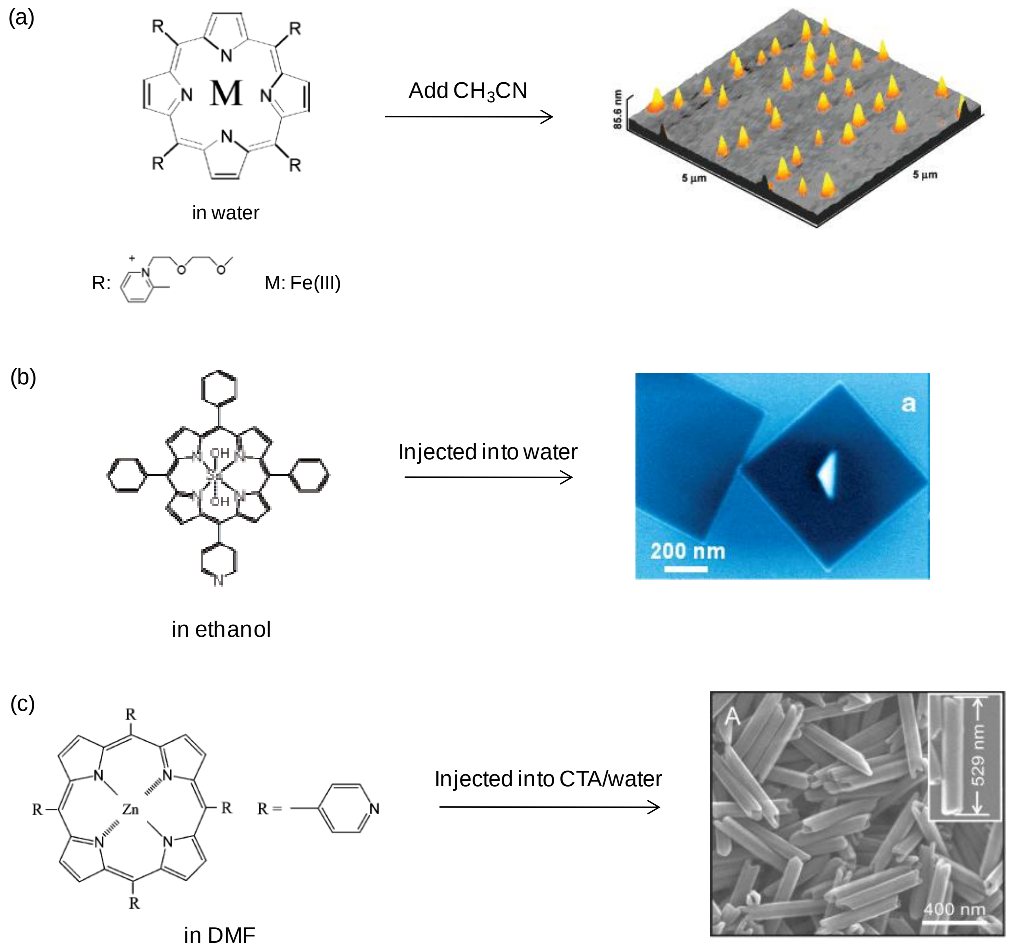

Figure 1.6. (a) The process of preparing porphyrin nanoparticles by solvent mixing method. The right panel is the AFM topographical image of nanoparticles dispersed on glass. (b) The process of preparing porphyrin nanosheets by solvent mixing method. The right panel is the SEM image of the nanosheets. (c) The process of preparing porphyrin hollow hexagonal nanoprisms by solvent mixing method. The image in the right is the SEM image of the nanoprisms. (Reproduced from ref. [137] with the permission of the copyright holders.)

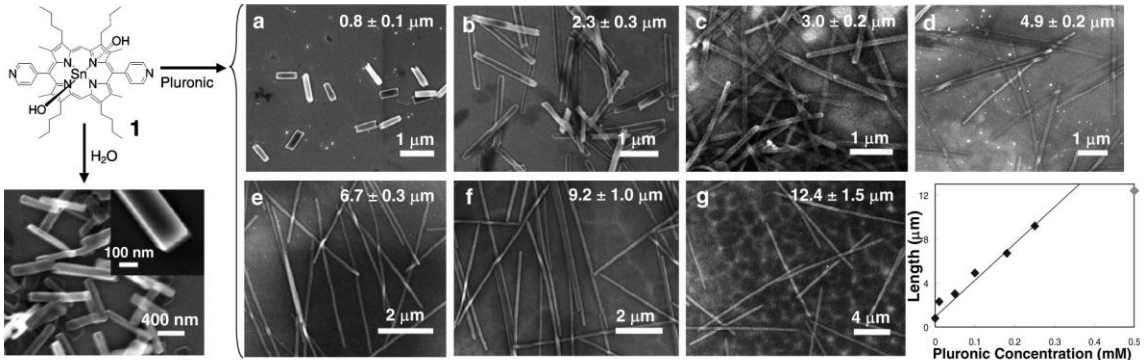

Figure 1.7. The SEM images showing the porphyrin nanowires prepared at various Pluronic concentrations. (a) 0, (b) 0.01, (c) 0.05, (d) 0.1, (e) 0.18, (f) 0.25 and (g) 0.5 mM of Pluronic F127 in water. The bottom-left panel is the SEM image of porphyrin nanorods synthesized without adding the surfactant. The bottom-right panel is a plot showing the relationship between the length of the nanowires and the Pluronic concentration. (Reproduced from ref. [136] with the permission of the copyright holders.)

Ionic self-assembly based on coupling of different ionic building blocks by electrostatic interactions was utilized by several research groups to fabricate porphyrin based materials in nanoscale or microscale.[44, 45, 138, 139] Unlike solvent mixing techniques, where single type of porphyrin is used in the reaction, ionic self-assembly typically involves porphyrin cation and porphyrin anion as the starting materials with the ionic interaction of the porphyrin ions playing a major role during the assembly process. Porphyrin nanostructures such as porphyrin nanotubes and porphyrin nanofiber bundles were prepared via ionic self-assembly, reported by Shelnutt *et. al.*. Porphyrin nanotubes can be obtained by mixing equal proportion of metal-free tetrakis(4-sulfonatophenyl)porphyrin ($H_4TPPS_4^{2-}$) and tin *meso*-tetra(4-pyridyl) porphyrin ($SnTPyP^{2+}$), in aqueous solution (Figure 1.8a).[44,45] Porphyrin nanofiber bundles were formed through mixing oxo-antimony(V) porphyrin ($SbOTPP^{+}$) and the free base or divalent metal complexes of porphyrin ($H_2TPPS_4^{-4}$) (Figure 1.8b).[138] Highly complex structures such as four-leaf clovers with micrometer-size can also be fabricated by ionic self-assembly from equal mole of zinc tetrakis(N-ethanol-4-pyridinium)porphyrin [ZnT(N-EtOH-4-Py)P^{+4}] and tin tetrakis(4-sulfonatophenyl)porphyrin [Sn(OH^-)$_2$TPPS^{-4}] (Figure 1.8c).[139]

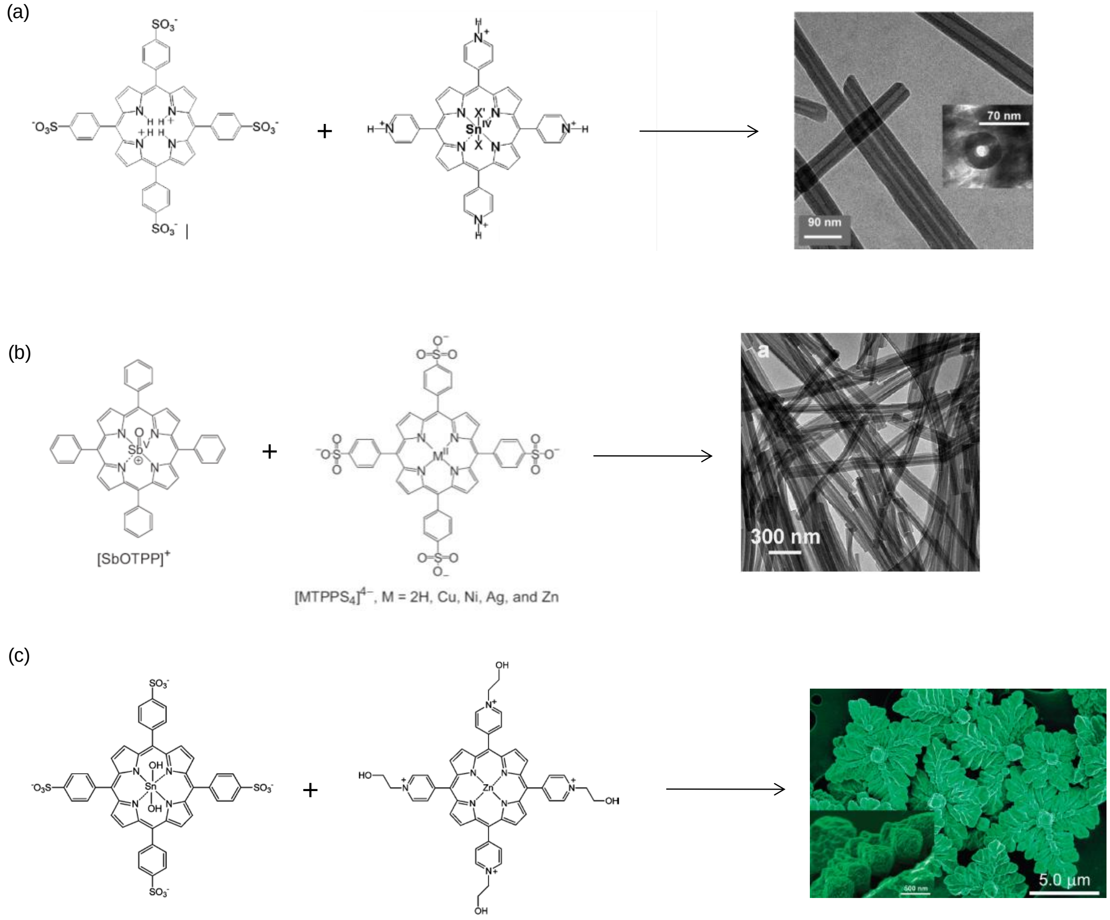

Figure 1.8. (a) The process of self-assembly of porphyrin nanotubes via the ionic interaction between $H_4TPPS_4^{2-}$ and $SnTPyP^{2+}$. The right panel shows the TEM image of the nanotubes. (b) The process of fabricating porphyrin nanofiber bundles through the interaction between $SbOTPP^+$ and $H_2TPPS_4^{-4}$. The right panel shows the TEM image of the nanofiber bundles. (c) The process of preparing porphyrin clovers via the interaction of ZnT(N-EtOH-4-Py)P^{+4} and Sn(OH^-)$_2$TPPS^{-4}. The right panel shows the SEM image of the clovers. (Reproduced from ref. [139] with the permission of the copyright holders.)

Highly crystalline nanostructures consist of porphyrinoid compounds such as porphyrin and phthalocyanine can be obtained by vapor deposition, where the molecules are vaporized and then condensed on a substrate. Vapor deposition is well-developed to apply on the fabrication of devices such as field effect transistors in large scale. This process involves recrystallization of the porphyrinoid compounds without the presence of solvent and assures the high crystallinity of the resulting nanostructures. The formation of rectangular nanotubes from metal-free 5, 10, 15, 20-tetra(4-pyridyl)porphyrin (H_2TPyP) by vapor deposition was reported by Yoon *et. al.*.[140] Figure 1.9 (a) and (b) show the SEM images of the rectangular nanotubes fabricated on Si (100) substrate. Single-crystal X-ray diffraction patterns of the highly crystalline nanotubes were obtained, which allowed the molecular orientation of the porphyrins within the nanotubes to be obtained (Figure 1.9c). Moreover, the fabrication of single-crystalline submicrometer and nanometer ribbons of copper hexadecafluorophthalocyanine (F_{16}CuPc) were reported by Tang *et. al.*.[141] The nanoribbons were grown on aluminum oxide membranes through vapor deposition. (Figure 1.10a) The performance of a transistor based on a single nanoribbon were furthered examined and the transistor was found to be air stable n-type semiconductor with high mobility (Figure 1.10b and c).[142]

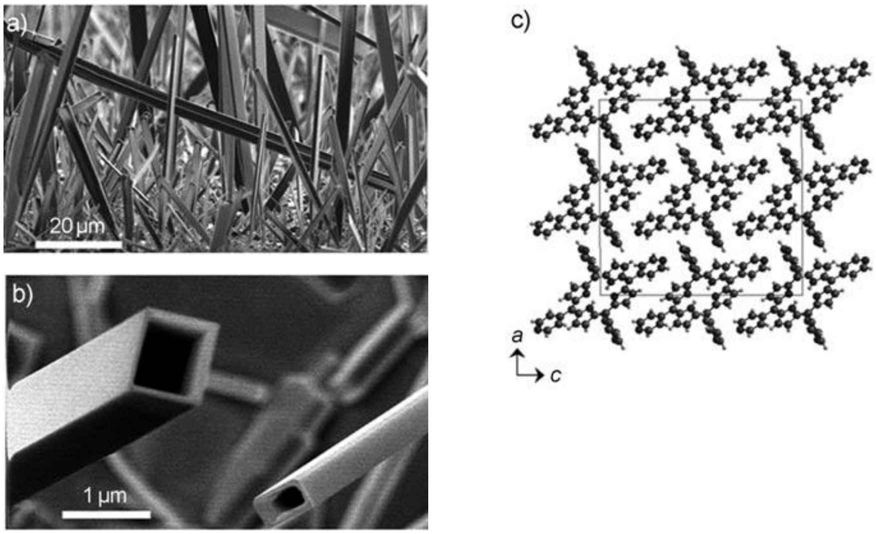

Figure 1.9 (a) and (b) show the SEM images of porphyrin rectangular nanotubes. (c) Unit cells of the porphyrin within the nanotubes. (Reproduced from ref. [140] with the permission of the copyright holders.)

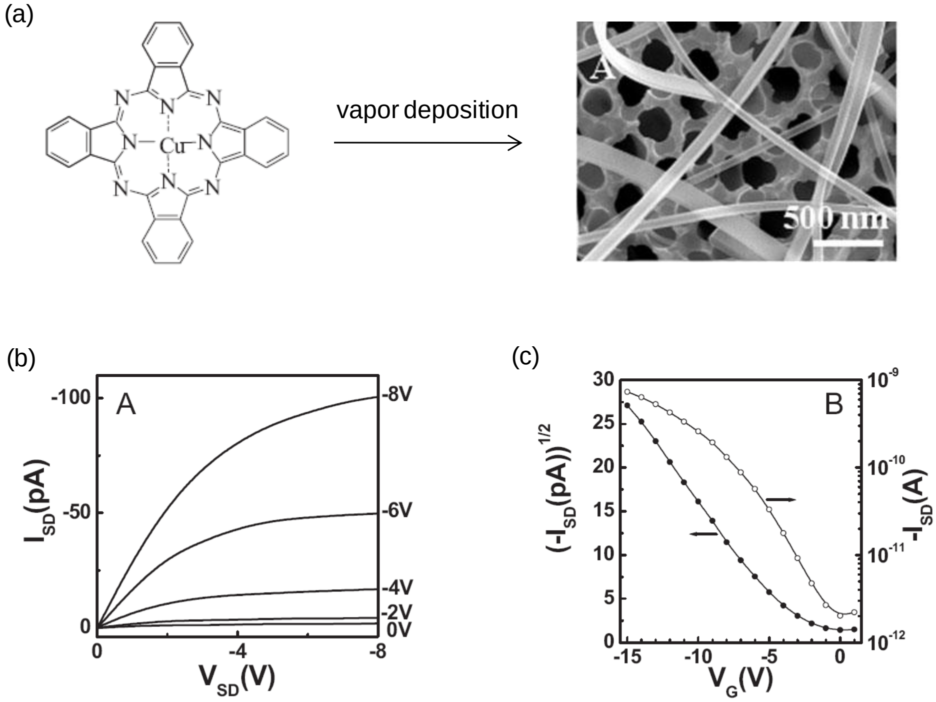

Figure 1.10. (a) Porphyrin nanoribbons obtained by vapor deposition of F_{16}CuPc on aluminum oxide membranes. The right panel shows the SEM image of the nanoribbons. (b) Output characteristics of an organic field effect transistor based on a single nanoribbon. (c) Transfer characteristics of the device measured at a fixed source–drain voltage *V*SD = 10 V (right axis). The solid circles represent the square root of the source–drain current (*I*SD) in the saturation regime as a function of the gate voltage (*V*G, left axis). The channel length is ~10 lm and the width is ~200 nm (width of the ribbon). (Reproduced from ref. [142] with the permission of the copyright holders.)

Coordination polymerization via the interaction between the peripheral groups and metal ions of metalloporphyrins can form supramolecular structures. Crystal structures of porphyrin coordination polymers have been extensively investigated;[143-151] however, there are very few examples of porphyrin coordination polymer structures in nanometer scale. One example is the formation of hollow hexagonal nanoprisms reported by Hu *et. al.* (Figure 1.6c). The nanoprisms are due to the coordination polymerization of a single-type porphyrin based on the interaction between the pyridyl groups and zinc ions.[137] Other types of porphyrin nanostructure can also be obtained via the coordination between the metal ion of metalloporphyrin and ligand compounds. Porphyrin nanospheres assembled through the reaction of MT(4-Py)P complexes (M= Sn^{IV}, Fe^{III}, Co^{III}) with choroplatinic acid were reported by Shelnutt *et. al.* (Figure 1.11).[152]

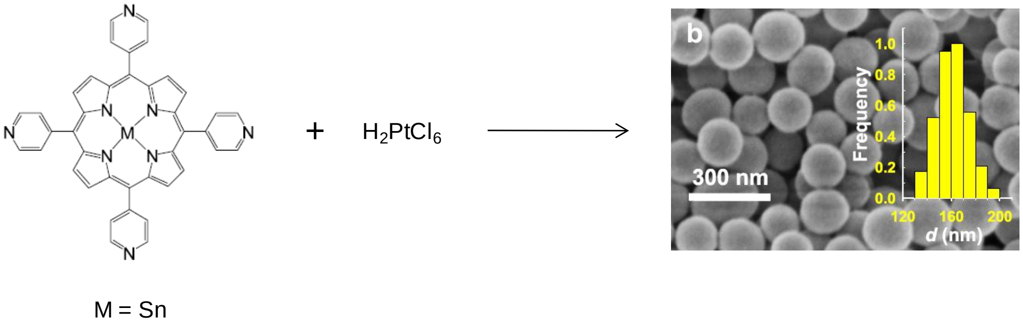

Figure 1.11. The assembly of porphyrin nanospheres through the coordination of Sn(4-Py)P with Pt. The right panel shows the SEM image of the nanospheres. (Reproduced from ref. [152] with the permission of the copyright holders.)

Acidification of porphyrins which have acidic groups such as sulfonic acids and carboxylic acids as peripheral substituents results in aggregation of the porphyrins in aqueous solution. For example, acidification of tetrakis(4-sulfonatophenyl)porphine (TPPS) with HCl forms aggregates in aqueous solution due to the poor solubility of TPPS dications.[40,153] The TPPS aggregates have been intensely studied using UV-vis spectroscopy and various light-scattering techniques; however, the morphology of these aggregates has not been investigated until recent years. The morphology of the aggregates of TPPS dications were characterized using AFM by Schwab *et. al.* and the structures were determined to be nanorods (Figure 1.12).[40] Acidification of tetra(*p*-

carboxyphenyl)porphyrin (TCPP) also formed aggregates of the porphyrin dications.[154,155] The absorption spectrum and morphologies of TCPP aggregates were found to depend on the identity of the counterions.

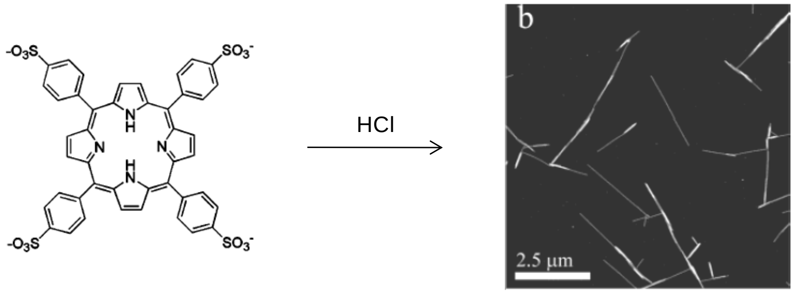

Figure 1.12. Self-assembly of porphyrin nanorods via direct acidification of TSPP. The right panel shows the AFM image of the nanorods. (Reproduced from ref. [40] with the permission of the copyright holders.)

The porphyrin nanostructures can further be modified or self-assemble into more complex structures. Previous reports state that porphyrin nanostructures such as nanorods or nanowires can further self-organized into well ordered hierarchical structures in microscale through their interactions with surfactants or evaporation of solvent.[40, 136] For example, the Sn porphyrin nanowires can further assemble into microscopic columns after aging in the surfactant-rich solution for 1 day (Figure 1.13). The ZnT(4-Py)P based hollow hexagonal nanoprisms were found to self-organized into three-dimensional architectures through solvent evaporation (Figure 1.14). Moreover, metal nanoparticles such as Au and Pt nanoparticles can be decorated on the porphyrin nanostructures via self-metallation of porphyrins to modify the functionalities of the nanostructures.[43,45,138] Figure 1.15 a, b, c and d show the TEM images of porphyrin nanofiber bundles metalized with Pt, Au, Ag and Pt-Au, respectively. Besides self-assembly, many current research efforts have been made to investigate the optoelectronic property,[37,156-160] transistor performance,[140,161,162] and catalytic properties[163] of the porphyrinoid nanostructures. The unique properties of porphyrin nanostructures reveal their potential applications in optoelectronic devices, transistors, catalysis and sensors. The elegance in utilizing these porphyrin materials considers their low cost and simple preparation methodologies.

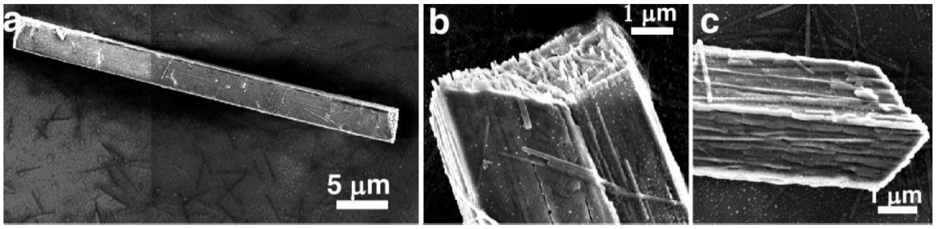

Figure 1.13. SEM images of micrometer-scale columns assembled from Sn porphyrin nanowires in 0.1 mM aqueous solution of Pluronic F127. (Reproduced from ref. [136] with the permission of the copyright holders.)

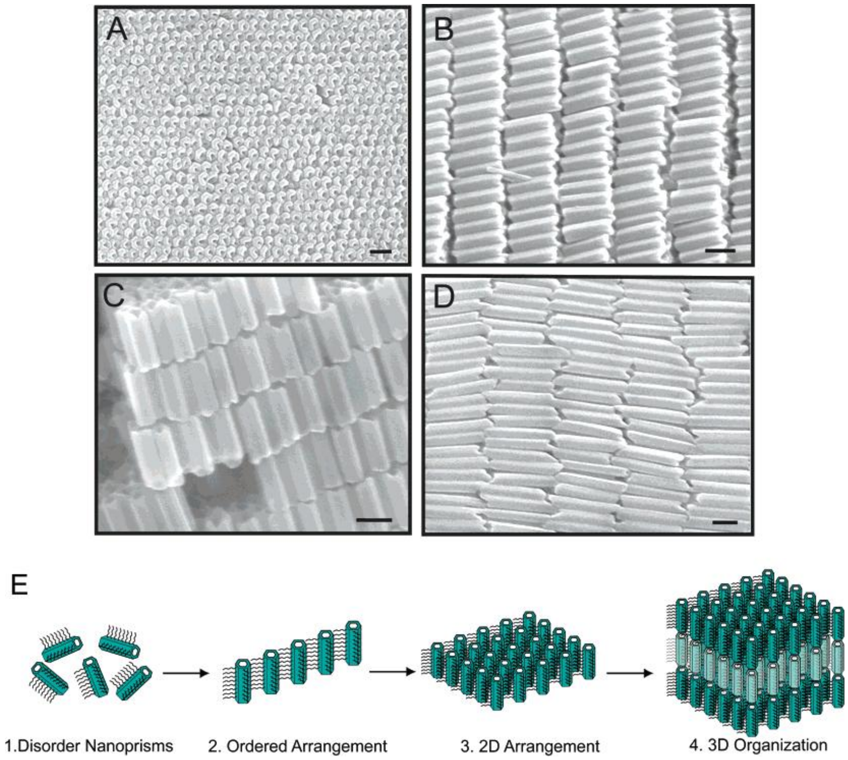

Figure 1.14. SEM images of 3D smectic superstructures self-organized by porphyrin hollow hexagonal nanoprisms. A smectic layer of the nanoprisms in vertical alignment (a), horizontal alignment (b), and horizontal alignment with defects showing a layer-by-layer structure (c). (d) Top view of Sample I in horizontal alignment. The bar length is 200 nm. (e) A schematic illustration of the possible self-organization process of HHNP assemblies. (Reproduced from ref. [137] with the permission of the copyright holders.)

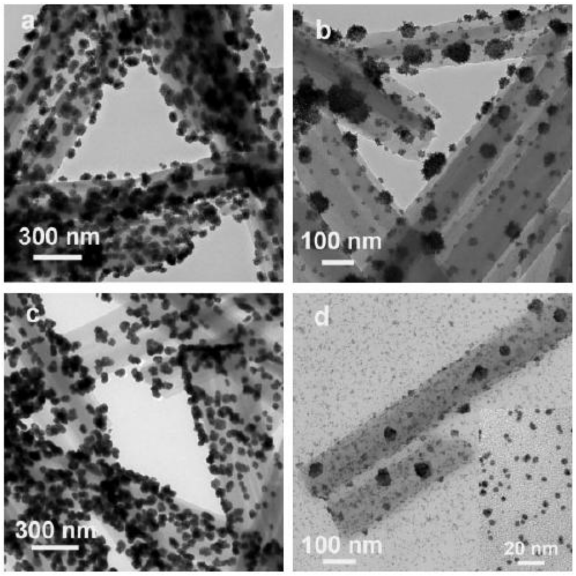

Figure 1.15. TEM images of porphyrin nanofiber bundles metallized with: (a) platinum, (b) gold, (c) silver, and (d) platinum–gold. Inset in (d): expanded view of the nanoparticles not attached to the nanofiber bundles. The durations of light exposure and solution compositions for the metallization reactions are: (a) 6 min, 0.1 mM K_2PtCl_4; (b) 8 min, 0.1 mM Au(I)- thiosulfate complex; (c) 8 min, 1.0 mM Ag(I)-thiosulfate complex; and (d) 8 min, 0.1 mM K_2PtCl_4, 0.1 mM Au(I)-thiosulfate complex, all with 20 mM ascorbic acid. (Reproduced from ref. [138] with the permission of the copyright holders.)

1.5. Introduction of the Following Chapters

In this work, the research is mainly focusd on assembling tetra(*p*-carboxyphenyl)porphyrin (TCPP) into well ordered nanostructures through direct acidification and investigating the optoelectronic, photoluminescence and optical memory effects of the assemblies. Other research projects such as studying the influence of surface energy on the size of porphyrinoid nanoparticles and characterization of polymer nanocomposites for wettability control are also included. In Chapter II, we demonstrate a variety of analysis methods and instruments that were used to characterize the samples in our experiments. The basic concept of the instrumental techniques will also be shown. In Chapter III, the detailed of self-assembly of porphyrin nanostructures through the acidification of TCPP and possible growth mechanisms will be described. The morphologies of the nanostructures were determined by an atomic force microscope (AFM), a scanning electron microscope (SEM) and a transmission electron microscope (TEM). The arrangements of the porphyrins within the nanostructures were probed by the absorption spectrum, TEM electron diffraction pattern and circular dichroism (CD) spectrum. The photoluminescence properties of the porphyrin assemblies were characterized using static spectrafluorometer and time-resolved spectrafluorometer. The electronic and optoelectronic properties were measured using four point probes and two point contact electrodes. Chapter IV provides insight of the counterion effect of the morphologies and photoluminescence properties of the porphyrin nanostructures prepared by direct acidification of TCPP. In Chapter V, we demonstrate a thin film consisting of porphyrin nanostructures that can be utilized for optical memory devices. The fluorescence emission of the thin film can be switched due to its structural transformation of the porphyrin nanostructures. We also show that fluorescence patters can also be created by AFM on the thin film. In Chapter VI, a surface energy gradient prepared by selectively oxidizing an alkanesilane monolayer was used to control the size of porphyrinoid nanoparticles. Chapter VII covers the characterization of the morphologies and surface roughness of various polymer nanocomposites which exhibit superhydrophobic properties or tunable wettability. In Chapter VIII a summary will be given along with the possible future directions of this project.

CHAPTER II

EXPERIMENTAL

2.1. Atomic Force Microscopy

Atomic force microscopy (AFM), which was invented by Binning, Quate and Gerber in 1986, is a high resolution type of scanning probe microscopy. AFM is a tool for obtaining topographical images, measuring physical properties (adhesion, friction) of the surface and manipulating matters in nanoscale. In recent years, lithography methods utilizing AFM such as nanografting,[164-168] nanoshaving,[169-172] and dip-pen lithography[173-178] have been developed. Furthermore, modifying the instrument allows the AFM to measure conductivity,[179-182] thermal properties,[183-185] tip-enhance Raman spectroscopy (TERS) of the sample in nanoscale.[186-192]

The AFM consists of a cantilever attached with a sharp tip which typically is made of silicon nitride and has a diameter around or smaller than 10 nm. The sample is placed on a scan stage which moves in a zigzag direction during the scanning to allow the tip scans through a specific region on the sample. Depending on the condition, the forces between the tip and the sample include van der Waals force, capillary force, chemical bonding, electrostatic force, and magnetic force, etc. The cantilever is fabricated with piezoelectric materials which deforms when external electric field is applied to adjust the movement of the tip during scanning and the deflection of the cantilever is recorded by monitoring a laser beam striking on the top of the cantilever and reflecting to the detector (Figure 2.1). In most cases a feedback voltage is controlled by the software to change the tip height to maintain a constant force between the tip and the surface. Thus, the topographical image of the sample can be obtained by combing the information of sample movement in x-y direction and the tip movement in z direction using the software.

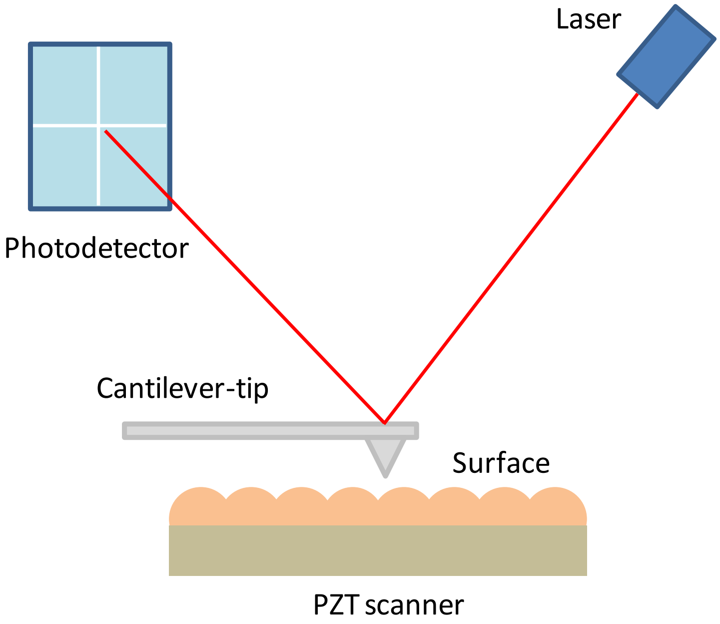

Figure 2.1. Schematic diagram of the setup of an atomic force microscopy.

There are two primary modes in AFM. One is contact mode, and the other is tapping mode (non-contact mode). In contact mode, the tip is dragged across the surface of the sample and the deflection of the cantilever is measured during the process. The tip is directly contact with the surface of the sample and the overall force is repulsive. Moreover, the friction between the tip and the surface of the sample is also measured during the scanning. In tapping mode, the tip does not contact with the sample. Instead, the cantilever oscillates slightly above its resonance frequency above the surface of the sample and the overall force is attractive. Any long range force such as Van der Waals force decreases the resonance frequency of the cantilever. The decrease of the resonance frequency is compensated by the feedback loop which changes the distance between the tip and the surface of the sample in order to maintain a constant oscillating frequency and amplitude. Scanning in tapping mode generates less damage and is more appropriate to measure soft materials than scanning in contact mode.

2.2. Confocal Microscopy

Confocal microscopy, which is patented by Marvin Minsky, is an optical imaging technique that is used to generate image based on the emission of a sample. The instrument overcomes some limits of conventional fluorescence microscope by utilizing point illumination a spatial pinhole to eliminate the out-of-focus light that is thicker than the focal plane (Figure 2.2). Hence only light emission very close to the focal plan can be detected and the optical resolution, especially in the sample depth direction, is much better than the wide-field microscope. However, since most of the light is blocked by the pinhole, typically the signal intensity is low and a long exposure time is required. Detector such as charge couple device (CCD) or photomultiplier tube (PMT) is often used. The three-dimension image based on the emission intensity of the sample and the x-y position can be reconstructed after collecting the light emission at each spatial point. For the confocal microscope (WiTech) that is used in our experiment, a single wavelength beam as the excitation light source goes through an optical microscope and focus on the surface of the sample, and the emission light from the sample is collected by the same microscope and the out-of-focus light which is blocked by the pinholes. The emission light is detected by a CCD detector and the resolution of the confocal is mainly limited by the numerical aperture of the microscope.

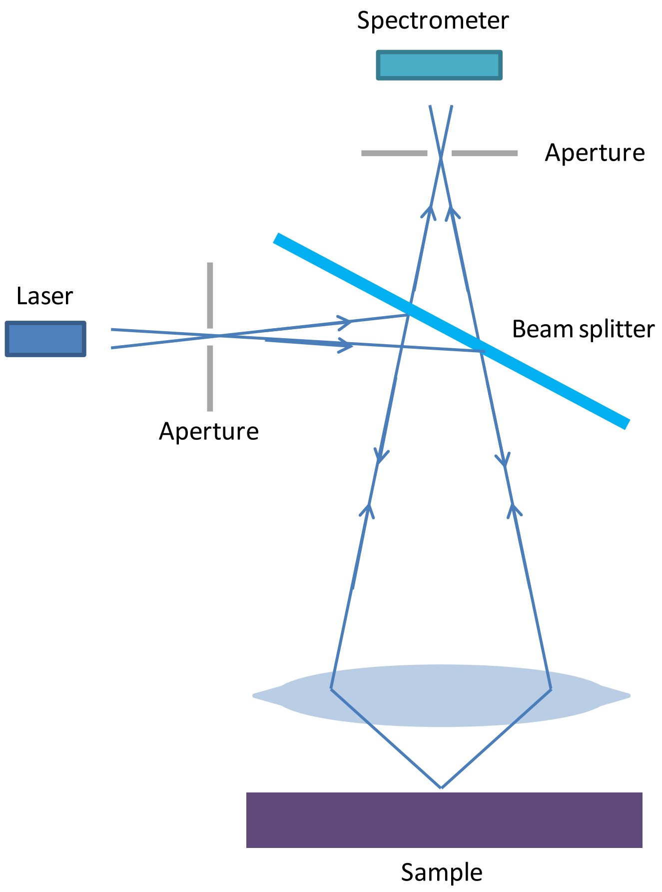

Figure 2.2. Schematic diagram of a confocal spectroscopy.

2.3. Transmission Electron Microscopy

Transmission Electron Microscopy (TEM) is a high resolution microscopy technique which utilizes electron beam to transmit through an ultra thin specimen to the detector. The image is formed by detecting the electrons which are interacted with the specimen and are transmitted by a detector such as a CCD camera. The components of the TEM include an electron gun, a vacuum system, a specimen stage, electron lenses and apertures. The electron gun is designed to generate electron beam by achieving thermionic emission of the filament, which is typically made of tungsten. The electrons can be directed from the filament to the anode plates and are forced into a size with minimum cross section by the Wehnelt cylinder. The vacuum system is required in order to restrict the electron gas interaction and increase the mean free path of the electrons. Electron lenses are fabricated with iron, iron-cobalt or nickel-cobalt alloy and are used to focus the parallel rays at a specific focal length. Apertures are used to exclude the electrons that are far from the optical axis and lower the intensity of the electron beam when measuring beam sensitive samples.

Besides imaging, TEM can also provide other useful information related to sample composition, including electron diffraction and elemental mapping. When being diffracted by the samples, the electrons undergo Bragg scattering and the electron diffraction patterns strike on the back focal plan. By measuring the electron diffraction patterns of a crystalline or a polycrystalline sample at different orientation, the information of the crystal type and atomic or molecular arrangement within the sample may be obtained. Moreover, the inelastically scattering electrons that have energy lost during the interaction with the specimen can offer the information of the chemical composition and electronic properties of the sample. Electron energy loss spectrum (EELS) can be obtained by energy filtering via the magnetic prisms in an EEL-spectrometer that is added on a TEM. Elemental maps can be generated based on the energy lost of the electrons and show the elemental distribution on the sample.

2.4. Scanning Electron Microscopy

Scanning electron microscopy (SEM) is an electron microscopic technique that is used to acquire high resolution images of the surface of the sample. A high-energy electron beam (0.5 – 40 keV) is scanned through the sample, and the interaction of the electrons with the sample produces secondary electrons, back-scattered electrons, transmitted electrons and X-rays. In the SEM, electron beam is thermionically emitted by a tungsten filament within an electron gun in the vacuum chamber. The electron beam is focused by the condenser lenses and passes through the deflection coils in the electron column, and then is deflected by the final lens to scan on the sample. The interaction between the electrons and the sample results in the reflection of the original electrons by elastic scattering, secondary electrons produced by inelastic scattering, and the emission of electromagnetic radiation. The secondary electrons can be detected by an Everhart-Thornley detector, which is a scintillator photomultiplier system. The brightness of the image depends on the number of the secondary electrons sensed by the detector. This is affected by the spatially topographical structure of the sample, therefore, images with three-dimensional appearance and high resolution (~1 nm) can be generated. The back scattering electrons are typically detected by scintillator or semiconducting detector. Since heavy atoms scatter more electrons than light atoms, the back scattering electrons can be utilized to obtain the chemical composition of the sample.

2.5. Ultraviolet-Visible Spectroscopy and Fluorescence Spectroscopy

Ultraviolet-visible (UV-vis) spectroscopy refers to an absorption spectroscopy used to measure the light absorption of the sample in the ultraviolet-visible (including near-UV and near-infrared) spectral range. The light absorption is due to the electronic transition from ground state to the excited states within the molecules. The energy for the π-π transition of the organic molecule with conjugated system usually falls within the UV-vis spectral range. The absorption of the species in solution follows Beer-Lambert Law:

$$A = \log(I_0/I) = \varepsilon \cdot c \cdot L$$

where A is the absorbance, I_0 is the intensity of the incident light at a given wavelength, I is the intensity of the transmitted light, c is the concentration of the absorbing species and L is the path length through the sample. For the setup of the instrument, typically a tungsten lamp (UV, vis and near IR) and a deuterium lamp (deep UV) are used as the light source, PMT is used as the detector, while quartz cuvette is used to contain the sample solution.

Fluorescence Spectroscopy, which is complementary to absorption spectroscopy, is used to measure the transitions from the electronic excited state to the ground state of the molecules. The electrons of the sample are excited to electronic excited states and then rapidly decay to the first excited state S_1. Fluorescence is generated when electrons decay from the first excited state to the ground state ($S_1 \rightarrow S_0$). Typically, the fluorescence emitted by the sample is measured by a monochromator at a constant excitation wavelength. In our experiment, a xenon arcs lamp is used as the light source, while PMT is used as the detector.

Time-resolved fluorescence spectroscopy is an extension of fluorescence spectroscopy. In this technique the fluorescence of the sample is monitored as a function of time after excitation by a laser pulse. The lifetime of the excited state typically follows the first-order kinetics and can be acquired using the equation below:

$$[S] = [S]_0 \, e^{-t/T}$$

Where [S] is the concentration of the excited state molecules at time t, $[S]_0$ is the initial concentration of the excited state molecules and T is the lifetime of the excited state.

2.6. X-ray Photoelectron Spectroscopy

X-ray Photoelectron Spectroscopy (XPS) is a surface analysis technique which is used to measure the elemental composition and the electronic state of the elements within the material. XPS is based on the photoelectric effect, in which an X-ray with specific wavelength provides an energy that allows the electrons within the materials to overcome their binding energy and escape to the vacuum (Figure 2.3). The electron binding energy can be determined by the following equation:

$$E_{\text{binding}} = E_{\text{photon}} - (E_{\text{kinetic}} + \Phi)$$

where E_{binding} is the binding energy if the electron, E_{photon} is the energy of the X-ray photons being used as the source, E_{kinetic} is the kinetic energy of the electrons measured by the detector, and Φ is the work function of the spectrometer. The binding energy of the electrons within different elements are unique, hence the XPS spectrum can be used to determine the composition and the ratio of the existing elements within the sample.

The XPS measurement is carried out in an ultra-high vacuum system, and is utilized monochromatic aluminum K-α X-rays or non-monochromatic magnesium X-rays as the light source. The instrument only detects the electrons that are generated within the top layer (~10 nm) of the materials since the deeper photo-emitted electrons are generally recaptured or trapped before escaping from the materials. Therefore, XPS is highly sensitive to the chemical composition and electronic property at the surface of the sample.

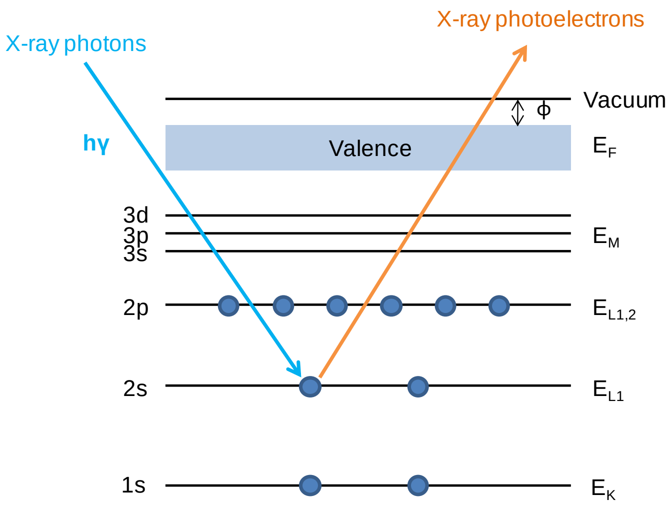

$$\mathbf{K.E. = h\gamma - E_L}$$

Figure 2.3. Schematic illustration of the generation of X-ray photoelectrons in XPS.

CHAPTER III

SELF-ASSEMBLY OF PORPHYRIN NANOSTRUCTURES BY DIRECT ACIDIFICATION

3.1. Synopsis

Porphyrin nanofibers with high aspect ratio up to 400:1 were fabricated by acidifying tetra(*p*-carboxyphenyl)porphyrin (TCPP) using hydrochloric acid in aqueous solution. A broad range of techniques were utilized in this study to determine the morphology, molecular arrangement, and the growth mechanism of the porphyrin assemblies. The results of absorption spectroscopy and atomic force microscopy (AFM) show that once the solution passed the equivalence point at around pH 5, the suspension of the porphyrin nanostructures formed in the solution, and the structures of TCPP assemblies were pH dependent. After the carboxylate groups of TCPP were protonated, the porphyrin forms nanoplates via J-aggregation. At lower pH, the absorption spectrum of the porphyrin nanofibers shows the collapse of the Q bands, revealing the protonation of the core nitrogen of the porphyrin occurred and form TCPP diacids. Highly crystalline lattice in the porphyrin nanofibers were observed using cryogenic-temperature transmission electron microscopy (cryo-TEM). The elemental mapping images of the samples and XPS measurement were used to verify the existence of the chlorides within the porphyrin nanofibers. This indicates the interaction between the TCPP diacids and the chlorides plays a key role in the assembly of nanofibers. In addition, the fluorescence of TCPP was quenched when forming the nanoplates and restored when the porphyrin assembled into nanofibers. The results of circular dichroism (CD) spectroscopy show that although the porphyrin molecules and nanoplates were achiral, the porphyrin nanofibers had supramolecular chirality. Moreover, negative photoconductivity effect of the porphyrin nanofibers was observed by four point probe and current voltage (I-V) measurements.

3.2. Introduction

Porphyrins are attractive molecular building blocks for self-assembly due to their unique optical and electronic properties. They absorb a broad range of light in visible wavelengths and are able to efficiently transport excitation energy. As such, nanoscale assemblies of these materials can be employed in applications such as light harvesting and chemical sensing. Among the porphyrin nanomaterials that have been studied, 1-D and 2-D porphyrin nanostructures with high aspect ratios are of particular interest not only because of their long range electron transport and photoresponsive properties, but also their geometries can be incorporated into viable devices such as organic field-effect transistors. The direct synthesis of 1-D or 2-D porphyrin nanostructures with large aspect ratios however remains a challenge.

Porphyrinoid compounds such as tetrakis(4-sulfonatophenyl)porphine (TPPS) and tetra(*p*-carboxyphenyl)porphyrin (TCPP) are more water soluble than porphyrins with other substitutes and they are able to self-aggregate in the acidic condition. The optical property and morphology of TPPS aggregates have been intensely studied and formation of TPPS nanorods at low pH has been reported. The absorption spectrum of TCPP aggregates has been studied by Choi et al and the absorption of the aggregates was found to be counterion dependent.[154,155] However, the detailed morphology, photoluminescence and corresponding optoelectronic properties of such TCPP aggregates have not been fully investigated.

In this study, we describe the self-assembly of porphyrin nanofibers and nanoplates prepared by acidifying TCPP anions (dissolved in concentrated NH_4OH) by titration with HCl and their resulting optical and electronic properties. Here, the nanoplates form through the J-aggregation of TCPP, while the nanofibers form via electrostatic coordination between the porphyrin dication and chloride. The morphologies and the photoluminescence properties of the porphyrin aggregates were also investigated during the titration. The photoresponsive character of the nanofibers was explored by current-voltage (I-V) measurements.

3.3. Experimental Detail

3.3.1. Materials

Tetra(*p*-carboxyphenyl)porphyrin (>97%) was purchased from Frontier Scientific Inc.. The sample was used without further purification. High purity water (18.2 MΩ·cm, NANOpure Diamond, Barnstead) was used here. Ammonium hydroxide (29%) and hydrochloric acid (37%) were purchased from EMD Chemicals Inc.. Double side polished silicon substrates (Cz, 368 μm, P doped) were purchased from Virginia Semiconductor. Photoresist S1805 and Developer MF-319 were purchased from Microchem Co.. Gold etchant (type TFA) was purchased from Transene Company, Inc.. Cr etchant (CR-7S) was purchased from Cyantek Inc..

3.3.2. Synthesis of Porphyrin Nanostructures

Typically, a 1 mM solution of TCPP in 0.2 M NH_4OH solution was acidified by adding 1 M HCl solution dropwise while stirring at room temperature until the pH decreased to a certain pH. The solution was stirred for another 1 hour after the titration. The titration curve shows an equivalence point at around pH 5, indicating the protonation of the carboxylate groups of TCPP has occurred. Assembly of the nanoplates was found to occur at pH 2 to 5 while the nanofibers were formed when pH was lower than 2.

3.3.3. Structural Studies

The morphologies of TCPP assemblies were characterized using tapping mode atomic force microscopy (AFM, Alpha300 S, WiTec Germany) and transmission electron microscopy (TEM, FEI Tecnai G^2 F20 FE-TEM). For AFM measurements ultrasharp silicon AFM tips (VISTA probes, NanoScience Instruments, Phoenix, Az) with nominal tip radii of <10 nm, a lever frequency of ~300 kHz, and a force constant of ~40 N/m were used. The samples were drop-casted onto a piece of Si wafer and air dried. To remove the salt residue, the substrate was immersed in the same pH diluted HCl solutions and then air dried. For Cryo-TEM measurement, the samples were prepared by plunge freezing using FEI Vitrobot, and then transferred to the cryo-stage and observed in the TEM at the liquid nitrogen temperature. The images and the electron diffraction patterns (EDPs) were obtained in low dose mode to avoid the sample damage from the electron beam. The dose rate was 1500 $e^{-}/nm^{2}/s$. STEM was done using a beam size of 1 nm.

3.3.4. Analysis of Optical Properties

The absorption spectra of TCPP anions in NH_4OH solution and TCPP nanofibers in acidic solution were obtained using an UV-Vis NIR spectrometer (Hitachi U-4100). The static emission spectrum and time decay emission spectrum were acquired using a spectrofluorometer (Fluorolog-3 Horiba Jobin Yvon). A Xenon arc lamp as the source and a PMT steady state detector were used for the measurement of the static emission spectrum. The excitation wavelength was set to be 415 nm. The lifetimes of the samples were measured by a Time-Correlated Single-Photon Counter (Edinburgh Instruments, OB-920). A LED light source with wavelength of 444 nm and 1 ns pulse width and a PMT detector were used to measure the fluorescence lifetime of the samples. Samples were degassed by pure N_2 prior to use and were stirred during the measurements.

3.3.5. X-ray Photoelectron Spectrum (XPS) Measurement

The XPS results were obtained by using a Kratos Axis ULTRA X-ray photoelectron spectrometer equipped with a 165 mm hemispherical electron energy analyzer. The incident radiation was the Al K X-ray line at 1486.6 eV. The analysis chamber was maintained at a steady base pressure of smaller than 6×10^{-9} Torr during sample analysis. Survey scans of up to 1100 eV were carried out at a analyzer pass energy of 160 eV with 1.0 eV steps and a dwell time of 300 ms. Multiplexed high resolution scans were taken at a pass energy of 40 eV with 0.1 eV steps and a dwell time of 60 ms. The survey and high resolution spectra were obtained with averages of 10 scans.

3.3.6. Circular Dichroism Measurements

CD measurements were acquired using an AVIV 62DS spectropolarimeter. Samples were placed in a cuvette with 1 cm path length and the CD spectra were taken every 1 nm between 250 and 600 nm at room temperature.

3.3.7. Four Point Probe Measurements

Volume conductivity was calculated by taking the inverse of the product of the sheet resistance and specimen thickness. Sheet resistance was measured using a Signatone Pro4 Four Point Probe with 0.4 mm probe tip diameter and 1.0 mm tip spacing (Gilroy, CA). Voltages were sourced with an E3644A DC Power Supply with an operating voltage of 1V (Agilent Technologies Inc., Santa Clara, CA), and detected with a Digital Multimeter (Keithley Instruments Inc., Cleveland OH). Voltage and current values were collected in LabView using a SCB-68 Shield I/O Connector Block (National Instruments Inc., Austin, TX). Correction factors were also tabulated because the dimensions of the substrate can influence the sheet resistance

$$R_s = \frac{V}{I} * CF_1 * CF_2$$

where Rs is the sheet resistance, V is the Voltage, I is the current, CF_1 is the correction factor based on the ratio between substrate diameter and the probe tip spacing, and CF_2 is the correction factor based on the ratio between thickness and probe tip spacing. The thikness of the TCPP nanofiber thin film was measured using the AFM tapping mode after scratching through the film.

3.3.8. Two Contact Current-Voltage (I-V) Measurement

Sample was spin-coated on Au electrodes fabricated on a glass substrate. The electodes was prepared by the following procedure: A piece of glass substrate was first immersed in a mixture of $NH_4OH/H_2O_2/H_2O$ (vol 1:1:4) at 85 ^{o}C for 30 minutes. The substrate was then rinsed with liberally of ultra pure water and dried with N_2 stream. The glass substrate was coated with 1 nm of Cr and 50 nm of Au by physcal vapor deposition using a metal evaporator chamber (BOC Edwards Auto 306). The substrate was exposed to UV light (wavelength 185 and 254 nm) for 5 minutes using a UV-ozone cleaner (PSD-UV, Novascan) to increase the hydrophilicity of the surface. The substrate was then spin-coated with Photoresist S1805 at 4000 rpm using a spin coater (WS-400B-6NPP/Lite, Laurell Technology, Co.) and heated to 120 ^{o}C for 3 minutes on a hot plate.

To create the pattern of the electrodes, the substrate was covered by a self-designed mask and exposed to near UV light (350~450 nm spectral range, 76 mW/cm^2 output) using a Flood Exposure Source (97435, Newport Co.) for 3 seconds and immersed in Developer MF-319 and rinsed with liberally of ultra pure water and dried with N_2 stream (Figure 3.1a). On the photoresist, the region expose to the UV light will be selectively dissolved in the developer and form the pattern. To produce a 3 µm gap on the photoresist pattern, a laser beam (488 nm, 70 µW/µm^2 output) was scanned through the strip patterns (Figure 3.1b), and the substrate was immersed in the developer and cleaned with ultra pure water and dried with N_2 stream (Figure 3.1c). To form the Au patterns, the substrate was immersed in gold etchant (TFA) and chromium etchant (CR-7S) sequentially and cleaned with ultra pure water and dried with N_2 stream (Figure 3.1 d). To remove the top layer of the photoresist, the substrate was treated with oxygen plasma using a plasma cleaner (PDC-32G, Harrick Plasma) and rinsed with literally of acetone and then dried with N_2 stream (Figure 3.1 e).

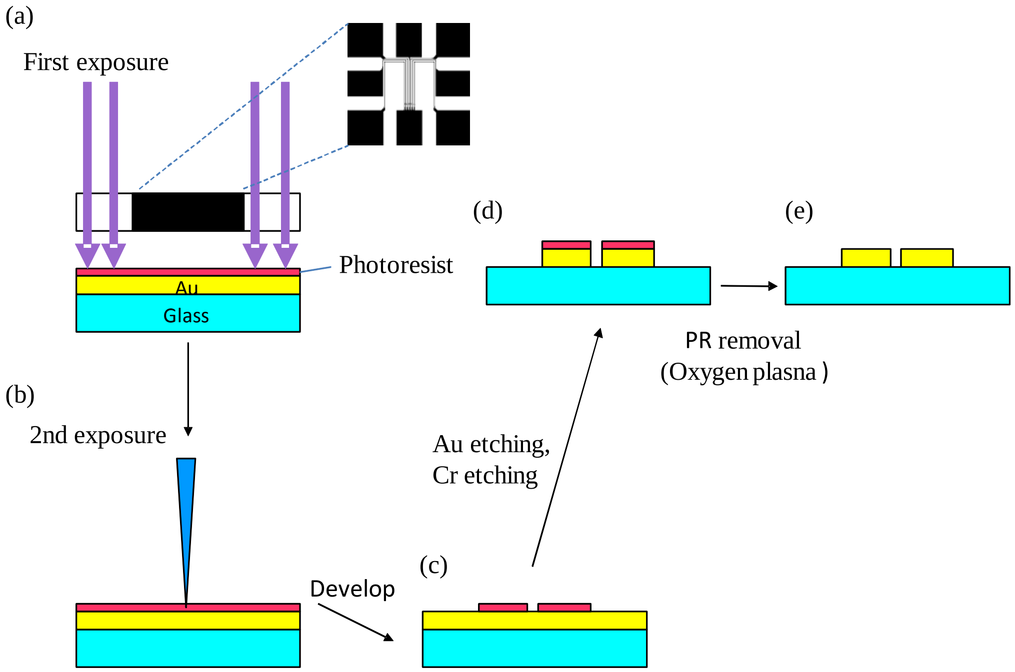

Figure 3.1. Schematic illustration of preparing Au electrodes for the measurement of optoelectronic property.

3.4. Results and Discussion

The sample of TCPP aggregates formed at pH 1 was first characterized. Spectroscopically, collapse of the four Q bands due to the protonation of the core nitrogens of TCPP was observed. As a result, the product at pH value of 1.0 resulted from the aggregation of TCPP diacids as the porphyrinic building blocks (Figure 3.2a) which are then coordinated via interstitial chloride ions.

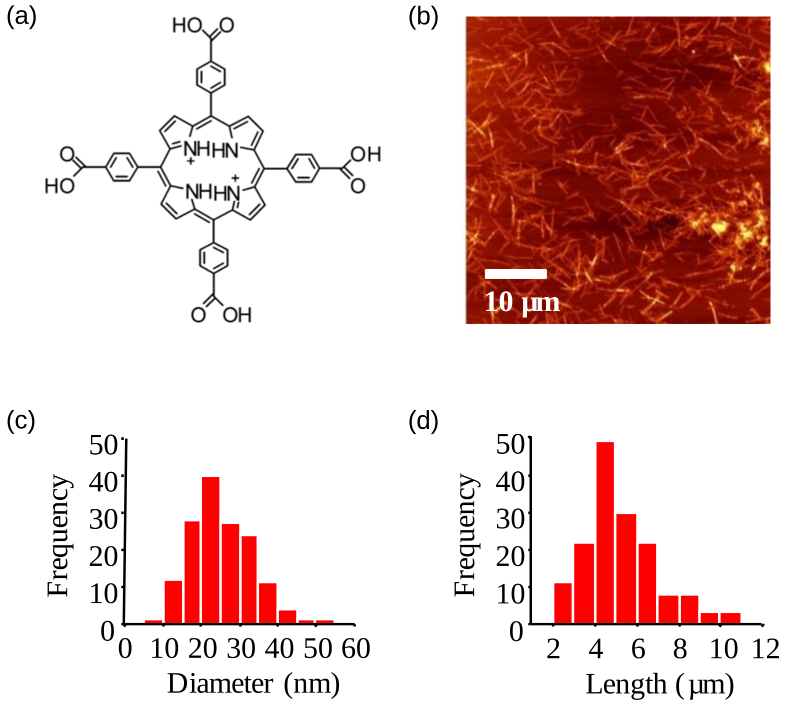

Figure 3.2. (a) The structure of TCPP diacid. (b) AFM topographic image of TCPP nanofibers on Si. The image was acquired in tapping mode. (c) Statistic diagram of the diameter of TCPP nanofibers. (d) Statistic diagram of the length of TCPP nanofibers.

The morphology of the assemblies was characterized by atomic force microscopy (AFM) in tapping mode and transmission electron microscopy (TEM). Figure 3.2b shows an AFM topographic image of TCPP nanofibers deposited on Si surface. The nanofibers exhibit high flexibility and large aspect ratios. The average diameter of the TCPP nanofibers was 25 ± 8.5 nm, ranging from 9 to 58 nm (Figure 3.2c), while the average length of TCPP nanofibers was estimated to be 5.2 ± 1.7 µm (Figure 3.2d). In some cases the length of the nanofibers were found to be over 10 µm, giving an aspect ratio up to 400:1. The TCPP nanofibers were also observed in Cryo-TEM of the frozen state inside the solution using low-dose mode (Figure 3.3a and b), as the samples were very sensitive to the electron beam and could be damaged in few seconds even in the low-dose mode. The images show a clear lattice aligned along the long axis of the nanofibers (Figure 3.3b). This indicates that the TCPP molecules arrange into highly ordered crystalline structures to form the nanofibers, with a lattice spacing of 1.8 nm. Electron diffraction patterns (EDPs) also reveal a lattice spacing of 1.80 nm as seen in the image. Another periodic spacing, along the fibre long axis direction of 0.46 nm, which may be related to the porphyrin stacking distance, was also observed (Figure 3.3c and d).

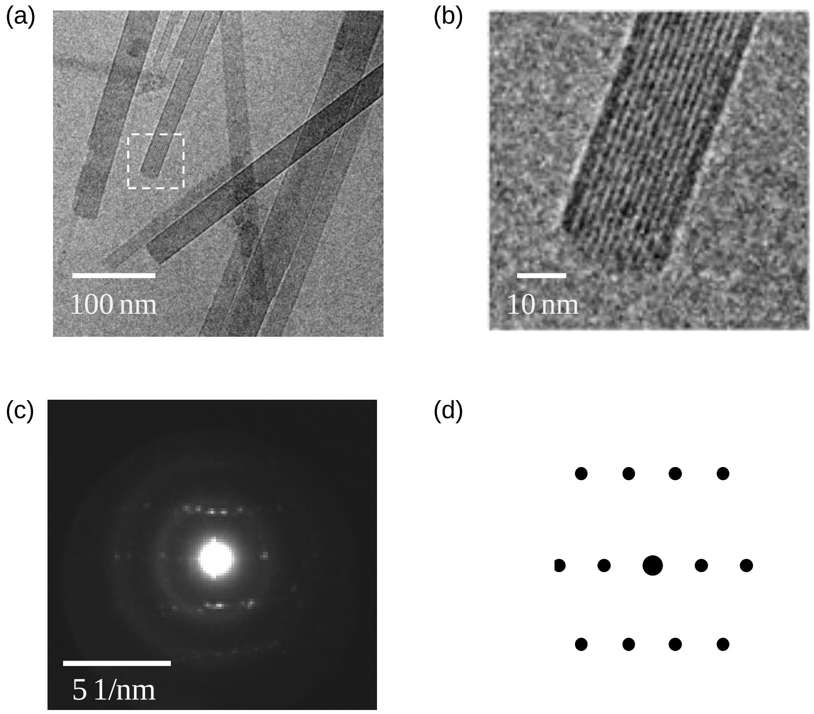

Figure 3.3. (a) Cryo-TEM image of TCPP nanofibers. (b) Enlargement of the region within the dashed square of (b). Note the background seen in (b) is ice rather than a support film. The lattice spacing in (b) is 1.8 nm. (c) Electron diffraction pattern of TCPP NFs at cryogenic temperature and (d) its schematic pattern showing the geometry of the reflections.

It has been previously proposed that TCPP diacids may be self-assembled with counter-anions in aqueous solution near pH 1.[155] To clarify the role of chloride in the self-assembly of these nanofibers, the samples were characterized using TEM elemental-mapping. Figure 3.4a and Figure 3.4b-d are the scanning TEM (STEM) and elemental maps of TCPP nanofibers using an energy filter, respectively. The distribution of Cl within the nanofibers is similar to the distribution of C and N. This clearly indicates that chloride took part in the self-assembly of nanofibers with the TCPP diacids, most likely through electrostatic interaction and hydrogen bonding. This is not surprising since porphyrin networks constructed through the interaction between porphyrins and anions, such as phosphates, chlorides or bromides, have already been reported.[193,194] Furthermore, the XPS spectrum of the nanofibers prepared in pH 1 HCl solution and deposited on Si shows the signals of Cl $2p_{3/2}$ and Cl $2p_{3/2}$ at 198.3 and 199.8 eV, repectively (Figure 3.5a). The binding energy and peak area of the elements within the nanofibers are summarized in Table 3.1. The atomic ratio of Cl and N in the nanofibers is around 1:3.8, determined by XPS, revealing the ratio between chloride and TCPP is close to 1:1 in the nanofibers.

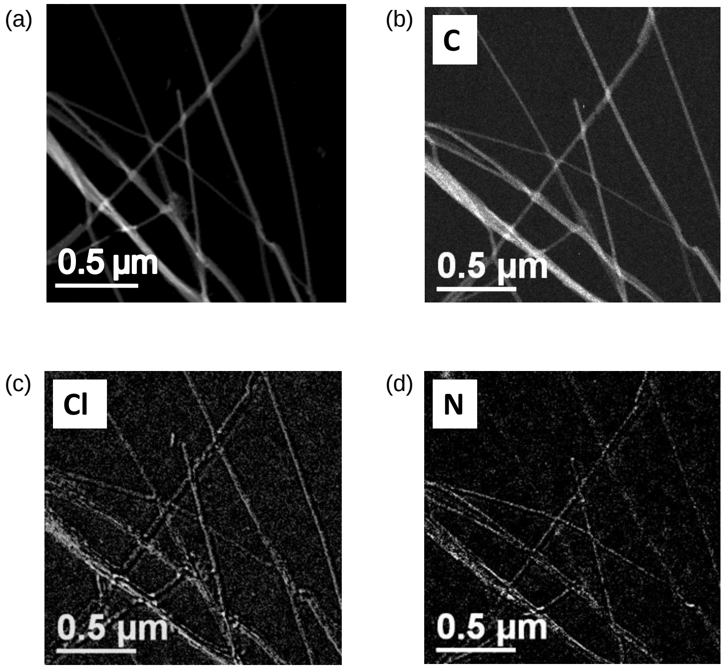

Figure 3.4. (a) STEM image and (b)-(d) elemental maps of TCPP nanofibers.

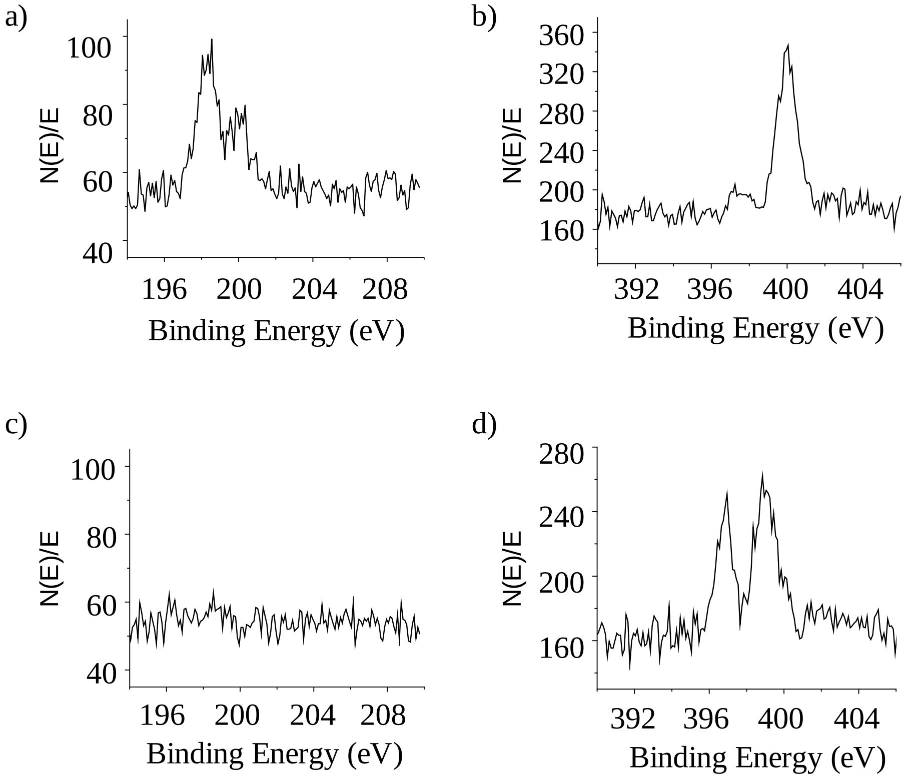

Figure 3.5. XPS spectrum of TCPP nanofibers formed in pH 1 HCl solution in (a) Cl 2p and (b) N 1s regions, and the spectrum of TCPP nanoplates formed in pH 3 HCl solution in (c) Cl 2p and (d) N 1s regions.

Table 3.1. The XPS results of TCPP nanofibers prepared in pH 1 HCl solution.

Peak	Position BE (eV)	FWHM (eV)	Raw Area (cps eV)	Atomic Mass	Atomic Conc (%)
O 1s	531.5	3.2	1083	16.0	14.7
N 1s	400.0	1.1	223	14.0	5.3
C 1s	284.4	1.4	1829	12.0	78.6
Cl 2p	197.9	1.1	101	35.5	1.4

To investigate the growth mechanism of the porphyrin nanofibers, samples of TCPP solution at different pH were prepared by carefully adding various amount of HCl solution into the initial TCPP/NH_4OH solution while stirring. It is observed that once the pH passed the equivalence point at around pH 5 suspension formed in the solution. The color of the suspension appeared to be brown when pH was higher than 2.0 and changed to green when pH was lower than 2.0. The AFM and cryo-TEM images show that the brown suspension appeared between pH 2.5 and 4.0 were composed of porphyrin nanoplates. Figure 3.6a, b and c show the typical AFM and cryo-TEM images of the porphyrin nanoplates. The width of the nanoplates was ranging from 35 to 80 nm with an average height of 2.6 ± 0.4 nm. Moreover, on the absorption spectrum the Soret band of the porphyrin broadened and red shifted when pH changed from 4.0 to 2.5 (Figure 3.7a and c), while four Q bands red shifted as well (Figure 3.7b and d), revealing the porphyrin formed J-aggregates.[126] It is possible that protonation of the carboxylic acid groups of TCPP decreased the solubility of the porphyrin and initiated the stacking of the porphyrin via π-π interaction and hydrogen bonding, resulting in the formation of nanoplates.

As the pH decreased to 2.0, the Q bands collapsed (Figure 3.7d), revealing the porphyrin exhibited four-fold symmetry due to the protonation of the core nitrogens.[40,119,155] Interestingly, formation of extra long nanofibers with length up to 125 was observed in this condition (Figure 3.6e). Comparing to the size of the nanofibers formed at pH 1.0, the nanofibers formed at pH 2.0 were much longer, however, they exhibited the same lattice in the TEM images, indicating in both conditions the porphyrin nanofibers had the same crystallinity. When the pH was decreased to 1.5, the average length of the nanofibers reduced to 5.3 ± 1.1 μm (Figure 3.6f). Furthermore, when the pH was decreased from 2.0 to 1.0, on the absorption spectrum the Soret band sharpened and shifted back to 415 nm, which is close to the wavelength of the monomers. This is likely due to the intercalation of chlorides occurred when pH was lower than 2.0 since protonation of the core nitrogens of TCPP results in the porphyrin dications, which could have electrostatic interaction with anions. The insertion of chlorides may weaken the π stacking of the porphyrin and disrupt the J-aggregation of the porphyrin, resulting in the the structural transformation from nanoplates to nanofibers. The narrower Soret band indicates the porphyrins within the nanofibers are more ordered comparing to their nanoplates structure.

More evidence of the presence of neutral TCPP in the nanoplates and the formation of the TCPP diacids within the nanofibers was obtained by the XPS measurement. The N 1s portion of the XPS spectrum of the porphyrin nanoplates formed in the pH 3 HCl solution shows two peaks at 396.8 and 399.4 eV (Figure 3.6d). The higher binding energy is assigned to the two nitrogen atoms that are bound to the hydrogen atoms, and the lower energy is ascribed to the other two nitrogen atoms without binding any hydrogen atom in the neutral porphyrin.[195,196] The XPS spectrum of TCPP diacids within the nanofibers formed in pH 1 HCl solution shows the higher energy peak shifts in the N 1s region to 400.5 eV with an intensity increase due to the protonation of the porphyrin core nitrogen atoms (Figure 3.6d).[196] The lower energy peak shifts to 397.3 eV and does not totally disappeared, revealing some TCPP diacids were lost under the condition of the XPS experiment. Moreover, the Cl 2p signals were not observed in the XPS spectrum of TCPP nanoplates, indicating the nanoplates were barely constructed with the neutral TCPP, and chlorides were not intercalated into the porphyrin nanoplates (Figure 3.6c).

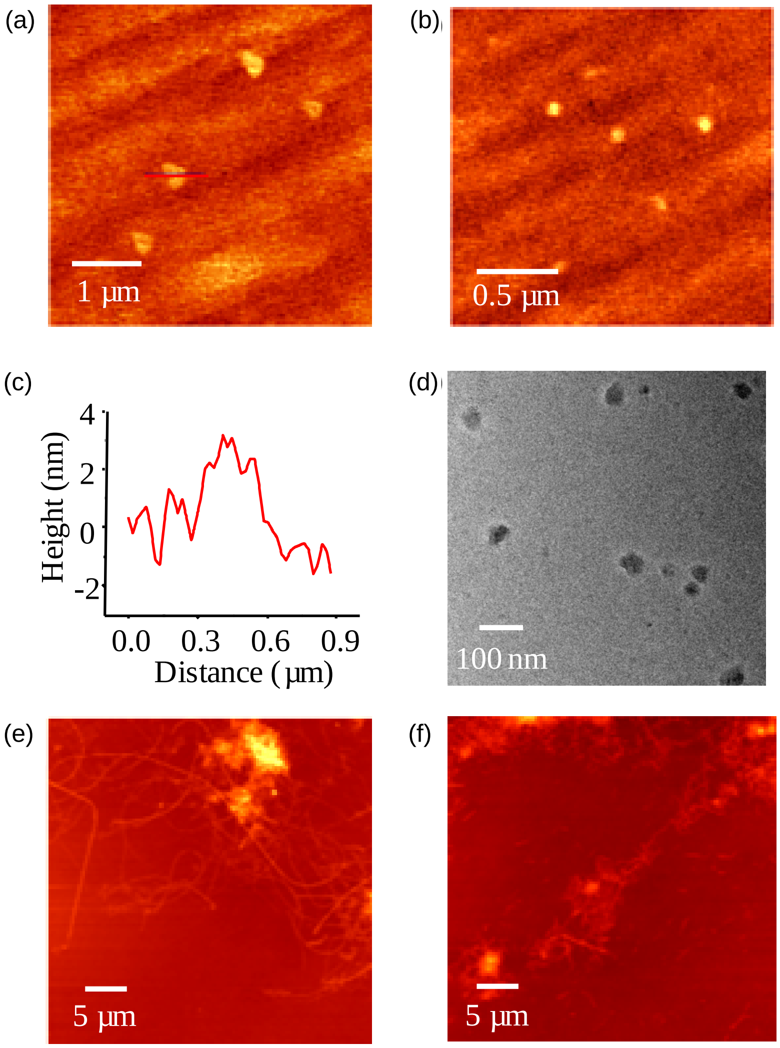

Figure 3.6. (a) and (b): AFM images of TCPP nanoplates prepared at pH 4.0 and 3.0, repectively. (c) Height profile of the trace line on (a). (d) Cryo-TEM image of the nanoplates prepared at pH 3.0. (e) AFM image of extra long TCPP nanofibers prepared at pH 2.0. (f) AFM image of TCPP nanofiber prepared at pH 1.5.

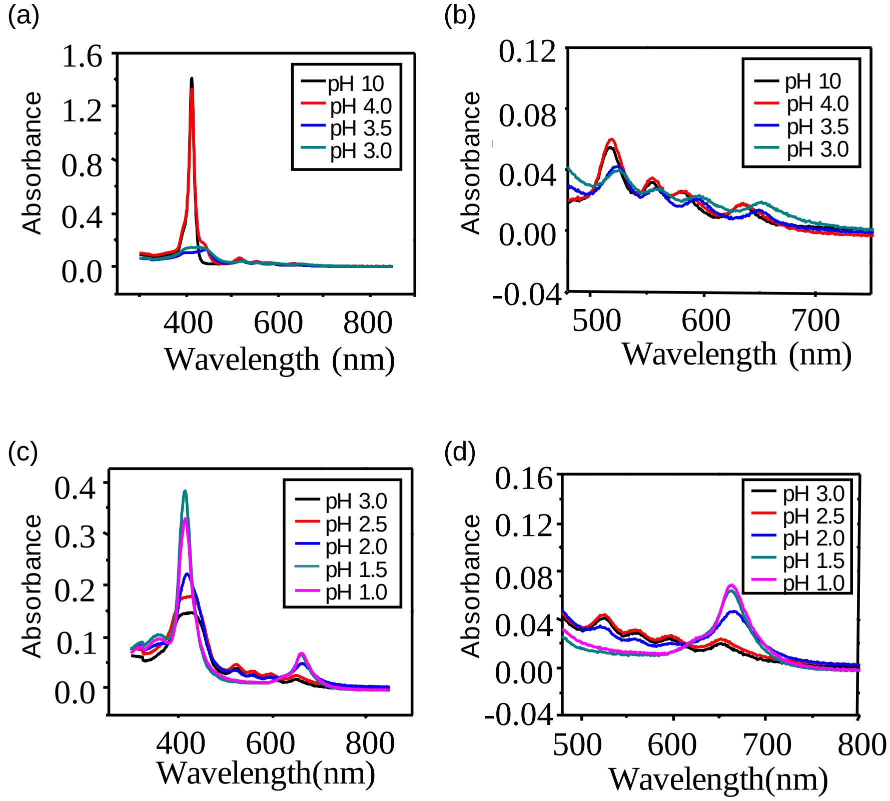

Figure 3.7. Absorption spectra of TCPP aqueous solution at (a) pH 10, 4.0, 3.5, 3.0, (c) 3.0, 2.5, 2.0, 1.5, and 1.0. (b) Spectral region covering the Q bands of (a). (d) Spectral region covering the Q bands of (d).

The photoluminescence properties of TCPP anions in the NH_4OH solution and TCPP assemblies in HCl solutions were studied by performing static and time-resolved fluorescence measurements. The quantum yields of the samples were also measured using tris(2, 2'-bipyridyl)ruthenium(II) [$Ru(bpy)_3^{2+}$] as reference. The quantum yields of the porphyrin solutions were acquired using the equation:

$$Q = Q_R \frac{I}{I_R} \frac{OD_R}{OD} \frac{n^2}{n_R^2}$$

Where Q and Q_R are the quantum yield of the sample and the reference, respectively. I and I_R are the fluorescence peak areas of the sample and the reference, respectively. OD and OD_R are the absorption of the sample and the reference at the same wavelength, respectively. n and n_R are the refraction indexes of the solvent of the sample and the solvent of the reference, respectively.

The emission spectra of TCPP solutions at different pH are shown in Figure 3.8a. The experimental results of the quantum yield measurements and the lifetime measurements are summarized in Tables 3.2 and 3.3, respectively. The emission spectrum of anionic TCPP in the NH_4OH solution (pH ~10) shows the fluorescence of the porphyrin with maxima intensities at around 613 and 658 nm (Figure 3.8a black line). The quantum yield Φ was determined to be 0.79%, and the fluorescence decay profile was bi-exponential with a long-lived (8.3 ns) and a short-lived (1.7 ns) component (Figure 3.8b). The long-lived component can be ascribed to TCPP anionic monomers, while the short-lived component can be ascribed to TCPP anionic dimers. In the acidic condition at pH 4.0, in which the assembly of TCPP nanoplates occurred, the fluorescence of the porphyrin shifted to 650 nm (Figure 3.8a red line), and the quantum yield Φ of the porphyrin slightly decreased to 0.57%. Fitting the fluorescence decay curve of TCPP solution at pH 4.0 resulted in a major component with lifetime of 2.8 ns (93%), and a minor component with lifetime of 0.69 ns (7%) (Figure 3.8c). It is worth notice that the absorption feature of TCPP solution at pH 4.0 is quite similar to the absorption of TCPP anions at pH 10.0 except the presence of a new shoulder of the Soret band at a higher wavelength (Figure 3.6a), revealing the aggregation of the porphyrin

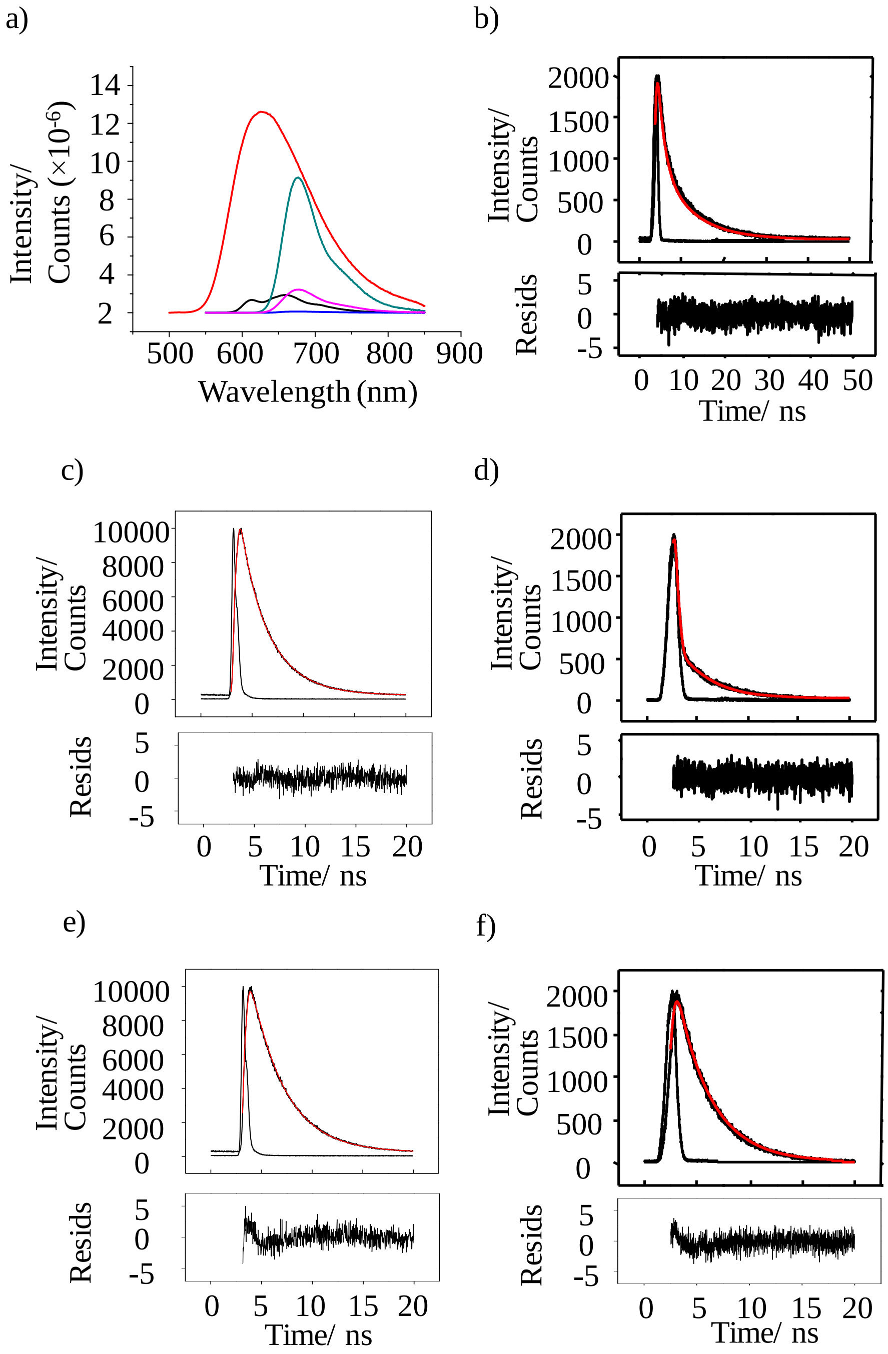

Figure 3.8. (a) Emission spectrum of TCPP anions in 0.2M NH_4OH solution (black line), TCPP in aqueous solutions at pH 4.0 (red line), pH 3.0 (blue line), pH 2.0 (green line) and at pH 1.0 (purple line). (b), (c), (d), (e) and (f) are the time-resolved fluorescence spectrum of TCPP in 0.2M NH_4OH solution. (λ_{em}: 660 nm), in pH 4.0 (λ_{em}: 680 nm), pH 3.0 (λ_{em}: 680 nm), pH 2.0 (λ_{em}: 673 nm), pH 1.0 HCl solutions (λ_{em}: 680 nm), respectively. Excitation wavelength: 436 nm.

Table 3.2. The experimental data and results of the quantum yield (*Φ*) measurements for TCPP solutions.

	TCPP absorption at 436 nm	$Ru(bpy)_3$ absorption at 436 nm in H_2O	TCPP fluorescence peak area	$Ru(bpy)_3$ fluorescence peak area	*Φ* (%)
In NH_4OH	0.051	0.052	8.88×10^7	4.83×10^8	0.79
pH 4	0.177	0.182	1.92×10^8	1.45×10^9	0.57
pH 3	0.263	0.249	5.29×10^6	1.82×10^9	0.12
pH 2	0.502	0.495	5.16×10^8	2.71×10^9	0.80
pH 1	0.279	0.274	9.15×10^7	1.94×10^9	0.19

Table 3.3. The results of the lifetime (τ) measurements for TCPP solutions, the possible components in the solutions, and the morphologies of the porphyrin assemblies based on the AFM results.

Medium	*τ* (ns)	Components	Morphologies
pH 10	8.3 (73%)	Monomeric TCPP anions	———
	1.7 (27%)	Dimeric TCPP anions	
pH 4.0	2.8 (93%)	Dimeric TCPP	Nanoplates
	0.69 (7%)	TCPP J-aggregates	
pH 3.0	3.2 (57%)	TCPP diacids	Nanoplates
	0.12 (43%)	TCPP J-aggregates	
pH 2.0	3.2 (100%)	TCPP diacids	Nanofibers
pH 1.0	3.2 (100%)	TCPP diacids	Nanofibers

was not severe in the solution at pH 4.0. Thus the major component in the solution at pH 4.0 is likely to be TCPP monomer or dimer, and the minor component could be the J-aggregates of the porphyrin. Comparing with the lifetime of TCPP anionic monomers (8.3 ns), the lifetime of the major component (2.8 ns) in the solution at pH 4.0 is closer to the lifetime of the TCPP anionic dimers (1.7 nm), hence we attribute this component to TCPP dimers. Further lowering the pH of TCPP solution to 3.0 strongly quenched the fluorescence of the porphyrin ($\Phi \sim 0.12\%$). (Figure 3.8a blue line), and the fluorescence decay was bi-exponential with an extra short-lived component (0.12 ns) and a long-lived component (3.2 ns) (Figure 3.8d). The former can be attributed to the lifetime of TCPP J-aggregates, and the latter can be attributed to the lifetime TCPP diacids, which will be discussed later. Although TCPP diacids were partially formed in the solution at pH 3.0, no fiberic structures were found in the results of AFM and TEM (Figure 3.6b and d), indicating the porphyrin diacids may remain monomeric in the solution. Moreover, the XPS spectrum of TCPP nanoplates formed in pH 3.0 HCl solution shows no chloride signals, revealing that the porphyrin diacids and chlorides only had weak interaction, which was not sufficient to keep chlorides in the porphyrin assemblies during solvent evaporatio. The decrease of the quantum yield is possible due to the formation of TCPP J-aggregates, which could be non-fluorescent complexes and led to self-quenching of the porphyrin. The red-shift of the Soret band (~15 nm) for the porphyrin solution at pH 3 in the absorption spectrum reveals the exciton coupling effect between the nearby porphyrins within the aggregates (Figure 3.7a). Decreasing the pH of the porphyrin solution to 2.0, in which the porphyrin formed nanofibers, drastically recovered the emission of the porphyrin ($\Phi \sim 0.80\%$) (Figure 3.8a green line). The time-resolved fluorescence spectrum of TCPP solution at pH 2.0 shows a mono-exponential decay curve with a single component (3.2 ns), which indicates the porphyrins in the solution were completely converted into the diacids (Figure 3.8e). Moreover, the Soret band of the porphyrin solution at pH 2.0 in the absorption spectrum was sharpened and shifted toward the wavelength of the Soret band of the anionic porphyrin in NH_4OH solution (from 430 to 415 nm, Figure 3.7a), implying the exciton coupling between the porphyrins was weakened, possibly due to the well order of the porphyrin diacids within the fibers and the increase of their interplanar separation resulted from the chloride intercalation into the assemblies. Continuously decreasing the pH of the porphyrin solution to 1.0 decreased the quantum yield ($\Phi \sim 0.19\%$) of the porphyrin. The reason for the decrease in quantum yield remains unclear and is still being investigated. Comparing with the porphyrin solution at pH 2.0, the porphyrin solution at pH 1.0 shows no difference in the emission wavelength and the lifetime (Figure 3.8f).

Recently, the chiroptical properties of porphyrin-based supramolecular assemblies have drawn a lot of interests due to their potential applications in sensing, memory devices, chiroptical devices, etc.[197-201] It has been reported that a number of achiral porphyrins were able to self-assemble into chiral supramoecular structures through noncovalent interactions.[194,202,203] For example, it has been shown that achiral zinc 5,10,15,20-tetra(4-pyridyl)-21H,23H-porphine (ZnTPyP) was able to form nanorods with supramolecular chirality.[202] Here, the chiroptical properties of TCPP anions, nanoplates and nanofibers were examined using circular dichroism spectroscopy. Figure 3.9 shows the results of the CD spectra of the porphyrin in the diluted ammonium hydroxide solution at pH 10 and in the diluted hydrochloric acid solutions which their pH values were varied between 1.0 and 4.0. The solutions were not stirred during the measurement to prevent any macroscopic anisotropy induced by the vortex of the solvent. At pH 10, as expected, the sample shows no signal in the CD spectrum (Figure 3.9 black line), indicating the porphyrin anions are achiral. At pH 4.0 and 3.0, in which TCPP self-aggregates into nanoplates, the samples were also CD silent (Figure 3.9 orange and green lines), revealing that the porphyrin nanoplates were achiral. As the pH lower to 2.0 and 1.0, however, TCPP nanofibers show absorption differences at the Soret band in the CD spectrum (Figure 3.9 blue and red lines). This indicates the porphyrin nanofibers have supramolecular chirality due to the symmetry breaking resulted from the stacking of the TCPP diacid. The absorption difference of the sample at pH 2.0 was larger than the sample at pH 1.0. It is worth notice that TCPP self-assembled into nanofibers in both conditions, but the aspect ratio of the nanofibers formed at pH 2.0 was much higher than the nanofibers formed at pH 1.0. This suggests longer porphyrin nanofibers exhibit stronger supramolecular chirality.

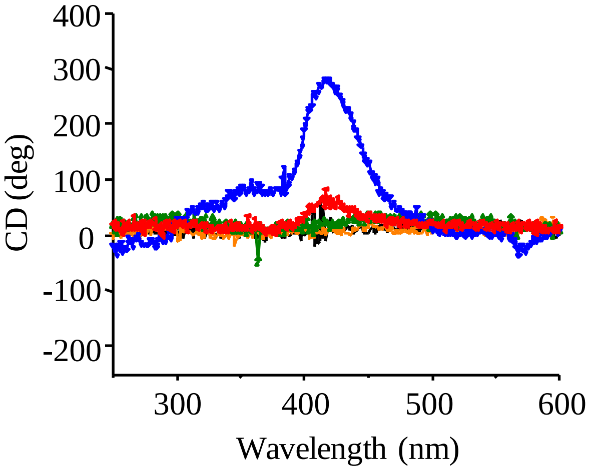

Figure 3.9. CD spectra of TCPP (6.25 μM) in aqueous solution at pH 10 (black line), 4.0 (orange line), 3.0 (blue line), 2.0 (green line) and 1.0 (blue line).

In order to investigate the optoelectronic response of the TCPP nanofibers, four point probe measurements and two contact current-voltage (I-V) measurements were also conducted. To measure the conductivity of the TCPP nanofibers, a thin film of the nanofibers with thickness of 5.6 ± 1.4 μm on glass was prepared and its conductivity was measured using a four point probe. The conductivity of the thin film was found to be 0.62 mS/cm, when measured in the dark. This decreased to 0.41 mS/cm when the sample films were irradiated with white light (25 W/m^2). From the four point probe measurements, the conductivities show that the TCPP nanofibers are semiconducting in nature. To examine the I-V performance of the TCPP nanofibers, the nanofibers were also spin-coated across two Au electrodes, prepared by photolithography, with a gap of 3 μm, as shown in Figure 3.10b and c, with around 60 TCPP nanofibers across the electrodes. Interestingly, when the samples were irradiated with white light, the current decreased reversibly (Figure 3.10a). The light could be switched on and off periodically and the current responded consistently. The current decreased more when the white light intensity was larger. The similar negative photoconductivity effects have been observed in the cases of Ge nanocrystals,[204] SiO_2 films,[205] and ZnO nanowires[206] and can be attributed to the results of reducing the carriers of the materials by charge-hole recombination through photoexcitation, or due to photoexciting the electrons to the trap states. Further experiments however will be required to clarify the mechanism.

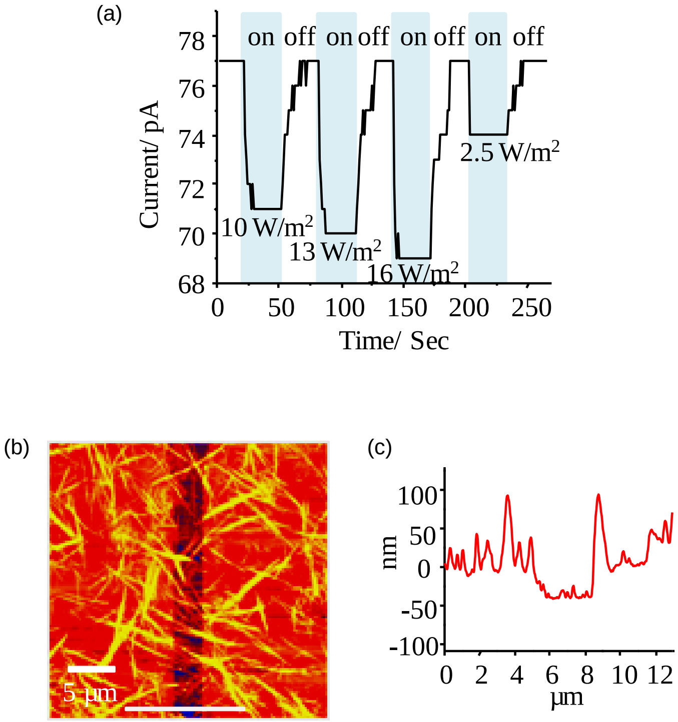

Figure 3.10. (a) Dependence of current on time at 0.5 V when white light with different power intensity was turned on and off periodically at room temperature. (b) AFM topography image of TCPP nanofibers distributed between two Au electrodes. The region of the glass substrate without Au is marked in blue. (c) Height profile of the trace line on (b).

3.5. Summary

We have shown that by simply controlling the pH porphyrin nanoplates and highly crystalline porphyrin nanofibers can be prepared by acidifying TCPP in aqueous solution with HCl. TEM elemental mapping shows a direct evidence of chlorides presenting throughout the porphyrin nanofibers. The fluorescence of TCPP was quenched when the porphyrin formed nanoplates and was recovered when nanofibers were assembled. Furthermore, the porphyrin nanofibers exhibit supramolecular chirality while the nanoplates were achiral. The photoluminescence and chiroptical properties of TCPP nanoplates and nanofibers indicate they might be used for optical memory devices. By simply changing the pH, the fluorescence and chirality of the porphyrin assemblies can be turned “on” and “off”. For example, the fluorescence and chirality of TCPP can be turned on by lowering the pH to 1 to form nanofibers, and can be turned off by increasing the pH to 3 to form nanoplates. The switching is reversible since this process involves protonation and deprotonation of the core nitrogens of TCPP along with intercalation and dissociation of chlorides. We also found that the conductivity of TCPP nanofibers decreased reversibly with increased light exposure. Other applications of the porphyrin nanofibers may be optical transistors, sensors, and solar cells.

CHAPTER IV

THE COUNTER ION EFFECT OF SELF-ASSEMBLY OF PORPHYRIN NANOSTRUCTURES

4.1. Synopsis

The counterion effect of self-assembly of porphyrin nanostructures by acidifying TCPP in aqueous solution was examined. In the last chapter, porphyrin nanofibers were obtained by titrating TCPP with HCl. The formation of the nanofibers was found to be due to the interaction between the porphyrin dications and chlorides. Herein, instead of using HCl, we used HBr to acidify TCPP in order to investigate the influence of the identity of counter-anions on the morphologies and photoluminescence properties. Our experimental results show that the morphologies of the porphyrin aggregates in aqueous solution at pH lower than 2 are anion dependent. Above pH 2, once the carboxylate groups of the porphyrin were protonated, TCPP self-assembled into nanoplates via J-aggregation. The XPS results showed no presence of halides in the assemblies and the absorption spectra of the aggregates were identical regardless of the difference of acids. At pH lower than 2, protonation of the core nitrogens of the porphyrin formed the TCPP dication, which further interacted with the anions. In this condition, the AFM and SEM results reveal that titrating TCPP with HBr formed porphyrin nanoparticles at pH 2 and bundles of nanowires at pH 1. The XPS data showed the presence of Br within the nanowires and nanoparticles, respectively. Moreover, the nanowires and nanoparticles exhibit difference in the absorption shifting in the UV-vis spectrum. This indicates the porphyrin stacked differently when different anions intercalated into the assemblies.

4.2. Introduction

Although self-assembly of porphyrin nanostructures been investigated in recent years, there are only few reports in the literature about utilizing porphyrin dications as building blocks to assemble well ordered structures. The assemblies of free-base 5,10,15,20-tetrakis(3.5-dimethoxyphenyl)-21*H*,23*H*-porphine dications on various acidic subphases were reported by Zhang and coworkers.[194] The morphologies, absorption spectrum and CD spectrum of the porphyrin assemblies were found to be counterion dependent. Moreover, the absorption spectra of tetra(*p*-carboxlyphenyl)porphine (TCPP) aggregates were intensively studied by Doan *et al*. Their results showed that in the aqueous solution at pH ~1 the absorption peaks of the porphyrin red-shifted when being titrated with HCl and blue-shifted when being titrated with HNO_3, indicating the porphyrin dications stacked differently as the counterions presented in the solution were varied.

In Chapter III, we demonstrated that self-assembly of highly crystalline nanofibers were obtained by acidifying TCPP with HCl. The results of XPS and TEM elemental mapping reveal chlorides intercalated within the nanofibers. When the carboxylate groups were protonated at pH lower than 5, TCPP with neutral charge self-aggregated into nanoplates, which greatly quenched the emission of the porphyrin. Protonation the core nitrogens of TCPP formed the porphyrin dications which interacted with chlorides possibly through columbic interaction. This likely increased the spacing between the porphyrins, which limited the self-quenching and resulted in the recovery of their fluorescence.

Herein, HBr was used to acidify TCPP in order to study the counterion effect of the self-assembly. The morphologies of the assemblies at different pH of HBr were characterized using AFM, SEM and TEM. The absorption spectra, CD spectra and XPS analysis of the assemblies were obtained to shed light on their growing mechanism and the arrangement of the molecules within the assemblies. Moreover, the photoluminescence properties of the porphyrin assemblies were investigated using static and time-resolved fluorospectroscopy.

4.3. Experimental Detail

Self-assembly of TCPP nanostructures was carried out by acidifying TCPP in aqueous solution with HBr. Typically, a 1 mM solution of TCPP in 0.2 M NH_4OH solution was acidified by adding 1 M HBr solution dropwise while stirring at room temperature until the pH decreased to a certain pH. The solution was stirred for another 1 hour after the titration. The aggregates formed at different pH were obtained and further characterized by UV-vis spectroscope, spectrafluorometer, XPS, CD spectrometer, AFM, and SEM. The analysis methods were described in Chapter III.

4.4. Results and Discussion

Acidification of TCPP in NH_4OH solution with HBr shows an equivalence point at around pH 5 in the titration curve, indicating the protonation of the carboxylate groups of TCPP has occurred. The TCPP aggregates formed within the solution at various pH below the equivalence point were first characterized by AFM and UV-vis spectroscopy to investigate their morphologies and the absorption properties, respectively. The AFM images show that TCPP formed the structure of nanoplates at around pH 4 and pH 3, as shown in Figure 4.1a and b, respectively. The absorption spectrum of the aggregates formed at pH 4 shows a absorption peak at 414 nm and a new peak at 437 nm (Figure 4.2a red line). The absorption peak at 414 nm can be attributed to the Soret band of TCPP monomers, while the new absorption of 437 nm can be attributed to the red-shift of the Soret band, which was due to the J-aggregation of the porphyrins. At pH 3, the Soret band of the the porphyrin red-shifted to 455 nm (Figure 4.2a green line). This reveals that all the TCPP monomers aggregated to form nanoplates.

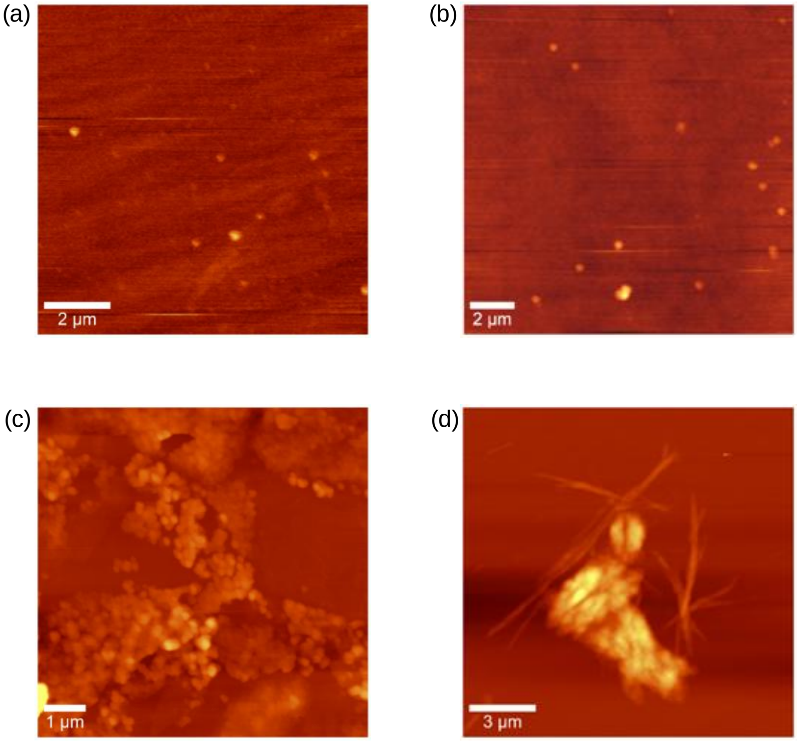

Figure 4.1. The AFM images of TCPP assembled through acidification with HBr at (a) pH 4, (b) pH 3, (c) pH 2, (d) pH 1.

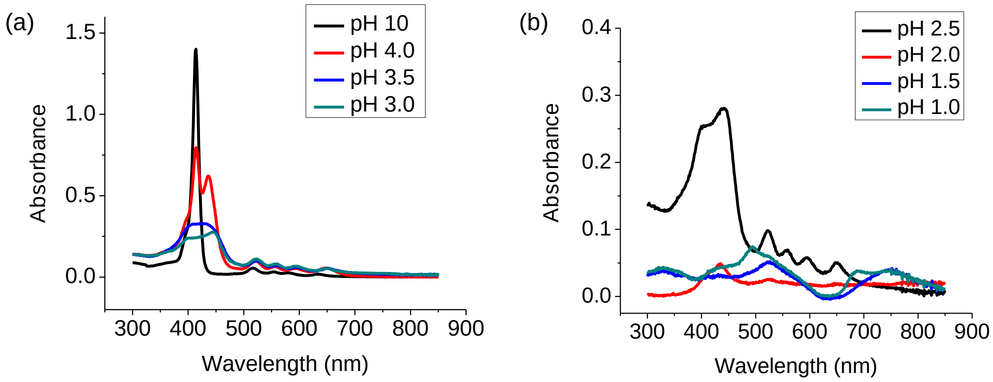

Figure 4.2. The absorption spectrum of TCPP solution after being titrated with HBr to certain pH.

The AFM results show that TCPP formed nanoparticles at pH 2. Figure 4.1c shows TCPP nanoparticles deposited on Si. Moreover, the absorption spectrum shows that the Q bands of the porphyrin collapsed, indicating the core nitrogens of TCPP had been protonated. The Soret band shifted back to 435 nm, indicating the dipole-dipole interaction between the porphyrins decreased. It is possible that protonation of the core nitrogens of TCPP formed the porphyrin dications which interacted with bromides through columbic interaction. The intercalation of bromide within the porphyrin assembly increased the spacing between the porphyrin planes and thus decreased their dipole-dipole interaction.

The AFM image shows that TCPP self-assembled into bundles of nanowires at pH 1, as shown in Figure 4.1d. The morphology of the nanowires was further characterized by SEM. Figure 4.3 shows the SEM images of the nanowire bundles deposited on Si. Furthermore, the absorption spectrum of the nanowires shows a broad Soret band at around 495 nm. The red-shift of the Soret band indicates the nanowires were assembled via the J-aggregation of the porphyrin. The large shift of the Soret band reveals the strong dipole-dipole interactions between the porphyrin.

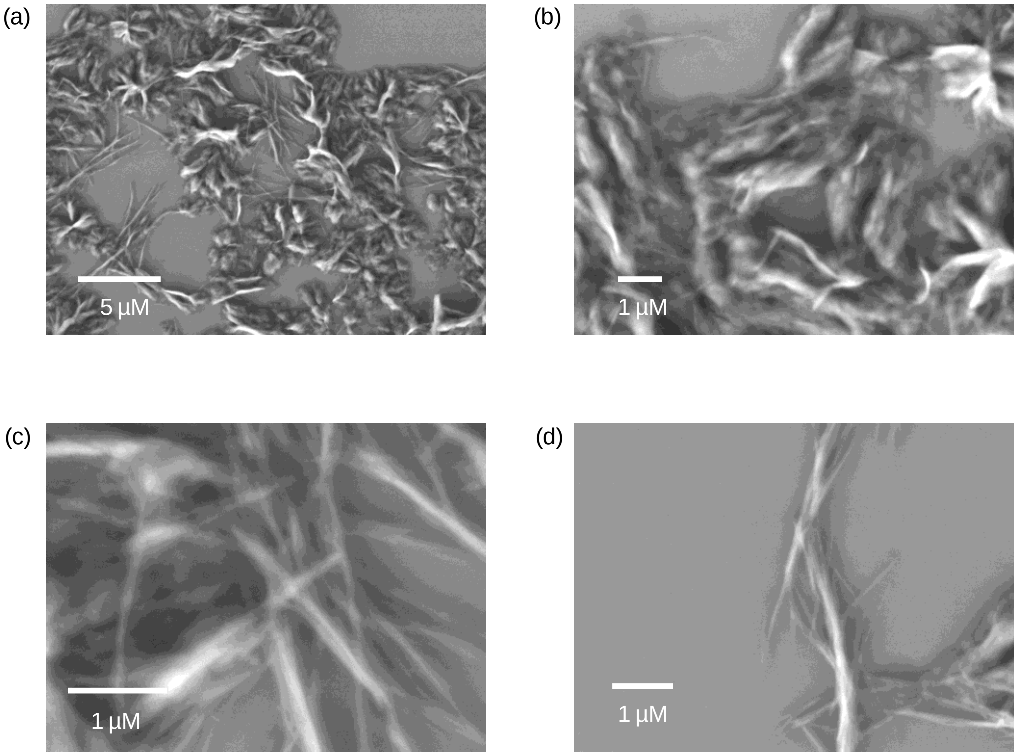

Figure 4.3. SEM images of TCPP nanowire bundles deposited on Si.

To confirm whether bromides were intercalated within the nanoplates or the nanowires, the samples were further analyzed by XPS. The XPS result of TCPP nanoplates shows almost no Br signal, revealing that bromide did not anticipate the assembly of the nanoplates (Figure 4.4a). The XPS data of the nanowires shows the Br signal at around 66.5 eV, implying the presence of Br within the porphyrin nanowires

(Figure 4.4b). This clearly indicates that the nanowires were assembled through the interaction between TCPP dications and bromides.

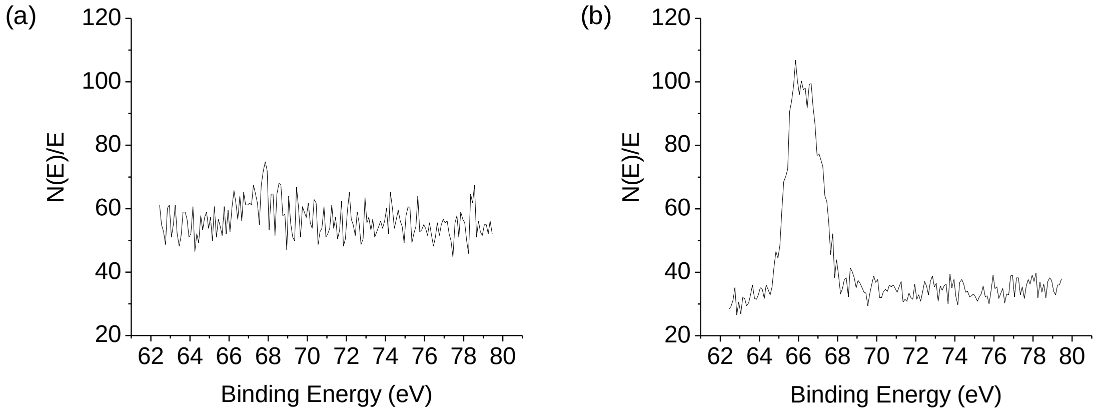

Figure 4.4. XPS of (a) TCPP nanoplates and (b) TCPP nanowire bundles in the spectral range of Br 2P binding energy.

To investigate the photoluminescence properties of the TCPP assemblies, the emission spectrum of the assemblies formed in HBr solution at various pH were measured. Figure 4.5 shows the emission spectrum of TCPP anions in NH_4OH solution at pH 10, TCPP nanoplates in HBr solution at pH 3, TCPP nanoparticles in HBr solution at pH 2 and TCPP nanowires in HBr solution at pH 1. The emission spectrum of TCPP anions in NH_4OH solution shows the fluorescence of the porphyrin with the emission maxima at 613 and 658 nm (Figure 4.5 black line). The emission spectrum of the porphyrin nanoplates in pH 3 HBr solution shows a week fluorescence peak at 680 nm (Figure 4.5 red line). The absorption spectrum of the porphyrin nanoplates shows the Soret band largely red-shifted, indicating there were strong dipole-dipole interactions between the porphyrins (Figure 4.2a green line). The strong dipole-dipole interaction between the porphyrins implies the porphyrins stacked closely, which may result in their self-quenching. The fluorescence of TCPP was strongly enhanced once the nanoparticles were assembled in the pH 2 HBr solution (Figure 4.5 blue line). The collapse of Q bands in the absorption spectrum indicates TCPP formed porphyrin diacids which could further interact with bromides (Figure 4.2b red line). It is likely the intercalation of bromides into the porphyrin assemblies increased the spacing between the porphyrin planes, which resulted in the recovery of the fluorescence of the porphyrins. The small red-shift of the Soret band in the absorption spectrum also implies the weak dipole-dipole interactions between the porphyrins possible resulted from their large spacing. The fluorescence of the porphyrin was largely quenched once the porphyrin nanowires were formed in the pH 1 HBr solution (Figure 4.5 green line). The absorption spectrum of the nanowires shows the Soret band largely red-shfited, revealing the strong dipole-dipole interactions between the porphyrins within the nanowires (Figure 4.2b green line). This indicates the rearrangement of the TCPP dications and bromides may occur and decreased the spacing between the porphyrin planes, which resulted in the self-quenching of the porphyrins.

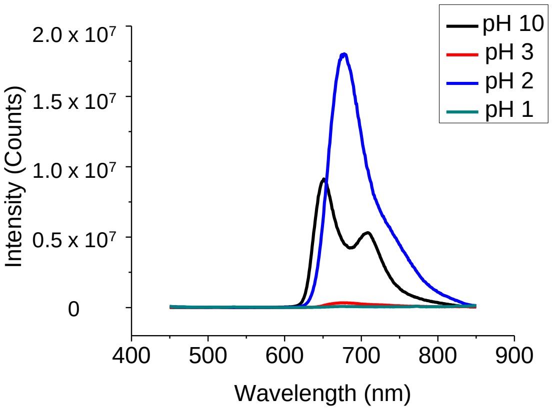

Figure 4.5. The emission spectrum of TCPP in pH 10 NH_4OH solution and in pH 3, pH 2 and pH 1 HBr solutions.

To study the chiroptical properties of the porphyrin assemblies, the CD spectra of the assemblies in HBr solutions at various pH were measured. The porphyrin nanoplates formed in pH 4 and pH 3 HBr solutions show no signal in the CD spectrum (Figure 4.6 red line and blue line, respectively), indicating the nanoplates were achiral. The porphyrin nanoparticles assembled in pH 2 HBr solution shows cotton effect in the CD spectrum (Figure 4.6 green line). This reveals the nanoparticles exhibited supramolecular chirality possibly due to the interaction between TCPP dications and bromides. The cotton effect became more severe once the porphyrin nanowires were formed in pH 1 HBr solution, revealing the nanowires also had supramolecular chirality.

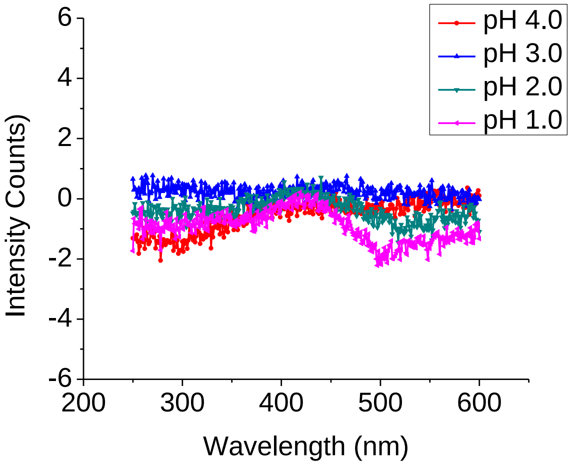

Figure 4.6. CD spectra of TCPP assemblies in HBr solutions at various pH.

4.5. Summary

The counterion effect of self-assembly of TCPP nanostructures through direct acidification was studied. It was found that the identity of counterions does not affect the morphologies and optical properties at pH above 2. Protonation of the carboxylate groups of TCPP with HCl and HBr both induced the J-aggregation of TCPP. The morphologies of the J-aggregates in both conditions were characterized by AFM and were determined to be nanoplate structures. When pH was lower than 2, protonation of the core nitrogens of TCPP formed the porphyrin dications which interacted with the counterions in the solution, and the structures of the porphyrin assemblies were found to be counterion dependent. While the dications interacted with chlorides to assemble into nanofibers in pH 1 and pH 2 HCl solutions, the dications interacted with bromides to form nanoparticles in pH 2 HBr solution and nanowires in pH 1 HBr solution. The absorption spectrum of the porphyrin reveals the weak dipoe-dipole interactions between the porphyrins within the nanoparticles and the strong dipole-dipole interactions between the porphyrins within the nanowires. This indicates TCPP dications stacked differently in pH 2 and pH 1 HBr solutions and strongly influence their photoluminescence properties. The nanoparticles formed in pH 2 HBr solution intensively fluoresced, while the emission of the nanowires formed in pH 1 HBr solution was largely quenched. Furthermore, the porphyrin nanoparticles and the nanowires formed in HBr solution both exhibited supramolecular chirality. Without the intercalation of bromides or chlorides, the porphyrin nanoplates assembled at pH 3 and 4 were achiral. Intercalating the counterions such as chloride es and bromides both resulted in the formation of chiral supramolecular assemblies, although the characteristic of the CD spectrum of the assemblies were counterion dependent. Our results show that intercalating different types of counterion into the porphyrin assemblies may change the arrangement of the porphyrins and the dipole interactions between the porphyrins, which greatly influences the morphologies, the photoluminescence properties and the chirality of the assemblies.

CHAPTER V

MEMORY EFFECTS OF PORPHYRIN THIN FILMS

5.1. Synopsis

In Chapter III, we have shown that porphyrin nanofibers can be prepared by direct acidification of TCPP with HCl. In acidic conditions below pH 2, the nanofibers are constructed through the interaction between the protonated core nitrogens of the TCPP and chloride counterions. Between pH 2-4 the porphyrins are neutral and form nanoplates through J-aggregation without the counterion participation. Here we describe the memory effect of TCPP thin film based on the structural transformations of TCPP thin films and their associated fluorescence. The porphyrin nanoplates were deposited on a Si wafer modified with an oxidized OTS monolayer, which enhanced adhesion between the nanofibers and the surface. After drying, the porphyrin nanoplates formed a thin film with thickness around 500 nm on the wafer. Immersing the thin film in a pH 1 HCl solution protonates the core nitrogens of the porphyrins, interacting with chlorides, causing the porphyrins to transform into nanofiber structures on the surface, and shifting their fluorescence. Immersing the porphyrin nanofibers into a pH 3 HCl solution deprotonates the core nitrogens of the porphyrins, releasing chlorides. This converts the nanofibers back into nanoplates and shifts the fluorescence back to the original wavelength. Therefore, the fluorescence of the porphyrin thin film can be changed reversibly. By utilizing the water meniscus between an AFM tip and the surface, here we illustrate that deprotonation of the porphyrin can be carried out within a selective region in micrometer scale, allowing fluorescence patterns to be written by AFM, and read by a confocal microscope. Furthermore, the fluorescence patterns can then be subsequently erased by immersing the thin film in a pH 1 HCl solution.

5.2. Introduction

In recent years, optical memory devices such as compact disks (CDs) and digital versatile disks (DVDs) have brought great convenience to our daily life because of their applications in storing bit data for music, photographs, videos, etc. The data recording on the disk is done by illuminating a light sensitive material within selective regions. The resulting patterns can be read by a laser beam which is selectively reflected by the recording materials. The recording density of these systems depends on the spot size on the recording materials. Due to the diffraction of light, the recording density is limited by the wavelength of the laser. As current optical memory techniques have approached to this limitation, developing new methods for optical memory recording is desirable. Recently there are various new alternative optical technologies being investigated, including multilayer reflective media,[207,208] near-field recording,[209-211] volume holography,[212-215] two photon storage[216-219] and others.

Here we demonstrate that porphyrin thin films can be used as recording medium for optical memory devices, where the fluorescence wavelength of the thin films can be changed by pH. Data can be written by an AFM tip on a selective region through the interaction between the porphyrin film and the water meniscus between the tip and the surface. The resulting local fluorescence change on the thin film can then be read by a confocal microscope.

The idea of writing on the porphyrin thin films was inspired by dip-pen nanolithography (DPN), which was developed by Mirkin *et al*.[173] DPN is a scanning probe lithography technique that is used to generate patterns of monolayers of molecules on the substrate. For DPN, the tip of an AFM is used as a “pen”, which is coated with the molecules (*e.g.* alkanethiol) as “ink”. The molecular-caoted tip is then brought into contact with the substrate (*e.g.* gold) as a “paper”. The contact of the tip and the substrate allows the molecules to be delivered to the surface through a water meniscus between the tip and the surface, which plays a key role in DPN. Therefore, patterns of alkanethiol monolayers can be created on a substrate. Figure 5.1a and b show that patterns of 1-octadecanethiol on a gold surface, which generated by DPN. Moreover, the size of the water meniscus is affected by the humidity of the environment and can strongly affect the size of the feature.[220,221] In our experiment, the water meniscus between an AFM tip and the substrate was utilized to locally deprotonate the TCPP diacids, which were used as the building blocks along with chlorides to assemble a thin film of porphyrin nanofibers (Chapter III). Deprotonating the porphyrin diacids by the water meniscus results in the neutral porphyrin and the releases of chlorides from the porphyrin assemblies. This leads to the porphyrin fluorescence to be changed in a confined region on the thin film, and fluorescence patterns can be created. Moreover, the fluorescence patterns can be erased by immersing the thin film in HCl solution, which allows the porphyrin to be re-protonated to form the nanofibers and changes the porphyrin fluorescence back to the original wavelength.

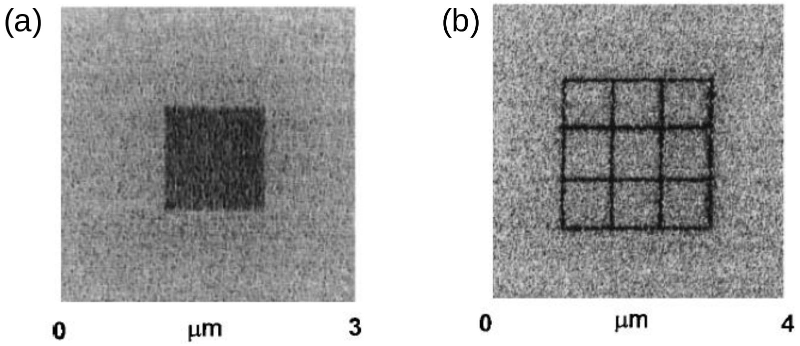

Figure 5.1 (a) and (b) are the lateral force images of 1-octadecanethiol patterns created on a gold substrate by DPN lithography. (Reproduced from ref. [173] with the permission of the copyright holders.)

5.3. Experimental Detail

5.3.1. Preparation of Porphyrin Nanoplate Solution

10 ml of a 1 mM solution of TCPP in 0.2M NH_4OH was acidified by adding 1 M HCl solution dropwise while stirring at room temperature until the pH decreased to 3. The solution was stirred for another 1 hour after the titration. To remove ammonium ions, which can form salts with chlorides after drying on the surface, the suspension was washed with 10 ml of pH 3 HCl solution ten times using centrifugation. The precipitates were resuspended with 10 ml of pH 3 HCl solution after the removal of ammonium ions. The XPS spectrum shows no signal of NH_4Cl which has a binding energy of 401.5 eV for N_{1s}, indicating the ammonium ions have been completely removed from the porphyrin nanoplate solution (Figure 5.2).

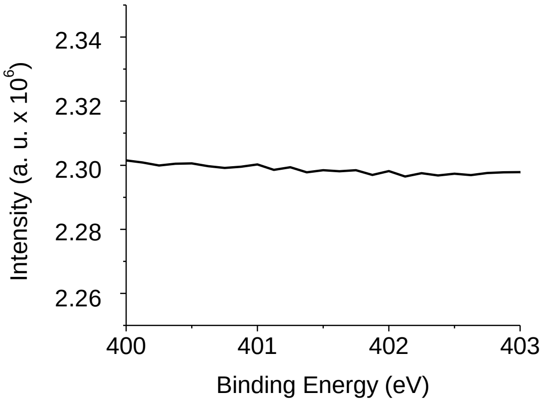

Figure 5.2. The XPS spectrum of the porphyrin nanoplates on Si. The spectrum covered the N_{1s} energy range of NH_4Cl.

5.3.2. Preparation of Porphyrin Thin Films on Si

The porphyrin nanoplate solution was deposited on a Si wafer to form a thin film. The wafer was modified with UV-ozone oxidized octadecyltrichlorosilane (OTS) monolayer prior to use in order to enhance the adhesion between the porphyrin nanoplates and the surface. Oxidizing the OTS monolayer converts the terminal methyl groups into carboxylic acids, which form hydrogen bonds with the porphyrin. Without the monolayer the porphyrin thin film would not remain adhered to the surface when the sample was immersed in HCl solution. To modify the surface with OTS, a 5 mm × 5 mm piece of silicon wafer was first cleaned in a mixture of 12 mL H_2O, 3 mL of 30% H_2O_2 and 3 mL concentrated NH_4OH at 85 °C for 40 min (RCA cleaning), and then rinsed with copious amounts of high purity H_2O (18.2 MΩ·cm) and dried under a jet of streaming nitrogen. This process also generated a layer of hydroxyl groups on the Si wafer.[222] The cleaned and oxidized Si wafer was then immersed in a 0.25 mM OTS in hexanes with sonificated at room temperature for 2 h. The sample was then washed in hexanes, water, ethanol, and dried with N_2. The OTS coated Si wafer was then rastered underneath a UV lamp at a distance of about 1 mm for 10 minutes. The UV-lamp has emission wavelengths of 254 and 285 nm, which produce ozone and oxidize the OTS to generate carboxylic acid groups.[223] The oxidized OTS modified Si substrate was then rinsed with copious amounts of water and dried with N_2. The porphyrin thin film was formed by dropcasting 20 μL of the porphyrin nanoplate solution onto the oxidized OTS modified Si surface and air dried. The sample was then immersed in pH 1 HCl solution for 10 minutes and then dried under N_2. The immersion in pH 1 solution converts the thin film of porphyrin nanoplates into a thin film of porphyrin nanofibers. The thickness of the resulting thin film was found to be ~477 ± 69 nm, as determined by AFM.

Although treating the wafer with RCA cleaning process produced isolated or vicinal silanol groups,[222] which could have hydrogen bonding with the carboxylic acids of TCPP, the porphyrin thin film easily fell off from the silanol-rich Si surface once the substrate was immersed in HCl solution. It is likely that the RCA-treated Si surface only has weak interactions with TCPP due to the hydrogen bonds formed between the silanol's hydrogen and the oxygen which belongs to the carboxylic acid groups of the porphyrins (Figure 5.3a). We suspect that the silanol's oxygen, which is a hydrogen bonding acceptor, might be hindered in either isolated or vicinal conformation, and does not participate in the formation of hydrogen bonds with the porphyrin. On the other hand, we observe that the porphyrin thin film was able to adhere on the Si wafer in HCl solution once the surface was modified with an UV-ozone oxidized monolayer, which had carboxylic acid end groups. It is possible that the carboxylic acid groups of the monolayers form dimers with the carboxylic acid groups of TCPP through hydrogen bonding, which stabilize the porphyrin thin film on the substrate (Figure 5.3b).

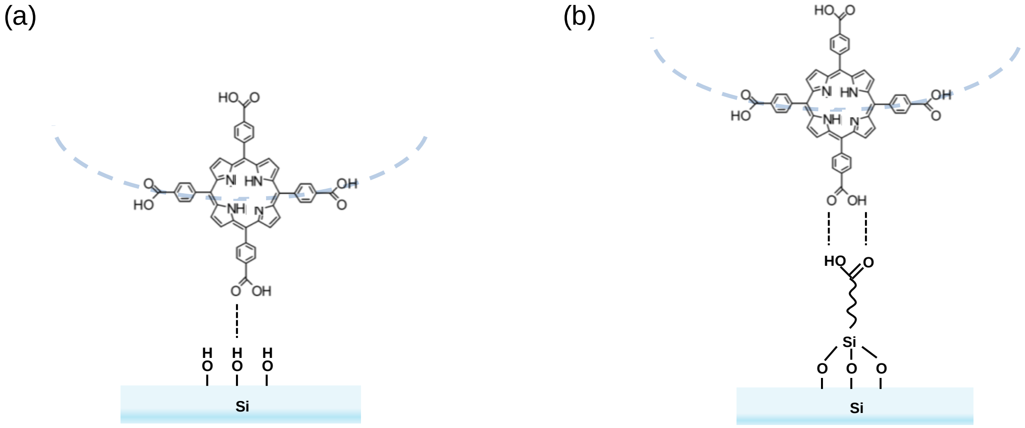

Figure 5.3. Schematic diagrams showing the hydrogen bonding between the porphyrin of TCPP nanoplate thin film and (a) silanol on Si, (b) COOH-terminated OTS on Si.

5.3.3. Writing on the Porphyrin Thin Film by AFM

The water meniscus between the AFM tip and the surface of the thin film was used to deprotonate and change the fluorescence wavelength of the porphyrin nanofiber thin film in a selective region. In order to increase the hydrophilicity of the tip, the tip was immersed in a mixture of 4 mL H_2O, 1 mL of 30% H_2O_2 and 1 mL concentrated NH_4OH for 5 minutes and then immersed in ultra-clean water for 1 minute and N_2 dried prior to use. Deprotonating the porphyrin thin film using AFM was done in contact mode using an Nscriptor DPN system developed by NanoInk. The environmental conditions during the wetting were controlled in a system chamber, which housed the entire DPN stage. The temperature and the humidity sensors monitored the enclosed environment in real time, and both parameters were controlled by PID feedback loops, which connected to the user PC. During the experiments, the temperature was kept at room temperature (~25^{o}C), and the humidity was controlled at 30-60%.

5.4. Results and Discussion

The emission spectrum of the porphyrin thin film after being immersed in pH 1 or pH 3 HCl solution was measured using confocal fluorescence microscopy. The thin film was prepared by drop-casting the TCPP nanoplate solution onto a UV-ozone oxidized OTS-Si surface. The emission spectrum of the porphyrin nanoplates measured in air shows the fluorescence peak with the maximum intensity at 654 nm. The thin film was immersed in a pH 1 HCl solution for 1-60 minutes. After the immersion, the thin film was taken out from the solution, blow dry with N_2 and the emission spectrum of the thin film was again measured in air. Figure 5.4a is the emission spectrum of the porphyrin thin film before and after being immersed in pH 1 HCl solution for 1 hour. The emission spectrum shows that the fluorescence peak of the porphyrin thin film shifted to 714 nm after the immersion. The correlation between the intensities of fluorescence peaks at 654 nm and 714 nm versus the immersion time is shown in Figure 5.4c. The intensity of the fluorescence peak at 654 nm decreased gradually, while the intensity of the peak at 714 nm increased gradually during the immersion in pH 1 HCl. The changing of the fluorescence of the porphyrin thin film is reversible. The fluorescence peak back shifted from 714 nm to 654 nm when the thin film was immersed in a pH 3 HCl solution (Figure 5.4b). Figure 5.4d shows the fluorescence intensities at 654 nm and 714 nm versus the immersion time in pH 3 HCl. The fluorescence peak at 654 nm increased gradually when the thin film was immersed in the solution. However, the decrease of the fluorescence at 714 nm was not obvious due to the shoulder of the new peak.

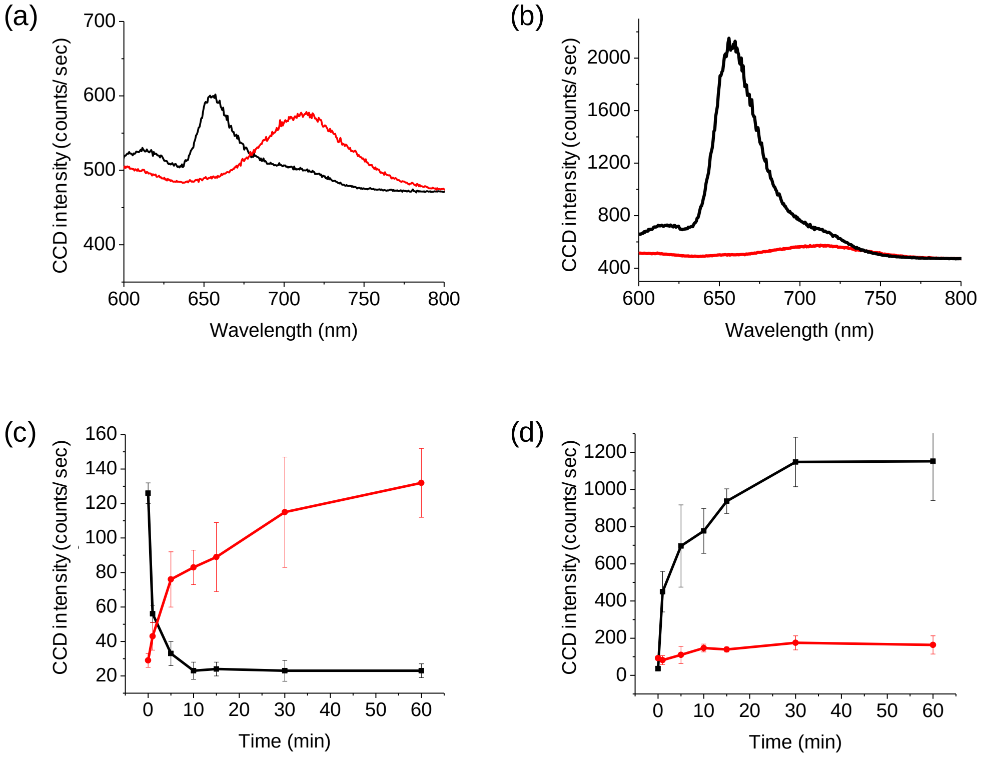

Figure 5.4. (a) Fluorescence spectrum of thin film of TCPP nanoplates before (black line) and after being immersed in pH 1 HCl solution for 1 hour (red line). (b) Fluorescence spectrum of thin film of TCPP nanofibers before (red line) and after being immersed in pH 3 HCl solution for 1 hour (black line). (c) Intensities of fluorescence peaks of the porphyrin thin film at 654 nm (black line) and 714 nm (red line) versus the immersion time in pH 1 HCl solution. (d) Intensities of fluorescence peaks of the porphyrin thin film at 714 nm (black line) and 654 nm (red line) versus the immersion time in pH 3 HCl solution. The error bars in (c) and (d) are the standard deviation based on five data points.

The porphyrin thin film was characterized by SEM in order to investigate its morphology. The SEM image of the as prepared thin film shows the aggregation of TCPP nanoplates (Figure 5.5a). The SEM image of the thin film after being immersed in the pH 1 HCl solution for 1 hour shows the formation of nanofibers which had lengths between 500 nm and 3 μm and diameters between 50 to 200 nm (Figure 5.5b). This indicates the porphyrin nanoplates transformed to nanofibers during the immersion in pH 1 HCl solution. Thus the emission at 654 nm in the spectrum can be attributed to the fluorescence of TCPP nanoplates, while the emission at 714 nm can be attributed to TCPP nanofibers. Immersing the thin film in the pH 1 HCl solution for 2 hours led to the aggregation of the nanofibers, as shown in Figure 5.5c and d. Moreover, immersing the thin film in the pH 1 HCl solution overnight resulted in the formation of large dimension porphyrin fibers which had length between 30 to 120 μm and diameter between 100 nm to 1 μm (Figure 5.5e). The cross-section of the porphyrin fibers was observed to be rectangular (Figure 5.5f). The structural transformation can be explained that when the thin film was immersed in the pH 1 HCl solution, the core nitrogens of TCPP were protonated and interacted with chlorides, which induce the porphyrin to assemble into nanofibers. This process is reversible since immersing the thin film of porphyrin nanofibers in the pH 3 HCl solution deprotonated the core nitrogen and caused the dissociation of chlorides from the porphyrin. The resulting neutral TCPP tends to form nanoplates through the J-aggregation of the porphyrin (see Chapter III). The XPS results reveal the lack of chlorides of the as-prepared thin film of TCPP nanoplates (Figure

5.6a) and the presence of chlorides within the thin film after it was immersed in pH 1 HCl solution to form TCPP nanofibers (Figure 5.6b).

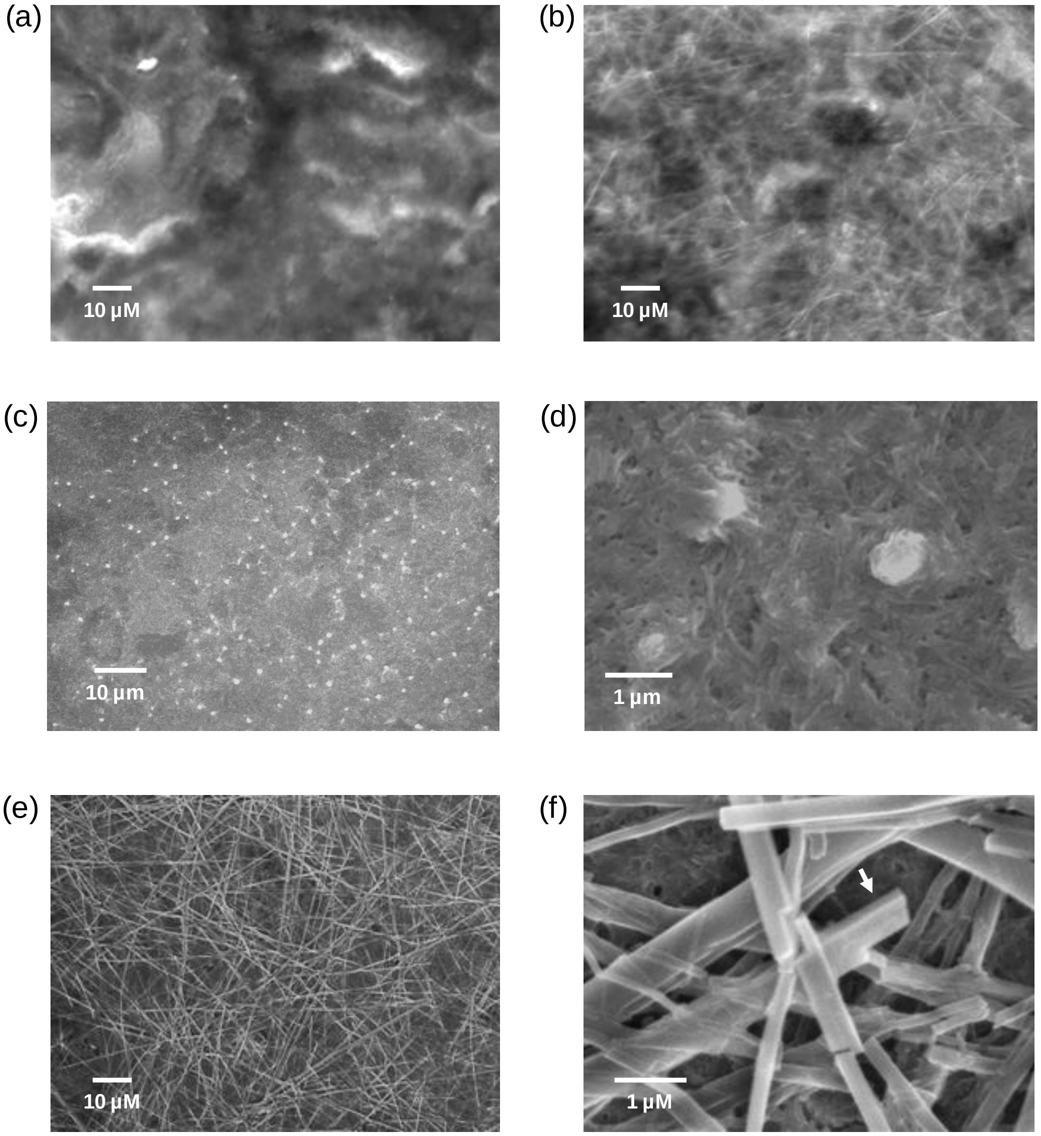

Figure 5.5. SEM images of (a) the as prepared porphyrin nanoplate thin, and the thin film after being immersed in pH 1 HCl for (b) 1 h, (c) and (d) 2 h, (e) and (f) 1 day. The arrow in (f) points at a tilted nanofiber which shows two faces of the fibers, revealing the shape of the cross-section of the nanofiber is square.

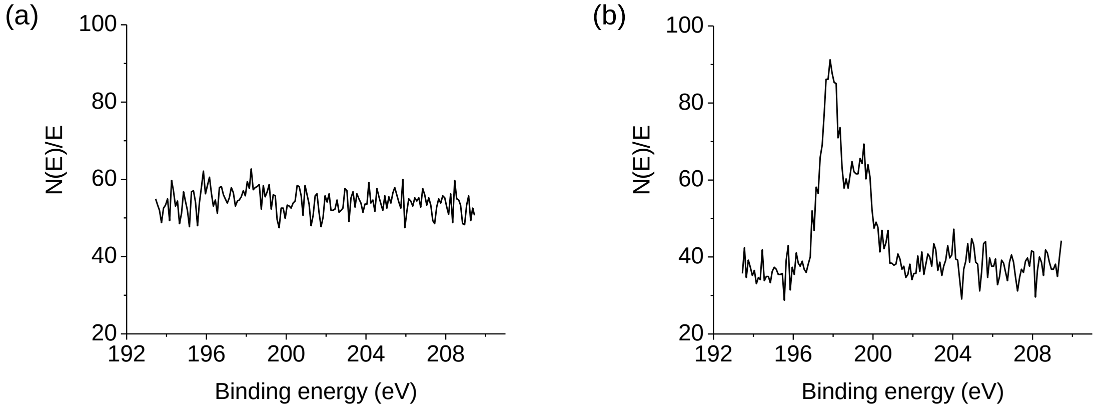

Figure 5.6. XPS results of (a) as prepared thin film of porphyrin nanoplates, and (b) thin film of porphyrin nanofibers formed in pH 1 HCl solution.

Our experimental results indicate TCPP thin film exhibits optical switching characteristic. The fluorescence of the porphyrin thin film at specific wavelength (654 or 714 nm) can be turned on or turned off by immersing the thin film within a HCl solution with controlled pH. For example, the as prepared thin film of TCPP nanoplates fluoresces at 654 nm (Figure 5.7a), and the fluorescence can be turned off by immersing the thin film in a pH 1 HCl solution (Figure 5.7b). Immersing the thin film in pH 1 HCl solution transforms the porphyrin nanoplates to nanofibers which emit at 714 nm (Figure 5.7c). Therefore, the fluorescence at 654 nm of the thin film is diminished. Immersing the thin film of TCPP nanofibers in a pH 3 HCl solution changes the nanofibers back to nanoplates and the emission at 654 nm is recovered (Figure 5.7 d). Figure 5.8a shows the emission spectrum of turning the fluorescence at 654 nm on (red line) and off (blue line) by this process. Figure 5.8b shows the changes of fluorescence intensity at 654 nm during four on-off cycles.

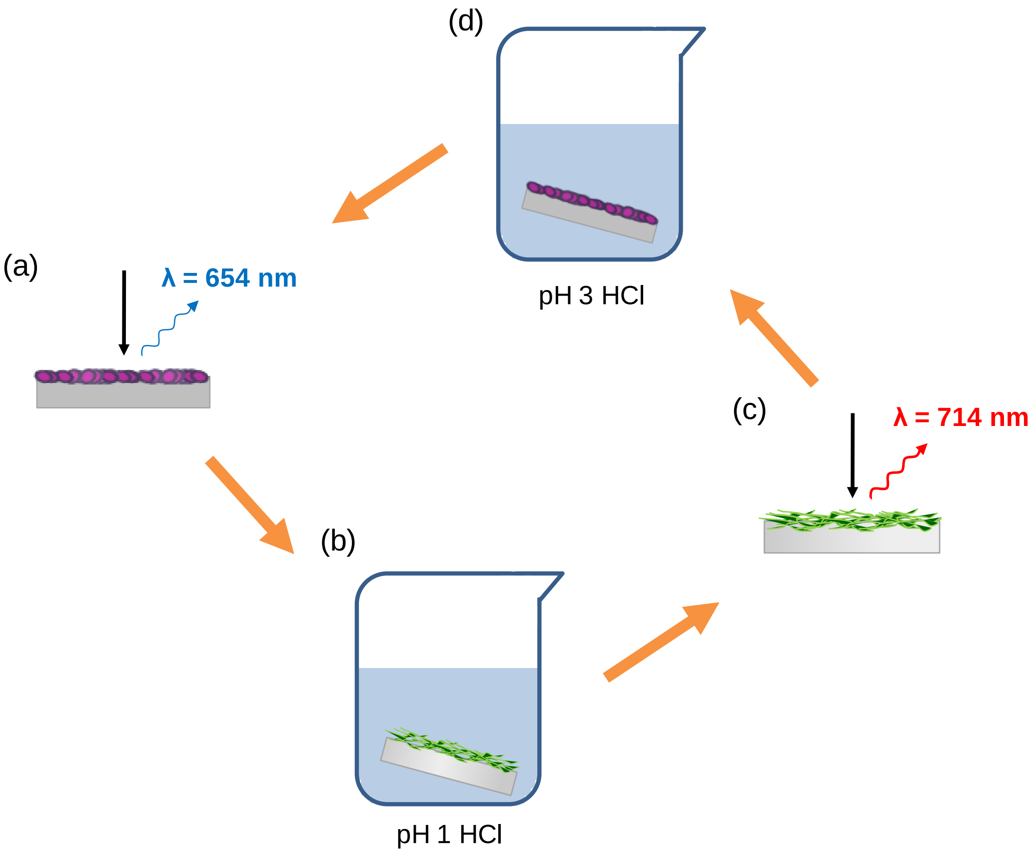

Figure 5.7. Schematic diagram showing the optical switching process of TCPP thin film. (a) The thin film of TPP nanoplates fluoresces at 654 nm in air. (b) Immersing the thin film in a pH 1 HCl solution transforms the nanoplates to nanofibers. (c) The thin film of TPP nanofibers fluoresces at 714 nm in air. The fluorescence intensity at 654 nm diminishes after the porphyrin nanofibers are formed. (d) Immersing the thin film in a pH 3 HCl solution transforms the nanofibers back to nanoplates.

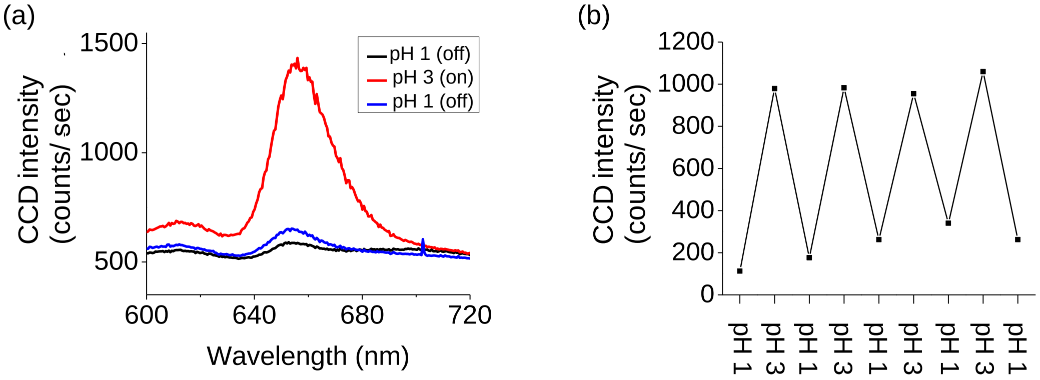

Figure 5.8. (a) Emission spectrum of TCPP thin film, showing the fluorescence at 654 nm could be turned on and off after the thin film was immersed in pH 3 for 5 minutes and pH 1 HCl solutions for 10 minutes, respectively. (b) Variation of the fluorescence intensity of the porphyrin thin film at 654 nm after being immersed in pH 1 or pH 3 HCl solution.

The optical memory property of TCPP thin film was also investigated. To apply the porphyrin thin film on optical memory technology, fluorescence patterns as the data bits must be written on the thin film. Here the water meniscus between an AFM tip and the surface of the porphyrin thin film is utilized to change the emission thin film in a confined area. This is inspired by dip-pen lithography, in which water meniscus formed between an AFM tip and the surface of the substrate when the humidity is high enough and is utilized as the media to transport molecules from the tip to the surface. In our experiment, the thin film of TCPP nanofibers is used as the recording materials and the water meniscus between the tip and the surface is used to locally disassemble the nanofibers. In liquid phase TCPP nanofibers are not stable when pH is higher than 2 since deprotonation of the core nitrogens of TCPP occurs and leads to the dissociation of chlorides from the porphyrin (see Chapter III). This changes the fluorescence of the porphyrin from 714 nm to 654 nm. Therefore, on the porphyrin thin film, the fluorescence of the region scanned by the AFM tip will be changed (Figure 5.9).

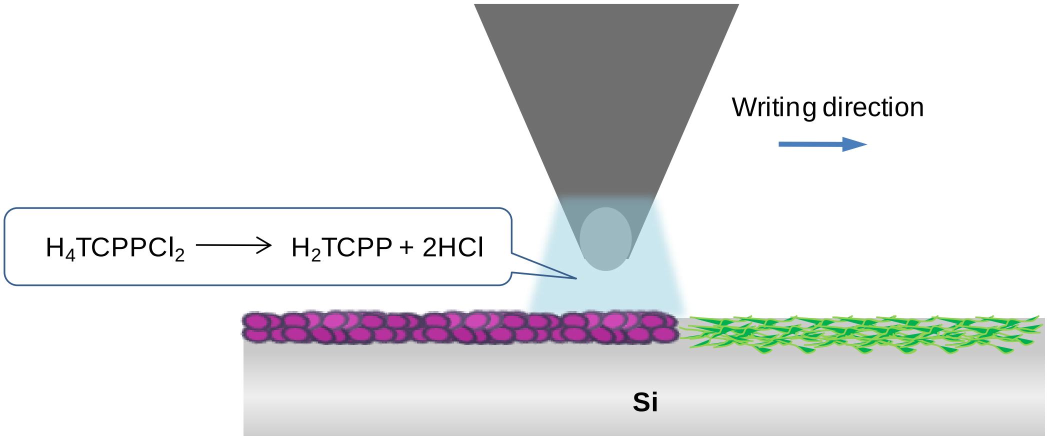

Figure 5.9. Schematic diagram of changing the morphology and emission of TCPP thin film using water meniscus between an AFM tip and the surface of the thin film.

The thin film of TCPP nanofibers was prepared by immersing the thin film of TCPP nanoplates within a pH 1 HCl solution for 10 minutes. After the immersion, the emission spectrum showed the disappearance of the fluorescence of the nanoplate at 654 nm and the appearance of the fluorescence of the nanofiber at 714 nm. In the next step, a 10 by 10 µm^2 region on the thin film was scan by AFM in contact mode at room temperature and ~40% humidity. The scanning speed was controlled at 1.0 µm/s. After the scanning the surface was characterized using confocal. The fluorescence image and spectrum shows the region scanned by the tip on the thin film fluoresced at 654 nm while no emission at the same wavelength appeared at the background area (Figure 5.

10a and c). This reveals the porphyrin nanofibers contact with the water meniscus have been disassembled and the porphyrins self-assembled into nanoplates. Furthermore, the fluorescence signal generated by the water meniscus is erasable. Immersing the thin film in a pH 1 HCl solution resulted in reformation of the nanofibers, which diminished the fluorescence at 654 nm (Figure 5.10b and d).

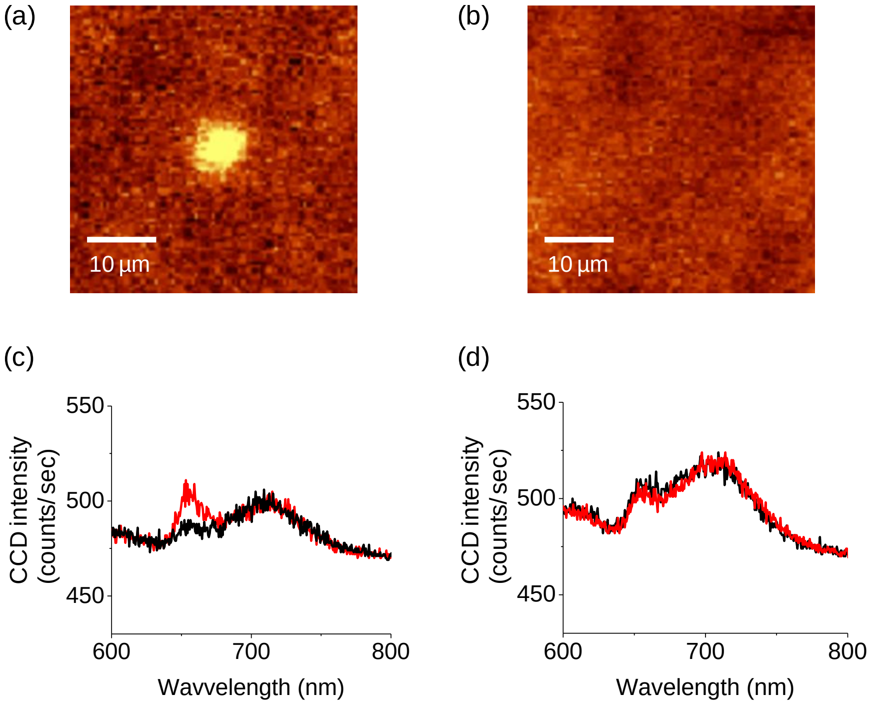

Figure 5.10. (a) The fluorescence image of a TCPP thin film. The contrast is based on the fluorescence intensity between 630 and 680 nm. A 10 x 10 μm^2 in the center was scanned by an AFM tip in contact mode. (b) The fluorescence image of the thin film within the region same as (a) after the sample was immersed in a pH 1 HCl solution for 5 minutes and blow dried with N_2. (c) Fluorescence spectrum of the write-on region (red line) and the back ground (black line). (d) Fluorescence spectrum of the write-on region (red line) and the back ground (black line) after being erased.

To investigate how the humidity affects the fluorescence intensity of the patterns on the porphyrin thin film, fluorescence patterns of four 3x3 μm^2 squares were generated by AFM scanning, and the humidity during the scanning was controlled at 60%, 50%, 40% and 30% by the system chamber. The scanning rate (1.2 μm /sec) and the resolution (128x128 points) of the scanning to produce the squares were the same, and the spacings between the centers of the squares were all 10 μm . Figure 5.11a and b show the 2-D and 3-D fluorescence images of the porphyrin thin film after the AFM scanning. The fluorescence patterns created by the tip-wetting can be clearly seen in the images. The fluorescence intensity of the pattern increased gradually as the humidity during the wetting was increased. Figure 5.11c and d are the fluorescence spectra and the deconvoluted fluorescence spectra collected in the centers of the squares, respectively. Interestingly, the fluorescence intensity at 654 nm increased linearly with the humidity from 30 to 60% (Figure 5.11e), whereas no clear trend of the decrease in the fluorescence intensity at 714 nm was observed. It is likely that at a higher humidity, a larger volume of water meniscus formed between the AFM tip and the surface, and the contact time between the water and the porphyrin fibers in the same area is longer. This allows more porphyrin diacids to be deprotonated, and hence changed the porphyrin fluorescence more effectively. To confirm whether there is any change in the morphology of the porphyrin thin film, the region includes the fluorescence patterns was scanned by AFM in tapping mode. The resulting topographical image shows no difference in the area where the fluorescence patterns were formed, comparing to the morphology of the background (Figure 5.11f). This indicates the fluorescence change on the thin film was not caused by tip scratching or other mechanical forces.

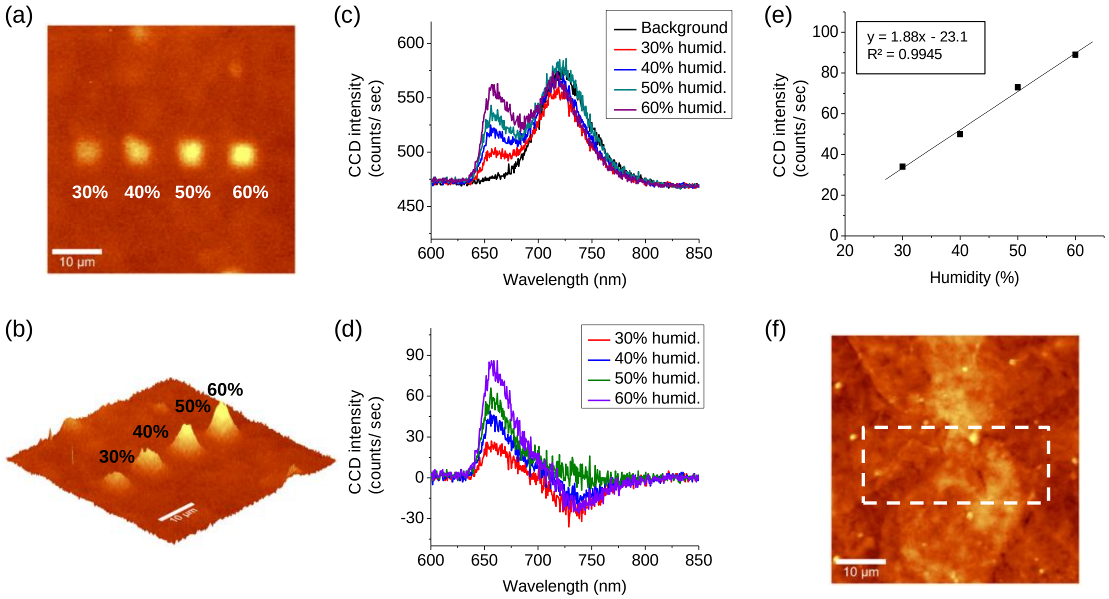

Figure 5.11. (a) and (b) The 2D and 3D fluorescence images of the TCPP thin film, respectively. The contrast of the image is based on the intensity between 630 to 680 nm. Four 3 x 3 μm ^{2} squares with a spacing of 10 μm between each square were generated by AFM scanning in contact mode at different humidity. (c) The fluorescence spectra collected in the center of the squares in the fluorescence images shown in (a) and (b). (d) The deconvoluted fluorescence spectra of (c). The spectra were produced by subtracting the signal of the background from the signals of the samples. (e) The intensity of the porphyrin fluorescence at 654 nm created by AFM tip wetting vs the environmental humidity. The inset shows the equation of the fit curve. (f) AFM topographical image of the porphyrin thin film. The dashed rectangular includes the region of the fluorescence patterns shown in (a) and (b).

The porphyrin fluorescence intensity could also be controlled by changing the scanning rate. Four 3 x 3 μm ^{2} squares were scanned at the rate of 0.6, 1.2, 1.8 and 2.4 μm / second in AFM contact mode at the same humidity (50%). Figure 5.12 (a) and (b) show the 2D and 3D fluorescence images of the region which includes the AFM scanning area. The fluorescence of the neutral porphyrin resulted from the deprotonation of TCPP diacid has a stronger intensity at 654 nm when the AFM scanning rate is slower (Figure 5.12 c). It is likely the contact time between the water meniscus and the porphyrin fiber thin film was longer when the scanning rate was slower. Therefore, the reaction time of the porphyrin diacid deprotonation was longer, producing more neutral porphyrins on the surface. The fluorescence intensity of the neutral porphyrin has a reverse linear relation with the scanning rate, as shown in Figure 5.12d.

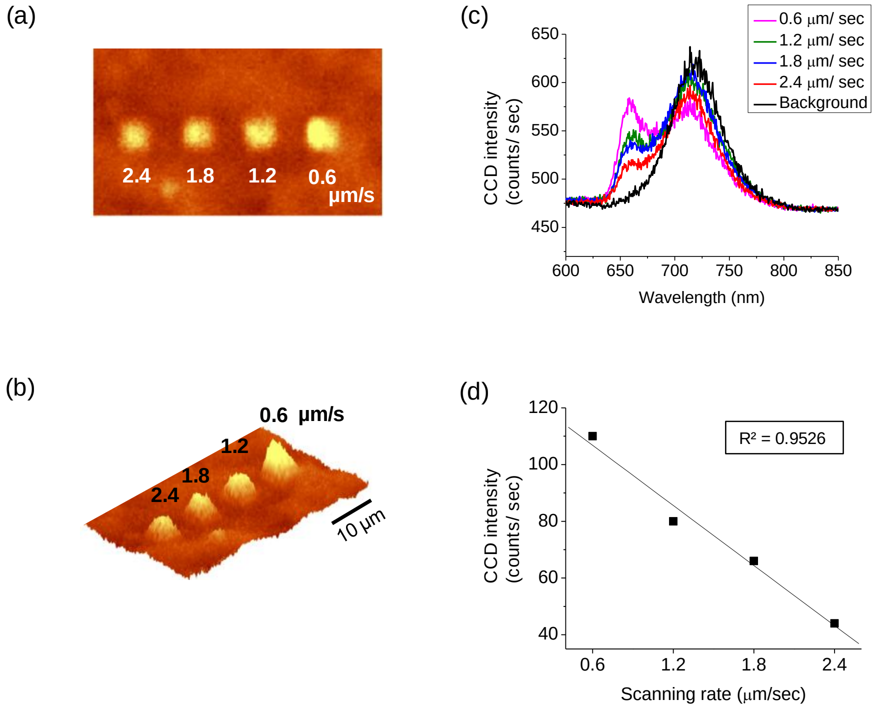

Figure 5.12. (a) and (b) The 2D and 3D fluorescence images of the TCPP thin film, respectively. The contrast of the image is based on the intensity between 630 to 680 nm. Four 3 x 3 μm^2 squares with a spacing of 10 μm between each square were generated by AFM scanning in contact mode at different scanning rate at the same humidity of 50%. (c) The fluorescence spectra collected in the center of the squares in the fluorescence images shown in (a) and (b). (d) The intensity of the porphyrin fluorescence at 654 nm created by AFM tip wetting vs the scanning rate. The inset shows the equation of the fit curve.

5.5. Summary

The optical memory property of the thin film of TCPP nanofibers has been examined. Our results reveal that fluorescence signals can be written on the thin film by AFM scanning. The water meniscus between an AFM tip and the surface of the substrate was utilized to change the the emission of the porphyrin assembly. The changes of the fluorescence on the thin film as the data bits can be “read” by confocal and can be easily erased by immersing the thin film in a pH 1 HCl solution. Moreover, the fluorescence signal increases linearly with the increase of the environmental humidity and the decrease of scanning rate. This reveals that the fluorescence intensity can be systematically control, and the memory information in 3D can be generated.

CHAPTER VI

SIZE CONTROL OF CORROLAZINE NANOPARTICLES ON SURFACE*

6.1. Synopsis

Nanoparticles consisting of corrolazines, which are new types of porphyrinoid compound, were prepared by solvent mixing technique and deposited on self-assembly monolayer (SAM) surface. In order to investigate how the surface interactions affect the size of the nanoparticles, surface energy gradient was prepared by selectively oxidizing the monolayers using UV-ozone and the corrolazine nanoparticles adsorbed on the surface were characterized by AFM in tapping mode. Our results show that the pristine nanoparticles disassembled into smaller nanoparticles when being deposited on the monolayer surface with a larger surface energy. This may have application in catalysis since previous report shows that the particle size of the catalyst based on corrolazine nanoparticles influences the activity of the catalyst in the epoxydation and oxidation reactions.[163]

6.2. Introduction

Corrolazines are a new class of porphyrinoid compounds and were the synthesis of corrolazines was developed by Goldberg et al.[224,225] Unlike porphyrins and phthyal-

---

*Reprinted with permission from "Preparation, Size Control, Surface Deposition, and Catalytic Reactivity of Hydrophobic Corrolazine Nanoparticles in an Aqueous Environment" by Kevin Cho, William D. Kerber, Se Ryeon Lee, Albert Wan, James D. Batteas, and David P. Goldberg, 2010. *Inorganic Chemistry*, 49, 8465-8473, Copyright [2011] by ACS Publications.

ocyanines, which own two replaceable hydrogens within each macrocycle, each corrolazine has three replaceable hydrogens (Figure 6.1). Thus corrolazines and their corrole analogs are able to stabilize metal with high oxidation state, and can be used as catalysts for oxidation reactions or group transfer reactions such as epoxidations,[163,226] and hydroxylations.[227]

Recently the nanoparticles consist of free base corrolazine (H_3Cz) and iron corrolazine (FeCz) were fabricated and the catalytic properties of FeCz in the oxidation of cyclohexene were examined.[163] It was found that in the addition of 5-Cl-1-MeIm, H_2O_2 can be used as the oxidation reagent when FeCz nanoparticles are used as the catalysts, where the molecular species of FeCz exhibit no catalytic activity in the same condition. Moreover, the size of the FeCz nanoparticles was found to affect the product selectivity significantly (Table 6.1). Therefore, it is desirable to control the particle size of corrolazine nanoparticles for the application in catalysis. For conventional heterogeneous catalysts the size and the catalytic properties of metal nanoparticles are usually affected by the interaction between the nanoparticles and the support. This inspires us to study how surface interaction of Cz nanoparticles influence the particle size and the morphology.

Table 6.1 Oxidation of Cyclohexene catalyzed by Fe(III)Cz and Fe(III)Cz nanoparticles. (Reproduced from ref. [163] with the permission of the copyright holders.)

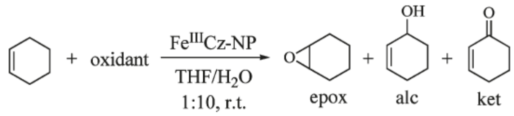

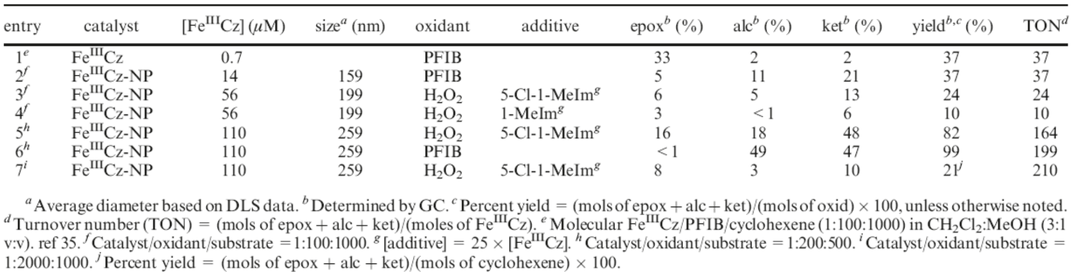

entry	catalyst	[$\mathrm{Fe^{III}}$Cz] (μM)	size[a] (nm)	oxidant	additive	epox[b] (%)	alc[b] (%)	ket[b] (%)	yield[b,c] (%)	TON[d]
1[e]	$\mathrm{Fe^{III}}$Cz	0.7		PFIB		33	2	2	37	37
2[f]	$\mathrm{Fe^{III}}$Cz-NP	14	159	PFIB		5	11	21	37	37
3[f]	$\mathrm{Fe^{III}}$Cz-NP	56	199	H_2O_2	5-Cl-1-MeIm[g]	6	5	13	24	24
4[f]	$\mathrm{Fe^{III}}$Cz-NP	56	199	H_2O_2	1-MeIm[g]	3	< 1	6	10	10
5[h]	$\mathrm{Fe^{III}}$Cz-NP	110	259	H_2O_2	5-Cl-1-MeIm[g]	16	18	48	82	164
6[h]	$\mathrm{Fe^{III}}$Cz-NP	110	259	PFIB		< 1	49	47	99	199
7[i]	$\mathrm{Fe^{III}}$Cz-NP	110	259	H_2O_2	5-Cl-1-MeIm[g]	8	3	10	21[j]	210

[a] Average diameter based on DLS data. [b] Determined by GC. [c] Percent yield = (mols of epox + alc + ket)/(mols of oxid) × 100, unless otherwise noted. [d] Turnover number (TON) = (mols of epox + alc + ket)/(moles of $\mathrm{Fe^{III}}$Cz). [e] Molecular $\mathrm{Fe^{III}}$Cz/PFIB/cyclohexene (1:100:1000) in CH_2Cl_2:MeOH (3:1 v:v). ref 35. [f] Catalyst/oxidant/substrate = 1:100:1000. [g] [additive] = 25 × [$\mathrm{Fe^{III}}$Cz]. [h] Catalyst/oxidant/substrate = 1:200:500. [i] Catalyst/oxidant/substrate = 1:2000:1000. [j] Percent yield = (mols of epox + alc + ket)/(mols of cyclohexene) × 100.

Self-assembly monolayer (SAM) is a layer of amphiphilic molecules adsorbed on the surface through the chemical reaction or chemisorptions of their hydrophilic head groups on the surface. In the adsorption process, the molecules initially lie down and form amorphous islands on the surface. After a period time, the number of molecules saturated and the molecules form close-packed crystalline or semicrystalline structure on the surface. Typical examples of SAMs include alkanethiol monolayer on gold surface and alkanesilane monolayer on silicon surface. The surface characteristic of the SAM surface is mostly determined by the tail groups which are far away from the surface. Therefore, further functionalizing the molecules can modulate the surface properties such as surface energy and surface wettability. For example, the surface modified with alkanesilane monolayer which has methyl groups as the tail groups is hydrophobic, however, after being oxidized through UV-ozone to form carboxylic acid groups as the tail groups, the surface becomes hydrophilic.[223]

The surface energy of a substrate can be determined by measuring its water contact angle according to Young-Dupree equation:[228]

$$W = \gamma(1+\cos\theta)$$

where W is the adhesion energy, γ is the surface tension between air and the liquid and θ is the contact angle.

In this study, corrolazine nanoparticles were deposited on a surface energy gradient and the correlation between the surface energy of the substrate and the particle size was investigated. A surface energy gradient was prepared by selective oxidized an 18-carbon chain silane monolayer on the Si <100> surface. The surface energies at different regions on the same platform were modulated by controlling the oxidation time and determined by the contact angle measurement. The particle size was measured by using AFM in tapping mode. The pristine corrolazine nanoparticles were characterized by dynamic light scattering and high resolution TEM for comparison. In brief, our results show that the nanoparticles disassembled into smaller nanoparticles with narrower size distribution on higher surface energy region.

6.3. Experimental Detail

Preparation of Cz nanoparticles: The Cz nanoparticles was prepared by our collaborator, Goldberg's group. In a typical preparation, 50 μL of a stock solution of corrolazine in THF (1.6 mM) was transferred to a 20 mL vial and diluted with 450 μL of THF to give a final concentration of 0.16 mM of corrolazine. To this solution was added TEG-Me (50 μL), and this mixture was stirred slowly for 5 min to ensure homogeneity.

While stirring at the same rate, Milli-Q H_2O (5.0 mL) was added slowly dropwise (1-2 min for complete addition) giving a final solution composed of H_2O/THF (10:1) (Figure 6.1). Care must be taken to keep the stirring rate of the mixture slow and constant throughout the addition of H_2O to prevent precipitation of the corrolazine. After the addition of H_2O is complete, it is important to stir the nascent nanoparticles for an additional 1-5 min until the solution is completely homogeneous. The final nanoparticle solution appears translucent with no precipitates.

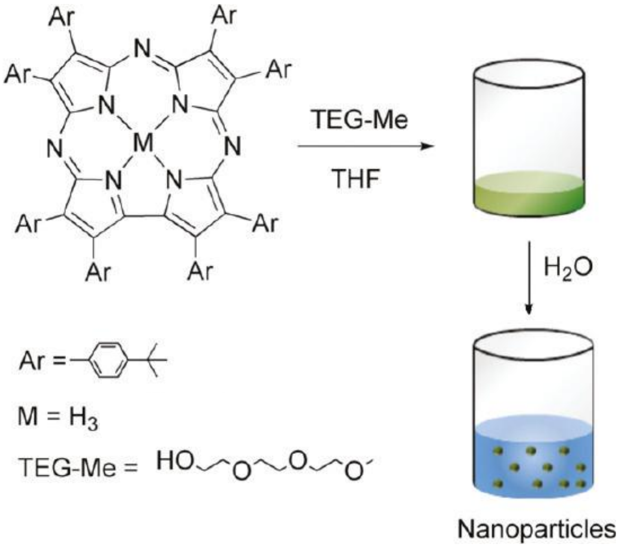

Figure 6.1. Schematic diagram of preparing Cz nanoparticles. (Reproduced from ref. [163] with the permission of the copyright holders.)

Preparation of SAMs with surface energy gradient: A 10 mm × 20 mm piece of silicon wafer was first oxidized in a mixture of 12 mL H_2O, 3 mL of 30% H_2O_2 and 3 mL concentrated NH_4OH at 85 ^{o}C for 40 min, and then cleaned with copious amounts of water and dried under a jet of streaming nitrogen. This process also generated a layer of hydroxyl groups on the Si wafer. The cleaned and oxidized Si wafer was then immersed in a 0.25 mM of octadecyltrichlorosilane (OTS)/hexanes solution with sonification at room temperature for 2 h. The sample was then washed in THF, water, ethanol, and dried with N_2 and then characterized by infrared spectroscopy (Thermo Nicolet 6700 FTIR) and static water contact angle measurements. The infrared spectrum showed the appearance of C-H symmetric stretching frequency at 2852 cm^{-1} and C-H asymmetric stretching frequency at 2918 cm^{-1}. The OTS surface exhibited a static water contact angle of ∼110°. The C-H asymmetric stretch of 2918 cm^{-1} is indicative of a well ordered OTS monolayer, which is consistent with the large water contact angle. A gradient in surface energy was prepared on the Si wafer by selectively oxidizing the OTS monolayer to various degrees using an ultraviolet/ozone gradient instrument. This home-built instrument consists of a UV-lamp with emission wavelengths of 254 and 285 nm, which was used to produce ozone and oxidize the surfaces. The OTS coated Si wafer is rastered underneath the UVlamp at a distance of about 1 mm with a computer controlled micropositioning stage (Zaber Technologies Inc., Canada). The wafer was divided evenly into four 5 × 10 mm^2 regions using a diamond cut to mark their boundaries. The sample was placed on the scan stage and moved under the UV-lamp at a constant rate of 0.032 mm/s and each region of the OTS/Si wafer was exposed to the UV light 10 sweeps, 6 sweeps, 2 sweep, with the last region receiving no exposure to produce the surface energy gradient with static water contact angle of 40°, 60°, 75°, and 110°, respectively for each region. All 4 regions were scanned using AFM tapping mode to confirm there were no cluster-like species on the surface before depositing Cz nanoparticles.

Deposition and Characterization of Corrolazine Nanoparticles: Typically Cz nanoparticles were deposited on the surface energy gradient by drop-casting 5 μL of the diluted (1600:1) Cz nanoparticles suspension on each region which were then air-dried in a covered Petri dish. AFM images of the deposited nanoparticles were collected on the central regions of the dried droplet areas. For AFM measurements (AFM, Alpha300 S, WiTec Germany) ultrasharp silicon AFM tips (VISTA probes, NanoScience Instruments, Phoenix, Az) with nominal tip radii of <10 nm, a lever frequency of ~300 kHz, and a force constant of ~40 N/m were used.

6.4. Results and Discussion

The size of the Cz nanoparticles in solution was measured by dynamic light scattering (DLS). Figure 6.2a shows the size distribution of Cz nanoparticles within the solution. The data are displayed as histograms showing the percentage of particles versus hydrodynamic diameter. The average diameter of the nanoparticles was 181 nm with a polydispersity index (PDI) of 0.096.

Further characterization of the Cz nanoparticles was done by TEM. Figure 6.2b shows the TEM image of the Cz nanoparticles dispersed on a Cu-grid. The nanoparticles exhibit spherical morphology. The diameters of the nanoparticles are 100-300 nm, which agree well with the DLS results. These data help confirm the spherical nature of the particles in solution, which is important for the DLS analysis because it relies upon the assumption that the NPs behave as hard spheres in solution.

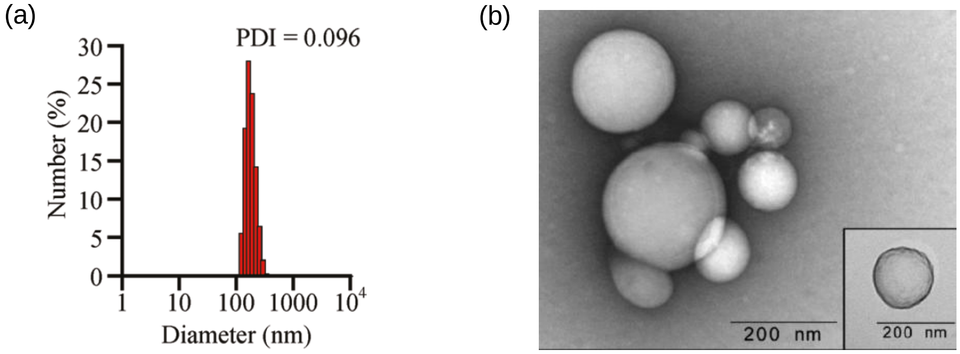

Figure 6.2. (a) The DLS histogram of the diameters of Cz nanoparticles in solution. (b) The TEM image of Cz nanoparticles on a Cu-grid. (Reproduced from ref. [163] with the permission of the copyright holders.)

In order to examine the influence of the surface interaction on the morphology of Cz nanoparticles, suspensions were deposited on a surface energy gradient prepared by oxidizing an OTS-Si SAM surface with UV light, and then characterized by AFM imaging in tapping mode. Oxidizing OTS with UV light produces carboxyl species,[223] thus lowering the water contact angle of the surface and increasing the surface hydrophilicity. Figure 6.3 and 6.4 show the IR spectrum of OTS monolayer on Si and water contact angle on the monolayer, respectively, before and after treated with UV-ozone. The spectrum shows the appearance of C-H symmetric stretching frequency at 2852 cm^{-1} and C-H asymmetric stretching frequency at 2918 cm^{-1} (Figure 6.3). The C-H asymmetric stretch of 2918 cm^{-1} is indicative of a well ordered OTS monolayer. The OTS surface exhibited a static water contact angle of ∼110^{o} (Figure 6.4a). OTS surfaces with contact angle of 75°, 60° and 40° were obtained by illuminating the monolayers with UV light 2 sweeps, 6 sweeps and 10 sweeps, respectively (Figure 6.4 b-d). An illustration depicting the process of oxidizing the OTS-Si SAM surface and the disassembly of the Cz nanoparticles onto the treated surface can be seen in Figure 6.5.

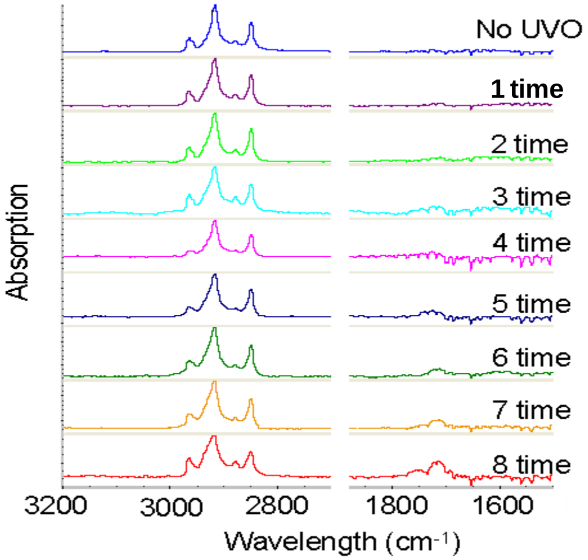

Figure 6.3. IR spectrum of OTS-Si before and after being illuminated with UV light various sweeps.

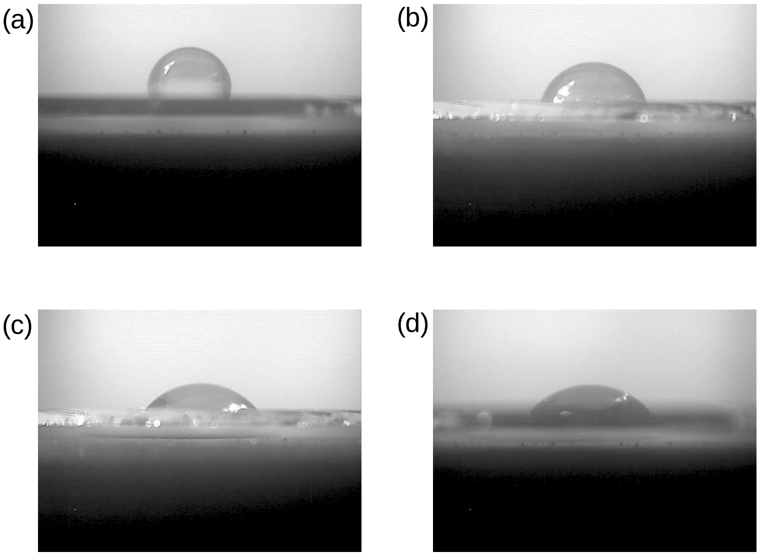

Figure 6.4. Water contact angle (CA) on OTS-Si (a) before exposing to UV light (CA= 110^o), (b) after sweeping by UV light for 2 times (CA= 75^o), (c) after sweeping by UV light for 6 times (CA= 60^o), (d) after sweeping by UV light for 10 times (CA= 40^o).

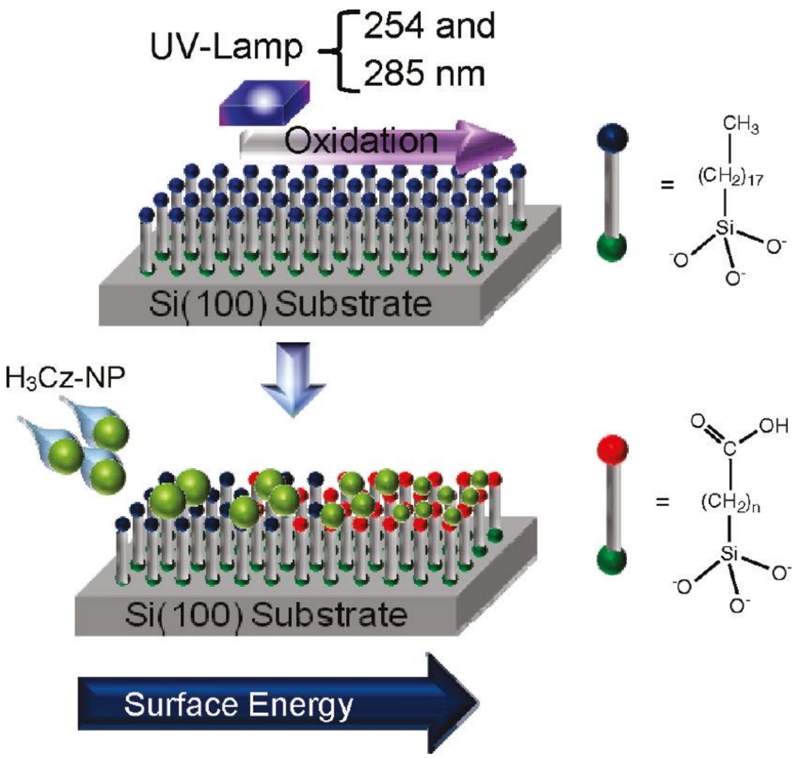

Figure 6.5. Illustration depicting the treatment of the OTS/Si SAMsurface by sweeping under a UV-lamp (top) and the adsorption and disassembly of Cz nanoparticles on to regions of the surface with varying degrees of oxidation of the SAM (bottom). (Reproduced from ref. [163] with the permission of the copyright holders.)

Figure 6.6 shows the AFM images and the size distribution of Cz nanoparticles on OTS-Si substrate with various contact angles. On the clean OTS surface with contact angle 110° (no UV light exposure), the average size of the nanoparticles is 227 ± 65 nm (Figure 6.6a and c). This is similar to the size obtained by DLS and TEM. Therefore, it is likely the nanoparticles maintained their solution phase morphologies on the hydrophobic OTS modified Si surface. On the surface with contact angle 75°, the average size of the nanoparticles decreases to 42 ± 27 nm (Figure 6.6b and d). The particle size decreases to 11 ± 3 nm and 13 ± 4 on the surfaces with contact angle of 60^o (Figure 6.7a and c) and 40^o (Figure 6.7b and d), respectively. Occasionally, on the surfaces with contact angle of ~60^o, collapse of the large nanoparticles was observed in some regions (Figure 6.8). These data indicate that interfaces with high surface energies favor the disassembly of Cz nanoparticles, producing small nanoparticles of about 10-15 nm with a relatively uniform size distribution. Figure 6.9 shows how the average particle size varies with the contact angle of the modified OTS-Si surface. A similar breakdown process has been reported for porphyrin ONPs.[33,38]

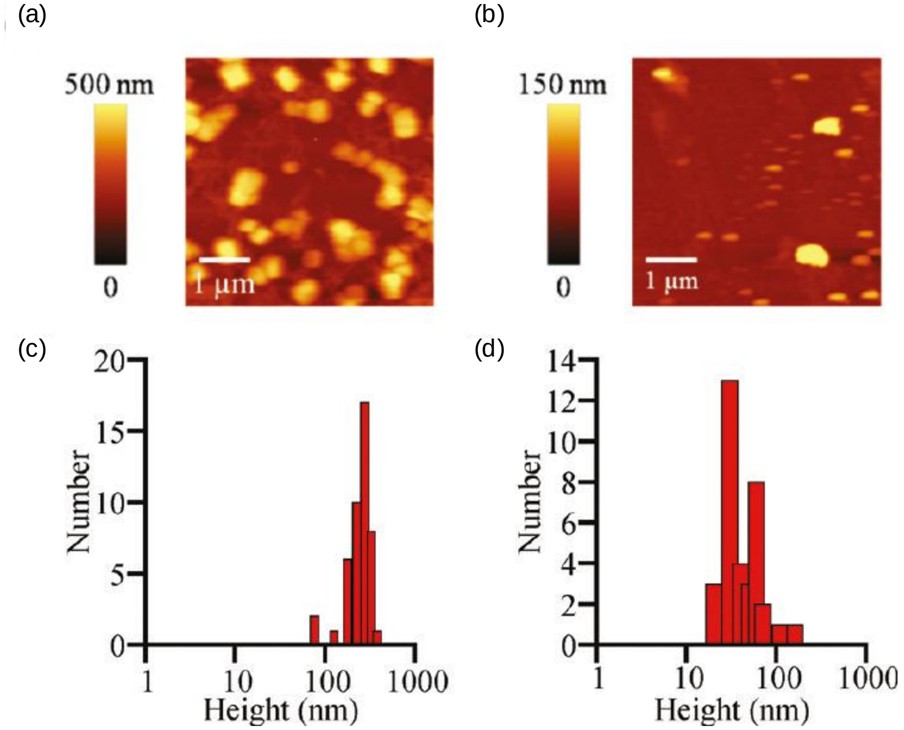

Figure 6.6. Topographic AFMimages and size distribution of Cz nanoparticles adsorbed on to UV/ozone-treated OTS-Si substrate. (a) and (b) are the AFM images of Cz nanoparticles adsorbed on OTS-Si with contact angle 110^o and 75^o, respectively. (c) and (d) are the size distribution of Cz nanoparticles adsorbed on OTS-Si with contact angle 110^o, 75^o, respectively.

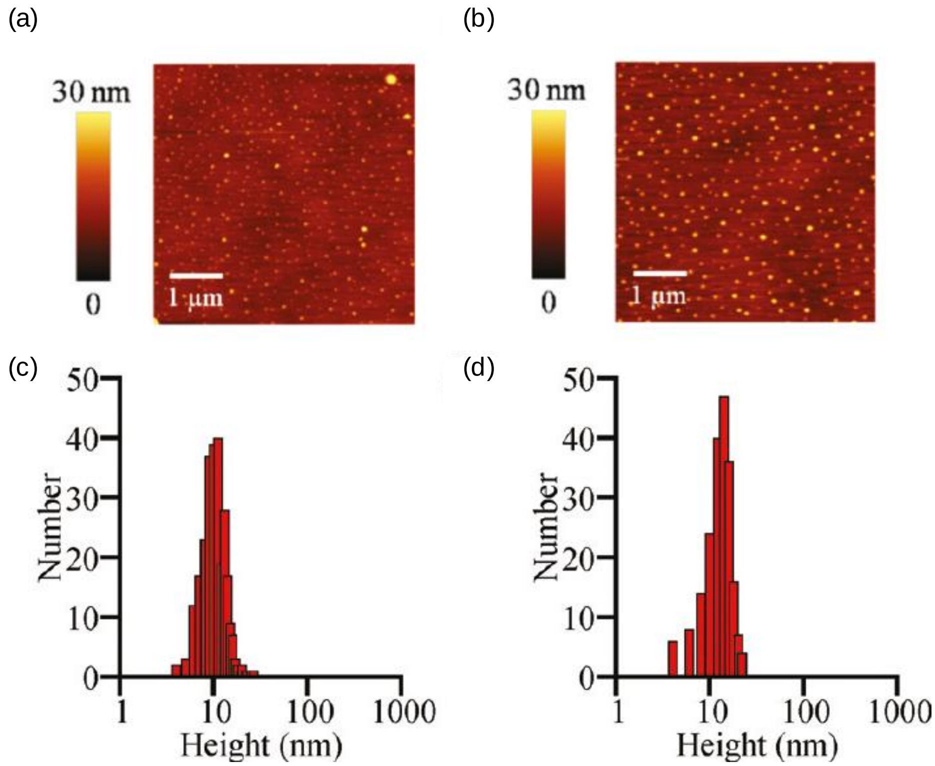

Figure 6.7. Topographic AFMimages and size distribution of Cz nanoparticles adsorbed on to UV/ozone-treated OTS-Si substrate. (a) and (b) are the AFM images of Cz nanoparticles adsorbed on OTS-Si with contact angle 60° and 40°, respectively. (c) and (d) are the size distribution of Cz nanoparticles adsorbed on OTS-Si with contact angle 60°, 40°, respectively.

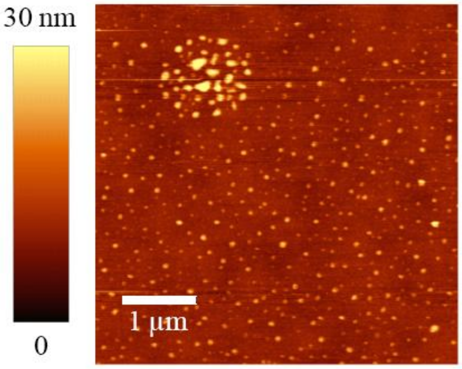

Figure 6.8. AFM image of large Cz nanoparticles disassembled into small particles on UV/ozone-treated OTS-Si substrate with contact angle 60°.

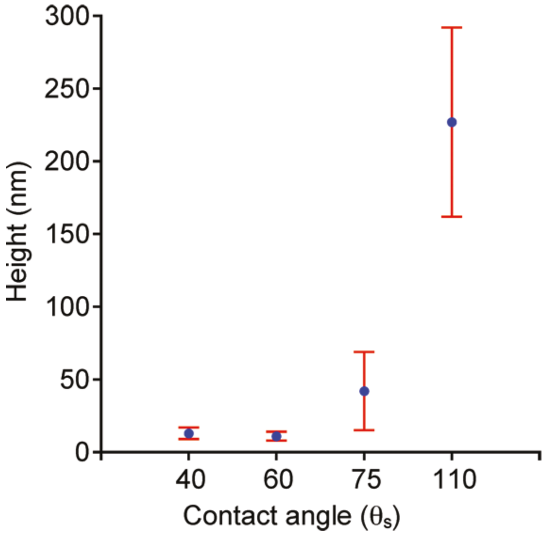

Figure 6.9. Average height of Cz nanoparticles versus the contact angle of the OTS modified Si surface.With increasing surface energy, the nanoparticles size decreases down to about 10 nm. (Reproduced from ref. [163] with the permission of the copyright holders.)

6.5. Summary

Water-soluble, corrolazine nanoparticles from highly hydrophobic corrolazines have been prepared by solvent mixing technique, and the influence of surface interaction on their size distribution on a surface energy gradient was investigated. The nanoparticles were found to disassemble into smaller nanoparticles on the surface with high surface energy. Therefore, the size of the corrolazine nanoparticles can be controlled by depositing onto OTS-modified silicon surfaces of controlled surface energies. These results are consistent with the presumed dynamic nature of the organic nanoparticles, which are assembled by relatively weak intermolecular forces. Their dynamic nature is advantageous in that different particle sizes can be accessed easily on the OTS modified Si surface and may have applications in catalysis or sensors.

CHAPTER VII

MORPHOLOGY STUDY AND WETTABILITY CONTROL OF POLYMER NANOCOMPOSITES*

7.1. Synopsis

Wettability of a surface can be influence by the hydrophobicity or hydrophilicity of the molecules functionalized on the surface and the surface roughness.[229-231] In this study polymer nanocomposites with controllable wettability were fabricated by layer-by-layer assembly, in which multiple carbon nanotubes or silica nanoparticles were added to increase the surface roughness of the nanocomposites. The morphology of the surface and the surface roughness of the nanocomposites during and after the layer-by-layer assembly were characterized by AFM in tapping mode. The distribution of the carbon nanotubes or silica nanoparticles within the nanocomposites was analyzed using confocal. It was found that increasing the surface roughness enhanced the hydrophobicity of the nanocomposite and eventually superhydrophobic surface was obtained. Moreover, surfaces with Hofmeister-like anion and cation-responsive wettability can be prepared by using covalent layer-by-layer assembly of PNIPAM-c-

---

*Reprinted with permission from "Superhydrophobic Surfaces Formed Using "Layer-by-Layer Self-Assembly with Aminated Multiwall Carbon Nanotubes" by Kang-Shyang Liao, Albert Wan, James D. Batteas, and David E. Bergbreiter, 2008. *Langmuir*, 24, 4245-4553, from "Superhydrophobic Surfaces Formed Using "Designing Surfaces with Wettability That Varies in Response to Solute Identity and Concentration" by Kang-Shyang Liao, Hui Fu, Albert Wan, James D. Batteas, and David E. Bergbreiter, 2009. *Langmuir*, 25, 26-28, and from "Parallel Effects of Cations on PNIPAM Graft Wettability and PNIPAM Solubility" by Hui Fu, Xiaoting Hong, Albert Wan, James D. Batteas, and David E. Bergbreiter, 2010. *ACS Applied Materials & Interfaces*, 2, 452-458,Copyright [2011] by ACS Publications.

PNASI with aminated silica nanoparticles. The changes in wettability and surface roughness were in response to solute ion identity and concentration.

7.2. Introduction

Wettability is a fundamental property of a solid surface and has drawn a lot of interest because of its usefulness in daily life, industry and agriculture. Biomimetic research demonstrates many phenomena related to wettability in nature, such as self-cleaning ability of lotus leaf, anisotropic dewetting property of rice leaf, and superhydrophobic force of water strider's legs. Based on the fundamental theory and inspired by nature, different approaches have been utilized to construct ultra rough surface with superhydrophobic properties[1-12]. Typically, superhydrophobic surface can be obtained by modifying a rough surface with molecules which exhibit low surface energy or roughening a surface which possesses low surface energy. Moreover, wettability-responsive surfaces (smart surfaces) have been developed in recent years[13-26]. The wettability of the surface can be tuned from superhydrophobic [water contact angle (CA) > 150^o] to superhydrophilic (CA ~ 0) or in the reverse way by inducing different stimuli, such as irradiation, electro current, solvent or pH. Special wettability on surfaces is expected to have application of microfluidics technology and usefulness in industry.

The wettability of a surface is generally defined by the contact angle (θ) of a water droplet on the surface. The contact angle results from the balance of the interfacial energies between solid-vapor, solid-liquid and liquid vapor, according to Young's equation,

$$\cos(\theta) = (\gamma_{SV} - \gamma_{SL}) / \gamma_{LV}$$

where γ_{SV}, γ_{SL} and γ_{LV} are the interfacial energy between solid-vapor, solid-liquid and liquid vapor, respectively. Young's equation is only appropriate to the liquid drop on a flat surface.

Both chemical composition and topographical structure of the surface can influence its wettability. The surface energy is determined by the chemical composition of the surface. However, there is certain limitation if surface roughness is not concern. For example, the $–CF_3$- terminated surface was reported to possess the lowest surface energy, but on the flat surface its maxima contact angle could only reach about 120^{o} [27]. It was found that when increasing the surface roughness, contact angle larger than 150^{o} could be obtained on the $–CF_3$- terminated surface. The influence of the surface topographical structure was explained by two models. One is Wenzel's model[28] (Figure 7.1a), which the liquid is believed to contact with the whole solid surface and the apparent contact angle θ' is amplified by the solid roughness,

$$\cos \theta' = r \cos \theta$$

where θ is the contact angle on the flat surface. The solid roughness r is defined as the ratio between the true surface area over the apparent one. The other model is Cassie's model[29] (Figure 7.1b), which the liquid is proposed to contact only the top of the asperities of the solid surface and leave the air below. In Cassie's equation,

$$\cos \theta' = f \cos \theta - (1 - f)$$

where f is the fraction of the solid/water interface, while (1 –*f*) is the fraction of the air/water interface. The behaviors of the water droplet in Wenzel's model and Cassie's model have both been observed on a surface with pillar structures in the experiment by Yoshimitsu and coworkers[30]. Later, it was observed by Lafuma and Quéré that irreversible transitions can be induced from Cassie to Wenzel states[31].

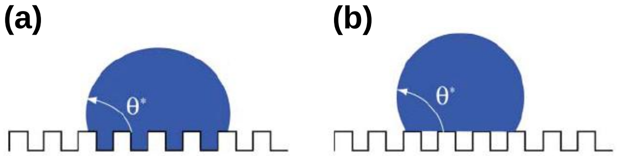

Figure 7.1. Schematic diagram of water droplet on a rough surface. (a) Wenzel model. (b) Cassie model. (Reproduced from the permission of the copyright holders from *Soft Matter* 2005, 1, 55)

A superhydrophobic surface is defined as the surface with water contact angle larger than 150°. The effect of superhydrophobicity is largely utilized in nature, including the self-cleaning of lotus leaf and the water-repelling of water spiders' legs. Assembling artificial superhydrophobic surfaces and controlling the surface wettability may have applications in microfluidic channels and anti-biofouling.

Recently, it has been shown that layer-by-layer self-assembly through electrostatic interaction or covalent bonding show promise for preparing rough surfaces with superhydrophobic properties or smart surfaces. Herein superhydrophobic PE film was obtained by covalent layer-by-layer self-assembly of PEI functionalized MWNTs and Gantrez. The surface roughness of the film was characterized by AFM and the distribution of the MWNTs was analyzed by confocal. On the other hand, PE film with anionic or cationic-responsive wettability was prepared by covalent layer-by-layer self-assembly of PNIPAM-c-PNASI with 10 and 100 nm diameter aminated silica nanoparticles. The surface roughness of the film was measured in air and in solution with various ions at different concentration. The correlation between the surface roughness and the contact angle of the film was investigated.

7.3. Experimental Detail

7.3.1. Preparation of Superhydrophobic Surface

Superhydrophobic PE films were prepared using covalent layer-by-layer self-assembly by our collaborators, Dr. Bergbreiter's group. The detail of the assembly procedure was reported elsewhere.[232]

7.3.2. Atomic Force Microscopy Studies of Superhydrophobic PE Film

The surface topography and roughness of the samples were characterized by atomic force microscopy in the tapping mode using a commercial atomic force microscope (Alpha300 S, WITec, Germany) which combines a confocal (Raman and fluorescence) microscope (CM) and an atomic force microscope. Ultrasharp silicon atomic force microscopy (AFM) tips (VISTA probes, NanoScience Instruments, Phoenix, AZ) with nominal tip radii of <10 nm, a lever resonance frequency of ~300 kHz, and a force constant of ~40 N/m were utilized. To determine the representative roughness of the surface, ten 1 µm × 1 µm AFM topographic images were taken at random positions on each sample and the value of the root-mean-square (rms) roughness was obtained.

7.3.3. Modification of AFM Tips

To decrease the adhesion between the AFM tip and the polymer surface, the tip was modified with octadecyltrichlorosilane (OTS) prior to use. To coat the tips, they were immersed in a $NH_4OH/H_2O_2/H_2O$ solution (vol. ratio: 1:1:4) for 1 minute, rinsed with water, acetone and dried with N_2 flow. The tip was then immersed in a solution of 1 Om OTS/ 10 ml hexane for 30 seconds, rinsed with hexane, ethanol, water, acetone, and dried with N_2 flow.

7.3.4. Confocal Raman Imaging of Superhydrophobic PE Film

Raman spectra and images were acquired with the same instrument described above, including a piezoelectric scan table, a microscope objective (100×, NA = 0.9 and 20×, NA = 0.45, Nikon), and a Peltier cooled charge-coupled device (CCD) detector (Andor). An air-cooled argon-ion laser at 488 nm was focused onto the samples. The Raman spectra were obtained at 4 cm^{-1} resolution with a 0.2 s integration time. Confocal Raman images were acquired based on the integrated G band and D band intensities in the frequency range between 1050 and 1700 cm^{-1}. The laser intensity was kept as low as possible during the experiment to minimize thermal damage caused by the laser.

7.3.5. Preparation of PE Film with Ion-Responsive Wettability

The PE film with ion-responsive wettability was prepared using covalent layer-by-layer self-assembly by Dr. Bergbreiter's group. The detail of the assembly procedure was reported elsewhere.[233]

7.4. Results and Discussion

7.4.1. Superhydrophobic PE Film

The process of covalent step-by-step assembly of MWNT-NH-PEI and Gantrez used is shown in Figure 7.2. This assembly process on films yielded visibly uniform coverage with films that become darker after each bilayer deposition for the first five bilayers. The nanocomposite exhibit superhydrophobic character with an advancing water contact angle of ~165° and a water sliding angle less than 5°.

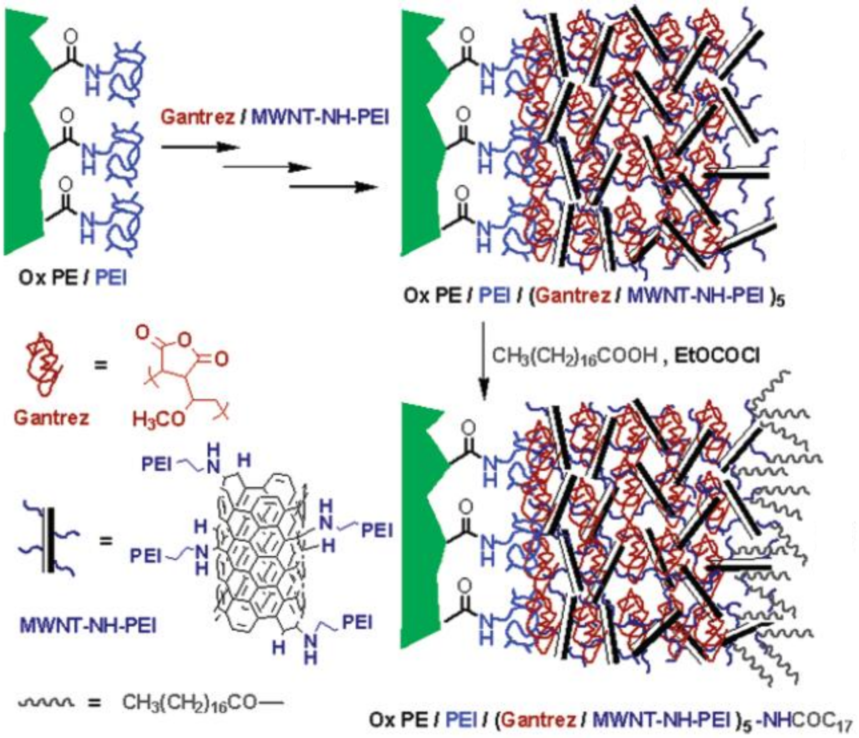

Figure 7.2. Procedure of covalent layer-by-layer self-assembly of Gantrez/MWNT-NH-PEI on PEI grafted oxidized PE film and further acrylation with a mixed anhydride prepared from chloroformate and octadecanoic aicd. (Reproduced from ref. [232] with the permission of the copyright holders.)

To better understand the character of these nanocomposite grafts, the surface morphology of the starting films and of both the ionically and covalently assembled layer-by-layer grafts were examined by AFM (Figure 7.3). The initial oxidized PE surface shows the typical fibrillar structure expected for such films (Figure 7.3a). Upon sequential layer-by-layer self-assembly, large clusters of accumulated materials are found on the surface, which generally increasing roughness up to the fifth bilayer. The first bilayer sample exhibited a relatively large sliding angle of >90°, indicating significant adhesion between the surface and water. AFM images show that this is likely due to incomplete coverage by the first bilayer, as large regions of oxidized PE remain exposed on the surface (Figure 7.3b) and the carboxylic acid groups of oxidized PE can form hydrogen bonds with water. However, after depositing more than two bilayers, the fiber-like oxidized PE was buried (Figure 7.3c-f), and the sliding angle of these samples decreased to only ~5°-10°. Topographic AFM images showed that the oxidized PE film had a root-mean-square (rms) roughness of ~58 nm. After five covalent layer-by-layer self-assembly steps, the rms roughness of the (Gantrez/MWNT-NH-PEI)$_5$-NHCOC$_{17}$ PE film increased greatly to ~306 nm. A controlled sample, the (Gantrez/PEI)$_5$- NHCOC$_{17}$ PE film, which was prepared using the same process instead of substituting PEI for MWNTs, had a contact angle of 100° and a rms roughness of only ~97 nm, indicating that the MWNTs play an important role for assembling an ultrarough surface.

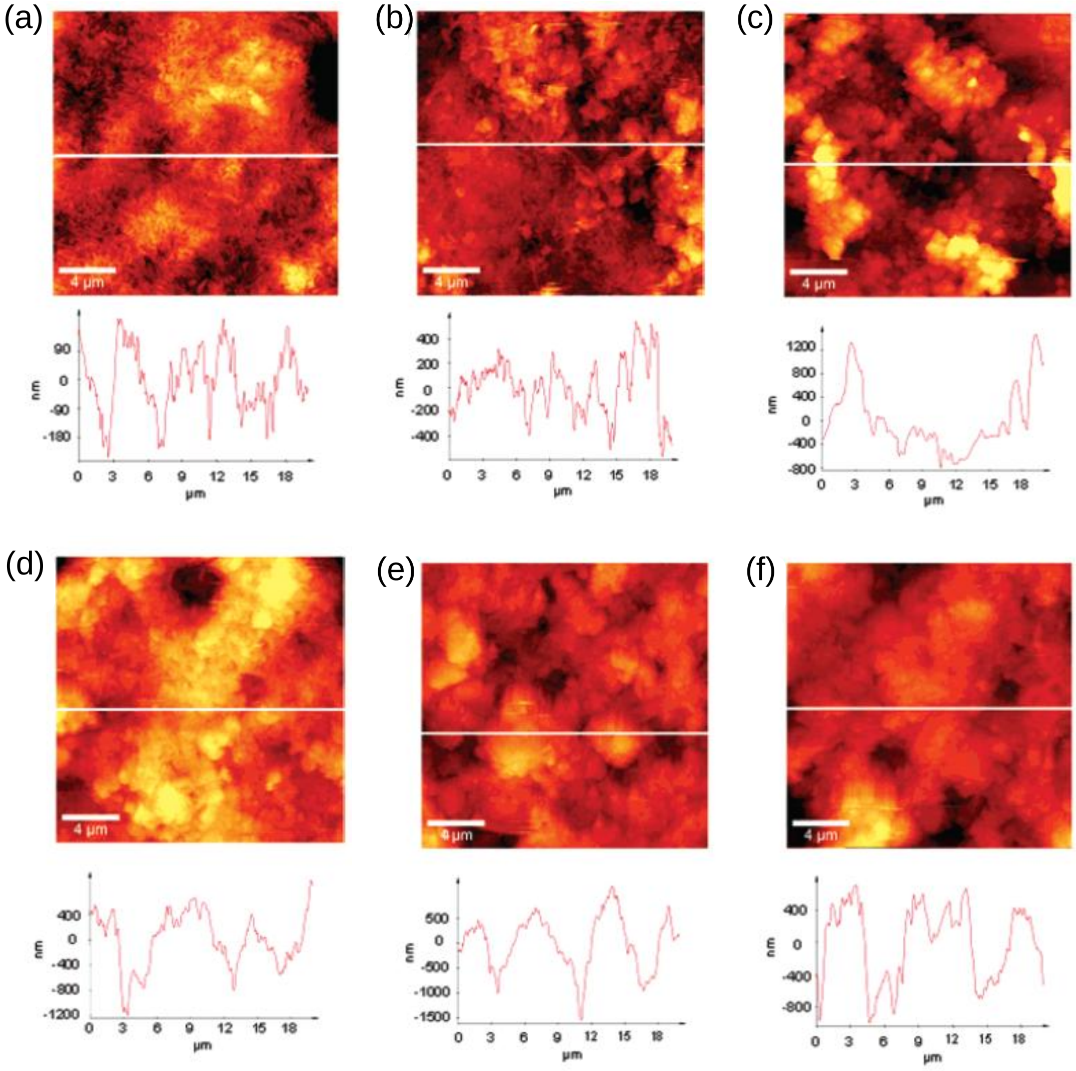

Figure 7.3. Series of tapping mode AFM topographic images of covalent layer-by-layer self-assembled (Gantrez/MWNT-NH-PEI)*x*- NHCOC$_{17}$ PE films with different numbers of bilayers (*x*) 1-5): (a) oxidized PE film, (b) 1 bilayer, (c) 2 bilayers, (d) 3 bilayers, (e) 4 bilayers, and (f) 5 bilayers. (Reproduced from ref. [232] with the permission of the copyright holders.)

Spatial variations in the MWNT coverage were examined by confocal Raman microspectroscopy. The Raman spectrum of the (Gantrez/MWNT-NH-PEI)$_5$-NHCOC$_{17}$ PE film showed a D band and G band of MWNTs at 1354 and 1584cm^{-1}, respectively, and also a 2D band at 2710 cm^{-1} (Figure 7.4c). Both horizontal and vertical Raman mapping based on the intensities of the G band and D band indicated that MWNTs were distributed throughout the sample (Figure 7.4a and b). High-resolution Raman images taken with a 100×, 0.9 NA objective (data not shown) were convoluted with the significant height variations over the sample of nearly 800 nm, which moves materials in and out of the focal plane of the image. This was confirmed by images taken with a 20×, 0.45 NA objective which has a larger focal volume and shows that the tubes are distributed fairly uniformly throughout the samples.

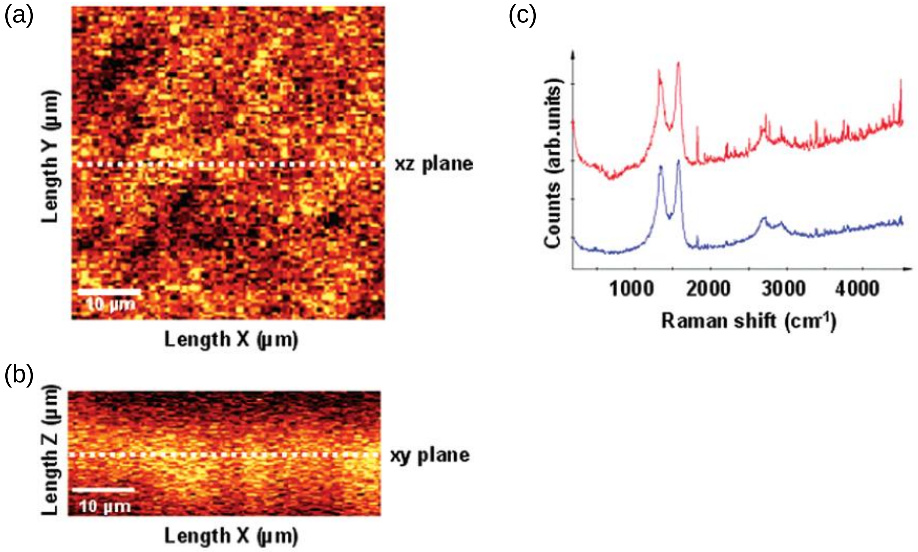

Figure 7.4. Raman spectrum of the (Gantrez/MWNT-NH-PEI)$_5$- NHCOC$_{17}$ PE film and relative Raman images in the spectrum range of 1050 to 1700 cm^{-1}: (a) Raman image in the *X*-*Y* plane, (b) Raman image in the *X*-*Z* plane, and (c) integrated average Raman spectrum obtained from the image (red) as compared to that of a pure MWNT sample (blue). (Adapted from ref 235.)

7.4.2. PE Film with Ion-Responsive Wettability

The synthesis of the solute responsive nanocomposite grafts involved utilizing PNASI (Mw = 30,000), PNIPAM-c-PNASI (Mw = 30,000) as electrophilic reagents, and PEI (Mn = 10000), aminated 10 and 100 nm fused silica nanoparticles as nucleophilic reagents. Scheme 7.1 illustrates the entire process of the covalent layer-by-layer assembly on a Si wafer. The Si wafer was cleaned by immersing the wafer in piranha solution [H_2O_2/H_2SO_4 (volume ratio 3:7)] at 60^{o}C for 30 minutes and then cleaned with deionized water prior to use. In the first step of the assembly process, the Si wafer was modified with 3-aminopropyltriethoxysilane (APTES) and then treated with PNASI. This allowed the amine groups of APTES to react with the NASI groups and formed amide bonds. The unreacted NASI groups on the surface were then reacted with PEI followed by being treated with excess of *i*-$PrNH_2$ to quench the remaining unreacted NASI (Step A in Scheme 7.1). The AFM image shows small polymer clusters well dispersed on the surface (Figure 7.5a). The surface roughness, which was obtained by averaging the room-mean-square roughness of five 2.5 μm × 2.5 μm regions, was measured to be 7 ± 3 nm. Step A produced an amine-rich surface and was repeated one time. The AFM image shows that repeating step A not only increased the coverage of the small polymer clusters, but also formed large polymer aggregates on the surface (Figure 7.5b), which exhibited surface roughness of 6 ± 2 nm, which was similar to the first time through step A. Although the aggregation of the polymer may increase the surface roughness, it is possible that more polymers filled in the defects of the film and flattened the surface.

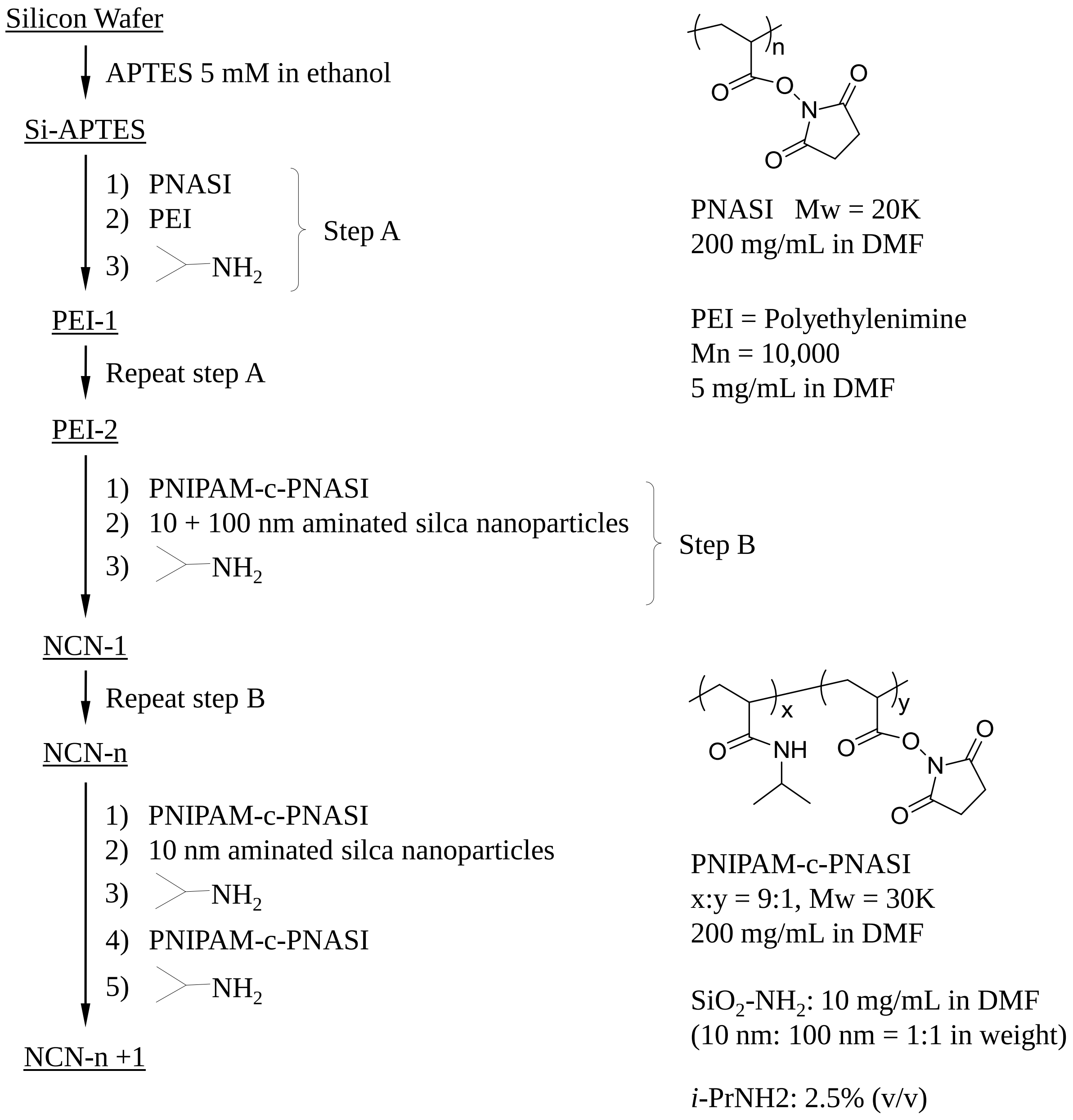

Silicon Wafer

APTES 5 mM in ethanol

Si-APTES

1) PNASI
2) PEI
3) NH$_2$

Step A

PEI-1

Repeat step A

PEI-2

1) PNIPAM-c-PNASI
2) 10 + 100 nm aminated silca nanoparticles
3) NH$_2$

Step B

NCN-1

Repeat step B

NCN-n

1) PNIPAM-c-PNASI
2) 10 nm aminated silca nanoparticles
3) NH$_2$
4) PNIPAM-c-PNASI
5) NH$_2$

NCN-n +1

PNASI Mw = 20K
200 mg/mL in DMF

PEI = Polyethylenimine
Mn = 10,000
5 mg/mL in DMF

PNIPAM-c-PNASI
x:y = 9:1, Mw = 30K
200 mg/mL in DMF

SiO_2-NH_2: 10 mg/mL in DMF
(10 nm: 100 nm = 1:1 in weight)

i-PrNH2: 2.5% (v/v)

Scheme 7.1. Flow chart of synthesis of anion induced wettability responsive surface by covalent layer-by-layer assembly.

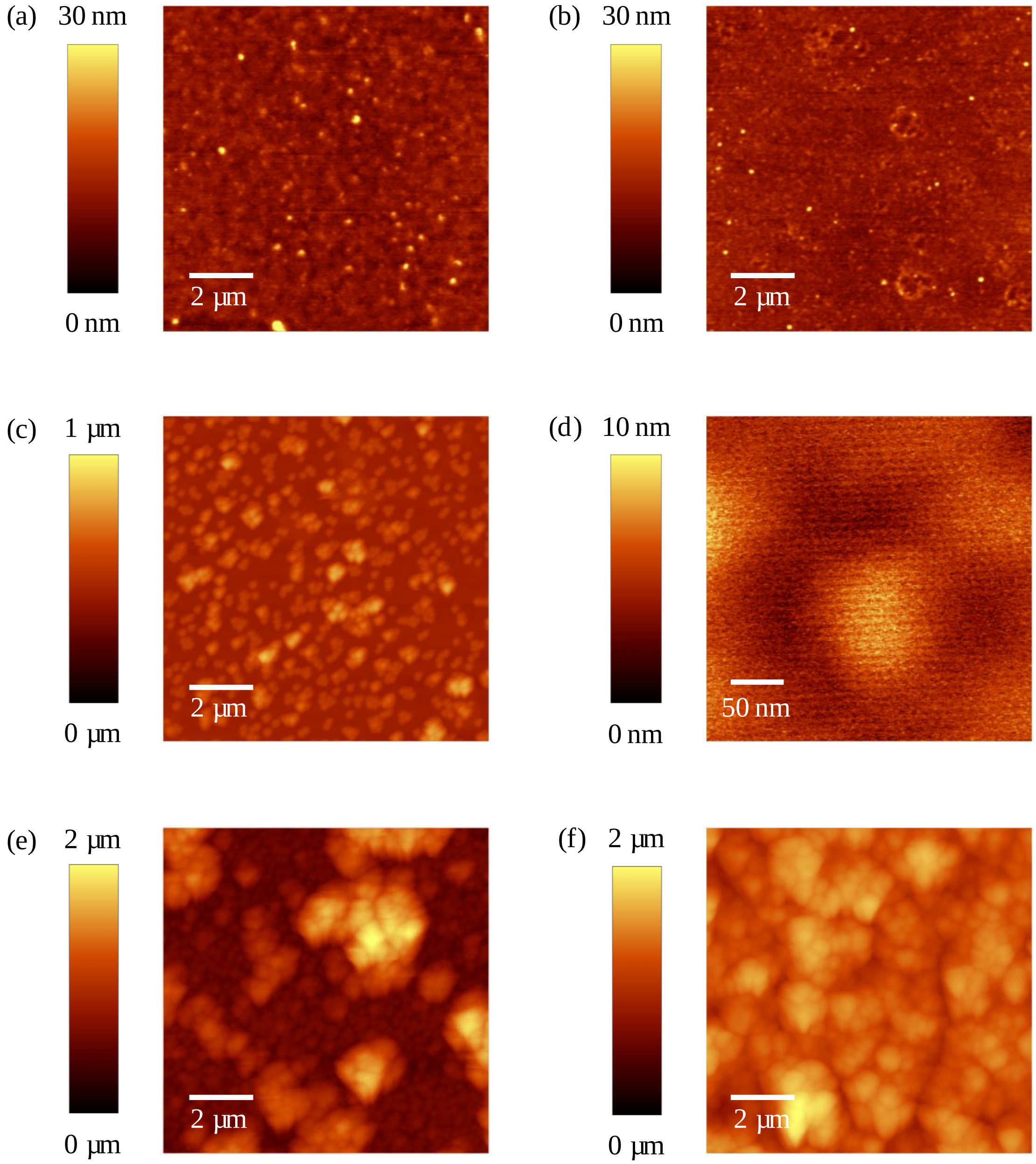

Figure 7.5. AFM topography image of (a) PEI-1, (b) PEI-2, (c) NCN-1, (d) the small silica nanoparticles on NCN-1, (e) NCN-2 , (f) NCN-3.

In the next step, the amine groups from PEI which was covalently attached to the Si surface in the previous step were initially reacted with excess of PNIPAM-c-PNASI. After the reaction, the resulting surface contained unreacted electrophilic NASI groups and was then immersed in a N,N-dimethylformamide (DMF) solution containing mixture of amine-functionalized 10 and 100 nm diameter silica nanoparticles (step B in Scheme 7.1). The NASI groups on the surface were expected to react with the amine groups on the silica nanoparticles to form amide bonds, which allowed the silica nanoparticles to be covalently attached on the surface. The surface was then treated with i-$PRNH_2$ to quantitatively convert any unreacted NASI groups to NIPAM groups. The topographic image shows that most of the 100 nm silica nanoparticles were well distributed on the surface after the treatment of step B (Figure 7.5c), while small amount of aggregates were observed as well. Due to the difference in height and image contrast, the 10 nm silica nanoparticles could not be seen directly on the 10 × 10 μm image which includes the 100 nm silica nanoparticles. The zoom-in regions around the 100 nm silica nanoparticles were scanned and the 10 nm silica nanoparticles were found to be well dispersed on the surface (Figure 7.5d). The surface roughness increased tremendously to 93 ± 27 nm at this stage, indicating that functionalizing the substrate with silica nanoparticles efficiently enlarges the roughness of the surface. Covalent layer-by-layer assembly of PNIPAM-c-PNASI with 10 and 100 nm amine-functionalized silica nanoparticles was repeated four more times. Since the top layer of the surface was covered with amine-functionalized silica nanoparticles after the treatment of step B, PNIPAM-c-PNASI was expected to continue reacting with the amine groups on the silica nanoparticles on the surface. New amine-functionalized silica nanoparticles were added to react with the NASI groups and covalently attached on the surface. As a result, aggregation of the silica nanoparticles on the surface occurred. Figure 7.5e is the AFM image of the surface after repeating step B one time. The 100 nm silica nanoparticles fully covered the surface and large aggregates of silica nanoparticles can be clearly observed in the image. The formation of the aggregates resulted in the enlargement of the surface roughness, which was 108 ± 36 nm in this stage. Repeating step B two times resulted in more aggregates of silica nanoparticles and polymer composite formed on the surface (Figure 7.5f). The large aggregates were all over the surface and the surface roughness increased to 196 ± 43 nm.

Figure 7.6a and b show the AFM images of the surface after repeating step B three and four times, respectively. The surface roughness increased as more and more aggregates formed on the surface. The surface roughness was 216 ± 18 nm and 246 ± 86 nm after repeating step B three and four times, respectively. In the final step, the surface was first treated with PNIPAM-c-PNASI/10 nm aminated silica nanoparticles/ *i*-PRNH_2, and then treated with PNIPAM-c-PNASI and *i*-PRNH_2 two times (Scheme 7.1). The 10 nm silica nanoparticles were expected to graft on the amine groups on the surface through the linkage of PNIPAM-c-PNASI. The AFM image shows that the surface in the final stage was fully covered by the nanoparticle-polymer composite (Figure 7.6c), while the surface roughness in this stage increased to ~288 ± 95 nm. The film thickness, which was measured by AFM, increased gradually during the layer-by-layer assembly process as expected since more and more polymer and silica nanoparticles were functionalized on the substrate (Table 7.1).

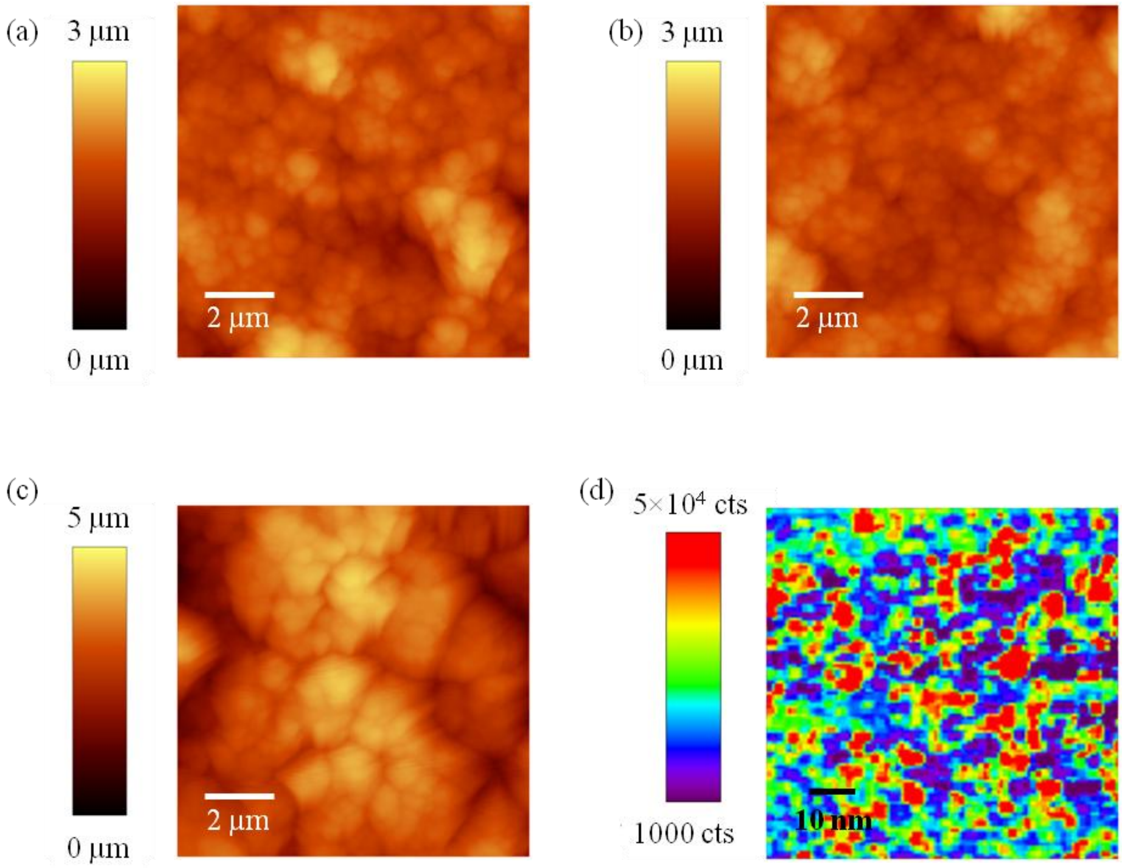

Figure 7.6. AFM topography image of (a) NCN-4, (b) NCN-5, (c) NCN-5+1, (d) Fluorescence image of NCN-5+1.

Table 7.1. Surface roughness and thickness of the nanocomposite at each stage.

	Si-APTES	PEI-1	PEI-2	NCN-1	NCN-2
Roughness (nm)	0.7	7 ± 3	6 ± 2	93 ± 27	108 ± 36
Thickness (μm)	-	a	b	0.3 ± 0.1	1.1 ± 0.1

*a: 11 ± 1 nm b: 23 ± 3 nm

	NCN-3	NCN-4	NCN-5	NCN-5+1
Roughness (nm)	196 ± 43	216 ± 18	246 ± 86	288 ± 95
Thickness (μm)	1.2 ± 0.1	1.6 ± 0.1	2.2 ± 0.4	2.4 ± 0.4

The nanocomposite-grafted PE films are found to exhibit reversible changes in surface wetting in response to solute anion identity and concentration, allowing surfaces to be switched from hydrophilic (advancing water contact angle 68°) to hydrophobic (advancing water contact angle 145°). The extent of the response to solute salts is found to be consistent with the Hofmeister series and with associated changes in surface roughness which result from varying degrees of polymer swelling in response to solute ion identity and concentration. The observed wettability changes on these surfaces are reversible. The results of the advancing water contact angle measurements are shown in Figure 7.7. For the kosmotropic anions, the results generally show a gradual increase in Θa values with increased salt concentration until a certain critical concentration of salt is reached. This is illustrated by the results for sodium citrate, Na_2SO_4, NaH_2PO_4, and

NaCl, where the increase in Θa with increased salt concentration exhibited sigmoidal behavior with inflection points that varied from around 0.6 M (sodium citrate) to 1.2 M (NaCl). In the case of chaotropic anions such as thiocyanate, salting-in behavior similar to that seen in the LCST behavior of PNIPAM,[234] hydroxymethylcellulose,[235] and other macromolecules[236] occurred. Salt-enhanced wetting is also seen for NaI, though the changes in Θa in this case are close to the error in contact angle measurements. All these surfaces had Θr values of <10°.

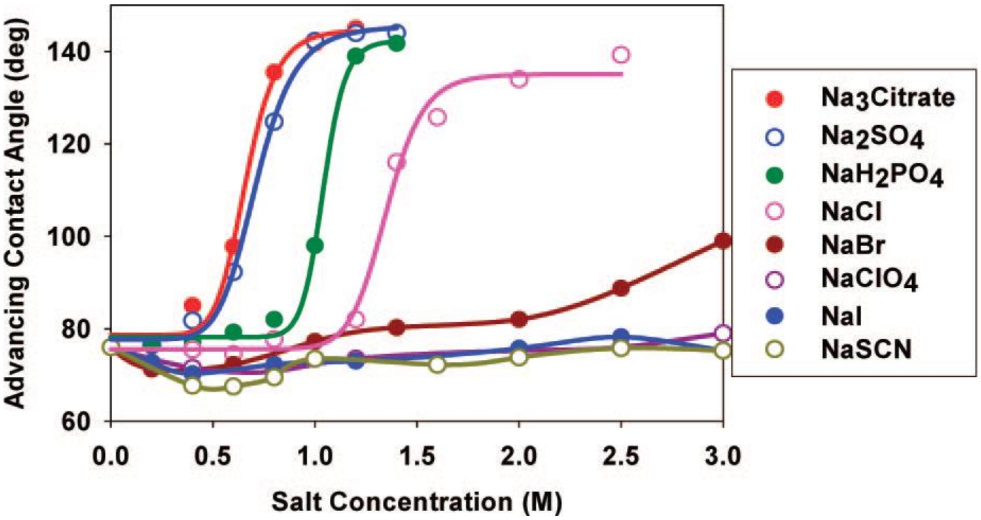

Figure 7.7. Changes in advancing contact angle (Θa) of a PE$_{oxid}$-(PNIPAM*c* PNASI/aminated silica nanoparticle)$_6$/PNIPAM surface measured with solutions of various salts as a function of salt concentration. Each data point is the average of three individual measurements and has an error of ± 2°. (Reproduced from ref. [233] with the permission of the copyright holders.)

The surface of PE_{oxid}-(PNIPAM-*c*-PNASI/ aminated silica nanoparticle)$_6$-PNIPAM was further characterized by AFM and in air had an average surface roughness of ~287 nm based on analysis of a random series of 2.5 μm × 2.5 μmregions. The AFM measurements of the surfaces show visible changes in surface texture when changing from one solute to the next (Figure 7.8). In air, the surfaces are rough and the larger silica particles (ca. 100 nm) dominate the surface morphology. Upon immersion in water, the film swells and the surface roughness decreases from ~287 nm rms to ~170 nm rms. Replacement of water by 1.4 M Na_2SO_4 results in an increase in roughness (ca. 232 nm rms) along with the ΔΘa of 68°. In 1.2 M NaSCN, the surface roughness decreased to~145nmrms and the Θa changed to 72° (ΔΘa of -4°). These changes show that these surfaces reconstruct in response to different solutes and suggest that the changes in water contact angle are likely due to a combination of changes in surface roughness induced by solute dependent swelling or chain collapse that alters the hydrophobicity of the PNIPAM. Hence, the swelling of the polymer on the textured surface follows the expected Hofmeister series which predictably alters the surface roughness and the associated wetting and dewetting of the surface.

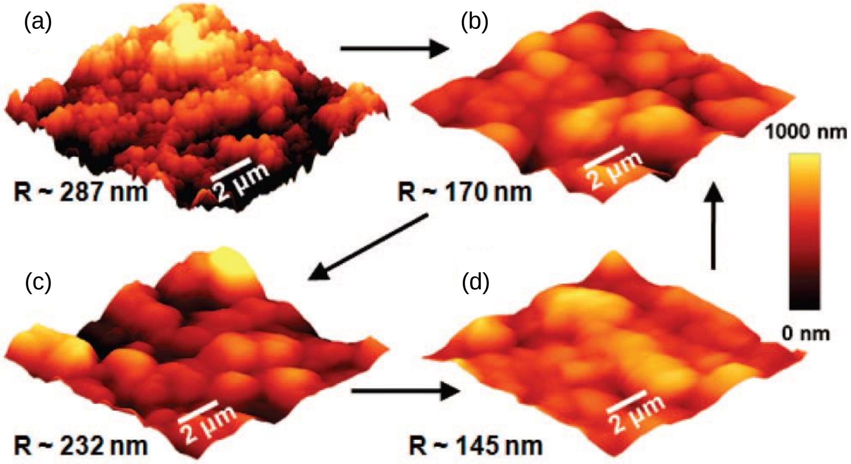

Figure 7.8. Tapping mode AFM images of PE_{oxid}-(PNIPAM-*c*-PNASI/ aminated silica nanoparticles$)_6$-PNIPAM obtained in (a) air, (b) water, (c) 1.4M Na_2SO_4, and (d) 1.2M NaSCN. Returning the sample to water yields an surface similar to (b). The average rms roughness of the surface in each environment taken from a random series of 2.5 μm × 2.5 μm regions is listed below each figure. (Reproduced from ref. [233] with the permission of the copyright holders.)

The influence of varying cation identity in a series of mono-, di-, and trivalent sulfate salts on the wettability of a stimuli-responsive grafted surface was also investigated by measuring advancing water contact angle (Θa) changes.[237] Figure 7.9 shows the influence of the type and concentration of cation sulfate salts on the advancing contact angles.

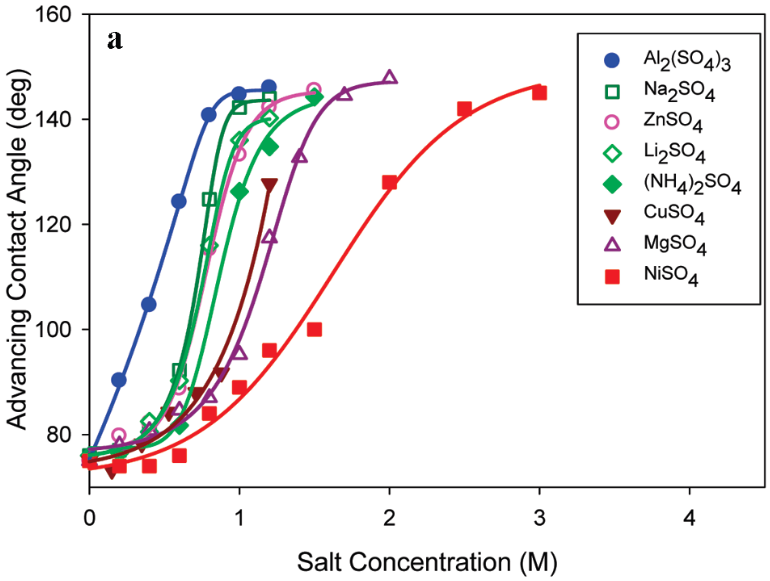

Figure 7.9. The advancing contact angles of various cation sulfate salts versus salt concentration. (Reproduced from ref. [237] with the permission of the copyright holders.)

The cation-induced changes inΘa were correlated with corresponding changes in surface morphology examined by AFM. A similar correlation between surface roughness and surface wettability with different cation sulfate solutions was also found by AFM on the PE_{oxid}-(PNIPAM/SiO_2)$_6$-PNIPAM surfaces (Figure 7.10). The 10 × 10 μm^2 AFM images were acquired multiple times under each condition. Similar morphology and roughness were observed between each measurement under the same conditions. Figure 7.10 shows typical topographic images and the average surface roughness of PE_{oxid}-(PNIPAM/SiO_2)$_6$- PNIPAM surfaces in air, water, 0.8 M $ZnSO_4$, and 1.2 M $ZnSO_4$. The PNIPAM/SiO_2 nanocomposite surface had both macro- and nanoscale roughness like the samples we prepared previously in air. This 224 nm rms roughness changed when the surface was exposed to water, dropping to a value of ~157 nm rms. This 157 nm rms roughness did not change significantly in the presence of 0.2Maqueous ZnSO4 (134 nm rms). However, treatment with a 0.8 M $ZnSO_4$ solution increased rms roughness to ~257 nm rms, which further increases to ~307 nm in the presence of 1.2 M $ZnSO_4$. As suggested above, these changes in roughness likely are due to changes in solvation of the nanocomposite graft. These changes in surface morphology are akin to those we observed in our earlier work. These changes observed by AFM correlate with the changes in wettability and are consistent with the notion that these cation sulfate salt solutes produce solute responsive swelling or chain collapse that altered the hydrophobicity of the PNIPAM component of the nanocomposite graft.

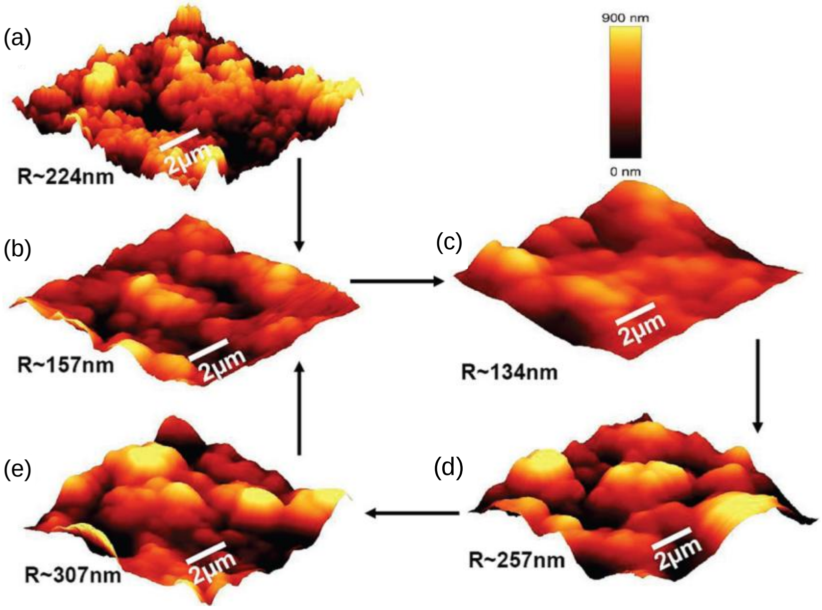

Figure 7.10. Tapping mode AFM images of a PE_{oxid}-$(PNIPAM/SiO_2)_6$-PNIPAM nanocomposite surface obtained in (a) air, (b) water, (c) 0.2 M $ZnSO_4$, (d) 0.8 M $ZnSO_4$, and (e) 1.2 M $ZnSO_4$. The average rms roughness of the surface in each environment was taken from six random 2.5 μm × 2.5 μm regions and the data were listed below each image (scale bar: 2 μm). (Reproduced from ref. [237] with the permission of the copyright holders.)

7.5. Summary

Superhydrophobic PE films and PE films with ion-responsive wettability were prepared by covalent layer-by-layer self-assembly and characterized by AFM. The superhydrophobic PE film consists of Gantrez/MWNT-NH-PEI and has a water contact angle of 165^o. The surface roughness and the morphology of the PE films at each stage of layer-by-layer process were determined by AFM and the surface roughness was found to be increased gradually during the assembly. This was found to be mainly contributed to the anticipation of MWNTs since without MWNTs the increase of surface roughness was much smaller after the assembly. The Raman signals of the G bands and D bands from MWNTs were further analyzed using confocal microscope and the results show that MWNTs were well dispersed in the nanocomposite.

The PE film with ion-responsive wettability was prepared by covalent layer-by-layer self-assembly using PNIPAM-c-PNASI copolymer, 10 nm and 100 nm aminated silica nanoparticles. The morphology and surface roughness of the nanocomposite were characterized by AFM during the assembly process. The AFM results show that the silica nanoparticles played a main role of increasing the surface roughness since the surface roughness increased drastically once the nanoparticles were grafted on the surface. The nanocomposite-grafted PE films are found to exhibit reversible changes in surface wetting in response to the solute identity and concentration of anion or cation, allowing surfaces to be switched from hydrophilic to hydrophobic. The surface roughness of the nanocomposite in the solution containing various identity or concentration of salts was characterized by AFM. The experimental results show that the changes in wettability may be due to the changes in surface roughness induced by solute dependent swelling or chain collapse that alters the hydrophobicity of the PNIPAM.

CHAPTER VIII

GENERAL CONCLUSIONS AND OUTLOOK

8.1. General Conclusions

The objective of this dissertation is to develop new methodologies to assemble well ordered porphyrin nanostructures and to understand how the arrangement of porphyrin molecules within the assemblies influences their morphologies, optical and photoluminescence properties. In this work, we first investigated characterized the nanostructures of tetra(*p*-carboxyphenyl)porphyrin (TCPP) formed in HCl solutions at various pH. We then researched on the porphyrin self-assembly in HBr solutions in order to study its counterion effect. The counterions were found to be a key role to organize the porphyrins into highly crystalline structures. Anion intercalation was further utilized to modulate the photoluminescence of the porphyrin assemblies, leading us to explore the optical memory effects of porphyrin thin films. Moreover, we studied the influence of surface energy on the morphologies of porphyrinoid nanoparticles by characterizing the nanoparticles on self-assembly monolayer surfaces. Lastly, we investigated the nanocomposites consisted of polymer/Si nanoparticles and polymer/carbon nanotubes nanocomposites by AFM to study the correlations between their surface roughnesses and their wettabilities.

In Chapter III and Chapter IV, we demonstrated well-defined porphyrin nanostructures were obtained by direct acidification of TCPP with HCl or HBr. Protonation the carboxylate groups of TCPP induced the aggregation of the porphyrin in aqueous solution. The structures of the aggregation were determined to be nanoplates based on the AFM and TEM characterization. Moreover, the absorption spectrum of the nanoplates reveals that they were assembled through the heat-to-tail aggregation (J-aggregation) of the porphyrin. The assembly of the nanoplates resulted in the fluorescence quenching and the short lifetime of the emission (0.1 ns), indicating their excited electrons were greatly quenched by the neighboring porphyrin possibly due to the strong exciton couplings. Further protonating the core nitrogens of TCPP formed the porphyrin diacids. The diacids self-assembled into highly crystalline nanofiber through their interaction in HCl solution and self-organized into nanoparticles or nanowires in HBr solution. The results of XPS and TEM elemental mapping provided the evidence of anion intercalation within the porphyrin assemblies. The results of CD spectroscopy show that the nanofibers formed in HCl solution exhibited positive chiroptical signals, whereas the nanoparticles and the nanowire bundles formed in HBr solution had positive cotton effect in the spectrum. This indicates although the porphyrin molecules are achiral, they self-organized into supramolecular chiral structures through the interactions between the porphyrin dications and the anions. Furthermore, compared to the nanoplates, the nanofibers strongly fluoresced and exhibited a much longer lifetime (3.2 ns). It is possible that intercalating chlorides into the porphyrin assemblies expanded the spacing between the porphyrin molecules and decreased the self-quenching of the porphyrin. Moreover, the nanofibers were found to have negative photoconductivity. Illuminating the nanofibers with white light reversibly decreased the current of the nanofibers.

In Chapter V, we explored the optical memory properties of porphyrin thin films on surfaces. The morphologies and the emission of TCPP nanostructures were found to be sensitive to the pH of the sounding solution. Immersing the thin film of TCPP nanoplates into a pH 1 HCl solution induced the formation of the porphyrin dications which further interacted with chlorides to form nanofibers. This process was found to be reversible since immersing the thin film into a pH 3 HCl solution deprotonated the core nitrogens of the dications, which transformed the nanofibers back to nanoplates. Furthermore, TCPP nanoplates fluoresce at 654 nm while TCPP nanofibers fluoresce at 714 nm in air. Thus the emission of the porphyrin thin film can be modulated by immersing the thin film in HCl solutions with controlled pH. We also demonstrated deprotonation of TCPP diacids can occur within the water meniscus between an AFM tip and the surface of the thin film. Therefore, fluorescence patterns can be "written" on the thin film of porphyrin nanofibers and be "read" by confocal microscope. The fluorescence patterns can be easily erased by immersing the thin film in a pH 1 HCl solution to re-protonate the porphyrin.

In Chapter VI, we characterize corrolazine nanoparticles deposited on a surface energy gradient to investigate how the surface energy affects the size of the nanoparticles. The surface energy gradient was prepared by selectively oxidizing a self-assembly monolayer of octadecyltrichlorosilane (OTS) using UV-ozone. We found that the nanoparticles tend to disassemble into smaller nanoparticles with smaller size distribution on the monolayer surface with higher surface energy.

In Chapter VII, we first characterized the surface of the superhydrophobic PE film constructed via the layer-by-layer assembly of Gantrez/MWNT-NH-PEI. The AFM results show that the superhydrophobicity of the Gantrez/MWNT-NH-PEI nanocompostes may be due to their extremely large surface roughness (~306 nm). The presence of MWNTs in the nanocomposite was found to be a key factor to effectively increase the surface roughness of the nanocomposite. We then characterized the morphologies and the surface roughness of the nanocompites which consisted of PNIPAM-c-PNASI copolymer, 10 nm and 100 nm aminated silica nanoparticles. The surface roughness of PNIPAM-c-PNASI/silica-nanoparticle nanocomposite was found to be varied by the concentration and identity of the cation and the anion in salt solution. This indicates the changes in wettability may be due to the variation of surface roughness induced by solute dependent swelling or chain collapse that alters the hydrophobicity of the PNIPAM.

8.2. Outlook

The future direction of this project will be utilizing the interaction between TCPP dications and different type of anions such as I^-, SO_4^{2-}, NO^{3-} to assemble new type of nanostructures. Our studies in this work reveal that the morphologies and optical properties of the porphyrin assemblies can be greatly influenced by the identity of the anions at low pH (< 2). We expect that utilizing different anions for the porphyrin self-assembly may vary the arrangement of the porphyrin molecules and their excitons coupling. The counterion effect may be used to modulate the photoluminescence and optoelectronic properties of the porphyrin assemblies. Moreover, changing the peripheral substituent of the porphyrin may also result in different types of structure due to the changes of the intermolecular interactions of the porphyrins and the solubility variation of the porphyrin molecules. For example, replacing the benzoic acid groups of TCPP to phenyl groups will make the porphyrin less hydrophilic with less hydrogen bonding and more π-π interactions. Changing the intermolecular interactions of porphyrins may influence the arrangement of the porphyrin molecules and affect the morphology of the porphyrin assemblies and the exciton couplings between the nearby molecules.

Another direction is to continuously research on TCPP nanofibers by transient absorption spectroscopy, which may provides useful information of the excited energy states of TCPP diacids within the nanofibers. As static and time-resolved spectrofluorometry can be used to detect the energy states of the porphyrin based on the radiative decays of the excited electrons, transient absorption spectroscopy can be utilized to measure the kinetics of both radiative and non-radiative decays of the excited electrons. Therefore, by performing the transient absorption measurement, energy states (such as trap states) of the porphyrin that are not observed in the fluorescence spectrum may be obtained. The results of the transient absorption measurement might be used to explain the negative photoconductivity of the porphyrin nanofibers (see Chapter III).

The other future direction of this research can be utilizing other approaches such as metal-ligand coordination to assemble organic nanostructures. The coordination chemistry of organometallic compounds has been intensively studied and widely reported in the literature. By controlling the concentration of the reactants and the reaction conditions, well-defines nanostructures with unique chemical and physical properties may be fabricated. For example, porphyrin nanoparticles can be obtained via the coordination between the carboxylic acid groups of ZnTCPP with Zn ions. Moreover, comparing with free-base porphyrins, metallic porphyrins typically have longer lifetimes (sometime phosphoresce) due to the heavy-metal effect. Thus the nanostructures of organometallic complex may have potential applications in phototherapy, sensors, and optoelectronic devices.

At this time, many questions still need to be answered in the field of porphyrin nanostructures. There is still lack of theory that can be used to predict the structure of the assemblies based on the porphyrin molecular structures, inter or intramolecular interactions between the porphyrins, and the synthesis conditions. Although the photoluminescence (lifetime, quantum yield) and optoelectronic properties of TCPP nanofibers have been studied in this work, these properties in other porphyrin systems remain unclear. The main challenge in this research field is that in most cases, there is not much information of the molecular arrangement of the porphyrins within the nanostructures. This could be due to lack of long range periodicity of the molecules in the nanostructures, and the diffusion of the Bragg's peaks in the XRD spectrum, which are frequently observed when measuring materials in nanoscale. One approach to obtain structural information of the nanostructures is to perform Pair Distribution Function (PDF) measurement, which deconvolutes the Bragg-like peaks and the diffusion scattering (non-Brag-like peaks),[238] providing a route to solve the 3-D molecular structures in the assemblies. We believe that by combining the detail information of the molecular arrangement of porphyrins inside their nanostructures and the clarification of their excited energy states, it is possible to build theoretical models to explain how the molecular structures within the porphyrin assemblies affect the porphyrin photoluminescence and optoelectronic properties. This may led us to understand more about the electron or energy transfer mechanisms within the porphyrin assemblies in biological systems and to develop new solar cells for clean energy conversion.

REFERENCES

(1) Imahori, H.; Umeyama, T.; Ito, S. *Accounts of Chemical Research* **2009**, *42*, 1809.

(2) Gao, F.; Wang, Y.; Shi, D.; Zhang, J.; Wang, M. K.; Jing, X. Y.; Humphry-Baker, R.; Wang, P.; Zakeeruddin, S. M.; Gratzel, M. *Journal of the American Chemical Society* **2008**, *130*, 10720.

(3) Hagfeldt, A.; Gratzel, M. *Accounts of Chemical Research* **2000**, *33*, 269.

(4) Nazeeruddin, M. K.; De Angelis, F.; Fantacci, S.; Selloni, A.; Viscardi, G.; Liska, P.; Ito, S.; Bessho, T.; Gratzel, M. *Journal of the American Chemical Society* **2005**, *127*, 16835.

(5) Yum, J. H.; Chen, P.; Gratzel, M.; Nazeeruddin, M. K. *Chemsuschem* **2008**, *1*, 699.

(6) Barber, J.; Andersson, B. *Nature* **1994**, *370*, 31.

(7) Fromme, P. *Current Opinion in Structural Biology* **1996**, *6*, 473.

(8) Krauss, N.; Schubert, W. D.; Klukas, O.; Fromme, P.; Witt, H. T.; Saenger, W. *Nature Structural Biology* **1996**, *3*, 965.

(9) Nakamura, Y.; Aratani, N.; Osuka, A. *Chemical Society Reviews* **2007**, *36*, 831.

(10) Nakano, A.; Yasuda, Y.; Yamazaki, T.; Akimoto, S.; Yamazaki, I.; Miyasaka, H.; Itaya, A.; Murakami, M.; Osuka, A. *Journal of Physical Chemistry A* **2001**, *105*, 4822.

(11) Watson, D. F.; Marton, A.; Stux, A. M.; Meyer, G. J. *Journal of Physical Chemistry B* **2004**, *108*, 11680.

(12) Imahori, H.; Hayashi, S.; Umeyama, T.; Eu, S.; Oguro, A.; Kang, S.; Matano, Y.; Shishido, T.; Ngamsinlapasathian, S.; Yoshikawa, S. *Langmuir* **2006**, *22*, 11405.

(13) Eu, S.; Hayashi, S.; Umeyama, T.; Oguro, A.; Kawasaki, M.; Kadota, N.; Matano, Y.; Imahori, H. *Journal of Physical Chemistry C* **2007**, *111*, 3528.

(14) Hayashi, S.; Matsubara, Y.; Eu, S.; Hayashi, H.; Umeyama, T.; Matano, Y.; Imahori, H. *Chemistry Letters* **2008**, *37*, 846.

(15) Hayashi, S.; Tanaka, M.; Hayashi, H.; Eu, S.; Umeyama, T.; Matano, Y.; Araki, Y.; Imahori, H. *Journal of Physical Chemistry C* **2008**, *112*, 15576.

(16) Gust, D.; Moore, T. A. *Science* **1989**, *244*, 35.

(17) Rybtchinski, B.; Sinks, L. E.; Wasielewski, M. R. *Journal of the American Chemical Society* **2004**, *126*, 12268.

(18) Guldi, D. M.; Rahman, G. M. A.; Zerbetto, F.; Prato, M. *Accounts of Chemical Research* **2005**, *38*, 871.

(19) Hasobe, T.; Saito, K.; Kamat, P. V.; Troiani, V.; Qiu, H. J.; Solladie, N.; Kim, K. S.; Park, J. K.; Kim, D.; D'Souza, F.; Fukuzumi, S. *Journal of Materials Chemistry* **2007**, *17*, 4160.

(20) Hasobe, T.; Imahori, H.; Kamat, P. V.; Ahn, T. K.; Kim, S. K.; Kim, D.; Fujimoto, A.; Hirakawa, T.; Fukuzumi, S. *Journal of the American Chemical Society* **2005**, *127*, 1216.

(21) Imahori, H.; Yamada, H.; Guldi, D. M.; Endo, Y.; Shimomura, A.; Kundu, S.; Yamada, K.; Okada, T.; Sakata, Y.; Fukuzumi, S. *Angewandte Chemie-International Edition* **2002**, *41*, 2344.

(22) Hasobe, T.; Murata, H.; Kamat, P. V. *Journal of Physical Chemistry C* **2007**, *111*, 16626.

(23) Stang, P. J.; Olenyuk, B. *Accounts of Chemical Research* **1997**, *30*, 502.

(24) Lucia, L. A.; Yui, T.; Sasai, R.; Takagi, S.; Takagi, K.; Yoshida, H.; Whitten, D. G.; Inoue, H. *Journal of Physical Chemistry B* **2003**, *107*, 3789.

(25) Nakano, A.; Osuka, A.; Yamazaki, T.; Nishimura, Y.; Akimoto, S.; Yamazaki, I.; Itaya, A.; Murakami, M.; Miyasaka, H. *Chemistry-a European Journal* **2001**, *7*, 3134.

(26) Hu, X. C.; Schulten, K. *Physics Today* **1997**, *50*, 28.

(27) Martinez-Planells, A.; Arellano, J. B.; Borrego, C. A.; Lopez-Iglesias, C.; Gich, F.; Garcia-Gil, J. S. *Photosynthesis Research* **2002**, *71*, 83.

(28) Bahatyrova, S.; Frese, R. N.; Siebert, C. A.; Olsen, J. D.; van der Werf, K. O.; van Grondelle, R.; Niederman, R. A.; Bullough, P. A.; Otto, C.; Hunter, C. N. *Nature* **2004**, *430*, 1058.

(29) McDermott, G.; Prince, S. M.; Freer, A. A.; Hawthornthwaitelawless, A. M.; Papiz, M. Z.; Cogdell, R. J.; Isaacs, N. W. *Nature* **1995**, *374*, 517.

(30) Koepke, J.; Hu, X. C.; Muenke, C.; Schulten, K.; Michel, H. *Structure* **1996**, *4*, 581.

(31) Olson, J. M. *Photochemistry and Photobiology* **1998**, *67*, 61.

(32) van Grondelle, R.; Novoderezhkin, V. I. *Physical Chemistry Chemical Physics* **2006**, *8*, 793.

(33) Gong, X. C.; Milic, T.; Xu, C.; Batteas, J. D.; Drain, C. M. *Journal of the American Chemical Society* **2002**, *124*, 14290.

(34) Osswald, P.; You, C. C.; Stepanenko, V.; Wurthner, F. *Chemistry-a European Journal* **2010**, *16*, 2386.

(35) Kashani-Motlagh, M. M.; Rahimi, R.; Kachousangi, M. J. *Molecules* **2010**, *15*, 280.

(36) Perepogu, A. K.; Bangal, P. R. *Journal of Chemical Sciences* **2008**, *120*, 485.

(37) Ou, Z. M.; Yao, H.; Kimura, K. *Journal of Photochemistry and Photobiology a-Chemistry* **2007**, *189*, 7.

(38) Drain, C. M.; Smeureanu, G.; Patel, S.; Gong, X. C.; Garno, J.; Arijeloye, J. *New Journal of Chemistry* **2006**, *30*, 1834.

(39) Ou, Z.; Yao, H.; Kimura, K. *Chemistry Letters* **2006**, *35*, 782.

(40) Schwab, A. D.; Smith, D. E.; Rich, C. S.; Young, E. R.; Smith, W. F.; de Paula, J. C. *Journal of Physical Chemistry B* **2003**, *107*, 11339.

(41) Friesen, B. A.; Wiggins, B.; McHale, J. L.; Mazur, U.; Hipps, K. W. *Journal of the American Chemical Society* **2010**, *132*, 8554.

(42) Micali, N.; Villari, V.; Castriciano, M. A.; Romeo, A.; Scolaro, L. M. *Journal of Physical Chemistry B* **2006**, *110*, 8289.

(43) Wang, Z. C.; Li, Z. Y.; Medforth, C. J.; Shelnutt, J. A. *Journal of the American Chemical Society* **2007**, *129*, 2440.

(44) Wang, Z. C.; Medforth, C. J.; Shelnutt, J. A. *Journal of the American Chemical Society* **2004**, *126*, 15954.

(45) Wang, Z. C.; Medforth, C. J.; Shelnutt, J. A. *Journal of the American Chemical Society* **2004**, *126*, 16720.

(46) Weisz, P. B. *Physics Today* **2004**, *57*, 47.

(47) Bartlett, A. A. *American Journal of Physics* **1986**, *54*, 398.

(48) Myers, N.; Kent, J. *Proceedings of the National Academy of Sciences of the United States of America* **2003**, *100*, 4963.

(49) Raupach, M. R.; Marland, G.; Ciais, P.; Le Quere, C.; Canadell, J. G.; Klepper, G.; Field, C. B. *Proceedings of the National Academy of Sciences of the United States of America* **2007**, *104*, 10288.

(50) Fluckiger, J.; Monnin, E.; Stauffer, B.; Schwander, J.; Stocker, T. F.; Chappellaz, J.; Raynaud, D.; Barnola, J. M. *Global Biogeochemical Cycles* **2002**, *16*.

(51) Keeling, C. D.; Bacastow, R. B.; Bainbridge, A. E.; Ekdahl, C. A.; Guenther, P. R.; Waterman, L. S.; Chin, J. F. S. *Tellus* **1976**, *28*, 538.

(52) Thoning, K. W.; Tans, P. P.; Komhyr, W. D. *Journal of Geophysical Research-Atmospheres* **1989**, *94*, 8549.

(53) Karlen, W. *Ambio* **1998**, *27*, 270.

(54) Tol, R. S. J.; De Vos, A. F. *Climatic Change* **1998**, *38*, 87.

(55) Lambert, S. J. *Journal of Climate* **1995**, *8*, 1447.

(56) Brereton, R.; Bennett, S.; Mansergh, I. *Biological Conservation* **1995**, *72*, 339.

(57) Whetton, P. H.; Fowler, A. M.; Haylock, M. R.; Pittock, A. B. *Climatic Change* **1993**, *25*, 289.

(58) Gordon, H. B.; Whetton, P. H.; Pittock, A. B.; Fowler, A. M.; Haylock, M. R. *Climate Dynamics* **1992**, *8*, 83.

(59) Beyschlag, W.; Barnes, P. W.; Flint, S. D.; Caldwell, M. M. *Photosynthetica* **1988**, *22*, 516.

(60) Sawin, J. L.; Martinot, E. *Renewables Global Status Report* **2010,** 10.

(61) Hillhouse, H. W.; Beard, M. C. *Current Opinion in Colloid & Interface Science* **2009**, *14*, 245.

(62) Oregan, B.; Gratzel, M. *Nature* **1991**, *353*, 737.

(63) Nazeeruddin, M. K.; Kay, A.; Rodicio, I.; Humphrybaker, R.; Muller, E.; Liska, P.; Vlachopoulos, N.; Gratzel, M. *Journal of the American Chemical Society* **1993**, *115*, 6382.

(64) Gratzel, M. *Nature* **2001**, *414*, 338.

(65) Bach, U.; Lupo, D.; Comte, P.; Moser, J. E.; Weissortel, F.; Salbeck, J.; Spreitzer, H.; Gratzel, M. *Nature* **1998**, *395*, 583.

(66) Nazeeruddin, M. K.; Pechy, P.; Renouard, T.; Zakeeruddin, S. M.; Humphry-Baker, R.; Comte, P.; Liska, P.; Cevey, L.; Costa, E.; Shklover, V.; Spiccia, L.; Deacon, G. B.; Bignozzi, C. A.; Gratzel, M. *Journal of the American Chemical Society* **2001**, *123*, 1613.

(67) Gratzel, M. *Inorganic Chemistry* **2005**, *44*, 6841.

(68) Zang, L.; Che, Y. K.; Moore, J. S. *Accounts of Chemical Research* **2008**, *41*, 1596.

(69) Iyoda, M.; Hasegawa, M.; Enozawa, H. *Chemistry Letters* **2007**, *36*, 1402.

(70) Nguyen, T. Q.; Martel, R.; Bushey, M.; Avouris, P.; Carlsen, A.; Nuckolls, C.; Brus, L. *Physical Chemistry Chemical Physics* **2007**, *9*, 1515.

(71) Balakrishnan, K.; Datar, A.; Oitker, R.; Chen, H.; Zuo, J. M.; Zang, L. *Journal of the American Chemical Society* **2005**, *127*, 10496.

(72) Lindner, S. M.; Thelakkat, M. *Macromolecules* **2004**, *37*, 8832.

(73) Stupp, S. I.; Pralle, M. U.; Tew, G. N.; Li, L. M.; Sayar, M.; Zubarev, E. R. *MRS Bulletin* **2000**, *25*, 42.

(74) Krysmann, M. J.; Castelletto, V.; McKendrick, J. E.; Clifton, L. A.; Hamley, I. W.; Harris, P. J. F.; King, S. A. *Langmuir* **2008**, *24*, 8158.

(75) Chou, J.-H. K., M. E.; Nalwa, H. S.; Rakow, N. A.; Suslick,; S., K. *The Porphyrin Handbook*; Acedamic Press: New York, 2000; pp 41.

(76) Kadish, K. M., Smith, K. M., Guilard,; R., E. *The Porphyrin Handbook*; Acedamic Press: New York 2000; pp 43.

(77) Chambron, J.-C. H., V.; Sauvage, J.-P. *The Porphyrin Handbook*; Acedamic Press: New York, 2000; pp 40.

(78) Kadish, K. M., Smith, K. M., Guilard, R., Eds. *The Porphyrin Handbook*; Acedamic Press: New York, 2000; pp 1.

(79) Zingg, A.; Felber, B.; Gramlich, V.; Fu, L.; Collman, J. P.; Diederich, F. *Helvetica Chimica Acta* **2002**, *85*, 333.

(80) Perutz, M. F.; Rossmann, M. G.; Cullis, A. F.; Muirhead, H.; Will, G.; North, A. C. T. *Nature* **1960**, *185*, 416.

(81) Reddy, K. S.; Yonetani, T.; Tsuneshige, A.; Chance, B.; Kushkuley, B.; Stavrov, S. S.; Vanderkooi, J. M. *Biochemistry* **1996**, *35*, 5562.

(82) Cullis, A. F.; Rossmann, M. G.; Muirhead, H.; Perutz, M. F.; North, A. C. T. *Proceedings of the Royal Society of London Series a-Mathematical and Physical Sciences* **1962**, *265*, 161.

(83) Collman, J. P.; Fu, L.; Herrmann, P. C.; Zhang, X. M. *Science* **1997**, *275*, 949.

(84) Nanthakumar, A.; Fox, S.; Murthy, N. N.; Karlin, K. D.; Ravi, N.; Huynh, B. H.; Orosz, R. D.; Day, E. P.; Hagen, K. S.; Blackburn, N. J. *Journal of the American Chemical Society* **1993**, *115*, 8513.

(85) Collman, J. P.; Marrocco, M.; Denisevich, P.; Koval, C.; Anson, F. C. *Journal of Electroanalytical Chemistry* **1979**, *101*, 117.

(86) Lyon, D. K.; Miller, W. K.; Novet, T.; Domaille, P. J.; Evitt, E.; Johnson, D. C.; Finke, R. G. *Journal of the American Chemical Society* **1991**, *113*, 7209.

(87) Mansuy, D.; Bartoli, J. F.; Battioni, P.; Lyon, D. K.; Finke, R. G. *Journal of the American Chemical Society* **1991**, *113*, 7222.

(88) Durand, R. R.; Anson, F. C. *Journal of Electroanalytical Chemistry* **1982**, *134*, 273.

(89) Gojkovic, S. L.; Gupta, S.; Savinell, R. F. *Journal of Electroanalytical Chemistry* **1999**, *462*, 63.

(90) Liu, H. Y.; Abdalmuhdi, I.; Chang, C. K.; Anson, F. C. *Journal of Physical Chemistry* **1985**, *89*, 665.

(91) Shi, C.; Anson, F. C. *Journal of the American Chemical Society* **1991**, *113*, 9564.

(92) Zhou, C. Y.; Chan, P. W. H.; Che, C. M. *Organic Letters* **2006**, *8*, 325.

(93) Nam, W. O.; Lim, M. H.; Lee, H. J.; Kim, C. *Journal of the American Chemical Society* **2000**, *122*, 6641.

(94) Galardon, E.; Le Maux, P.; Simonneaux, G. *Tetrahedron* **2000**, *56*, 615.

(95) Gross, Z.; Ini, S. *Organic Letters* **1999**, *1*, 2077.

(96) Kubo, Y.; Yamamoto, M.; Ikeda, M.; Takeuchi, M.; Shinkai, S.; Yamaguchi, S.; Tamao, K. *Angewandte Chemie-International Edition* **2003**, *42*, 2036.

(97) Daunert, S.; Wallace, S.; Florido, A.; Bachas, L. G. *Analytical Chemistry* **1991**, *63*, 1676.

(98) Mills, A.; Lepre, A. *Analytical Chemistry* **1997**, *69*, 4653.

(99) Hartmann, P.; Trettnak, W. *Analytical Chemistry* **1996**, *68*, 2615.

(100) Lee, S. K.; Okura, I. *Analyst* **1997**, *122*, 81.

(101) Plaschke, M.; Czolk, R.; Ache, H. J. *Analytica Chimica Acta* **1995**, *304*, 107.

(102) Lee, S. K.; Okura, I. *Analytica Chimica Acta* **1997**, *342*, 181.

(103) Lee, S. K.; Okura, I. *Analytical Communications* **1997**, *34*, 185.

(104) Bonnett, R. *Chemical Society Reviews* **1995**, *24*, 19.

(105) Sternberg, E. D.; Dolphin, D.; Bruckner, C. *Tetrahedron* **1998**, *54*, 4151.

(106) Bown, S. G.; Tralau, C. J.; Smith, P. D. C.; Akdemir, D.; Wieman, T. J. *British Journal of Cancer* **1986**, *54*, 43.

(107) Pandey, R. K.; Bellnier, D. A.; Smith, K. M.; Dougherty, T. J. *Photochemistry and Photobiology* **1991**, *53*, 65.

(108) Vanderveen, N.; Vanleengoed, H.; Star, W. M. *British Journal of Cancer* **1994**, *70*, 867.

(109) Messmann, H.; Mlkvy, P.; Buonaccorsi, G.; Davies, C. L.; Macrobert, A.; Bown, S. G. *British Journal of Cancer* **1995**, *72*, 589.

(110) Pandey, R. K.; Smith, K. M.; Dougherty, T. J. *Journal of Medicinal Chemistry* **1990**, *33*, 2032.

(111) Renge, I.; Wild, U. P. *Journal of Physical Chemistry A* **1997**, *101*, 7977.

(112) Wertsching, A. K.; Koch, A. S.; DiMagno, S. G. *Journal of the American Chemical Society* **2001**, *123*, 3932.

(113) Mack, J.; Stillman, M. J. *Coordination Chemistry Reviews* **2001**, *219*, 993.

(114) Sundholm, D. *Chemical Physics Letters* **2000**, *317*, 392.

(115) Rubio, M.; Roos, B. O.; Serrano-Andres, L.; Merchan, M. *Journal of Chemical Physics* **1999**, *110*, 7202.

(116) Levy, S. T.; Rubin, M. B.; Speiser, S. *Journal of the American Chemical Society* **1992**, *114*, 10747.

(117) Mack, J.; Stillman, M. J. *Journal of Porphyrins and Phthalocyanines* **2001**, *5*, 67.

(118) Gouterman, M. *Journal of Chemical Physics* **1959**, *30*, 1139.

(119) Gouterman, M. *Journal of Molecular Spectroscopy* **1961**, *6*, 138.

(120) Weiss, C.; Kobayash.H; Gouterma.M *Journal of Molecular Spectroscopy* **1965**, *16*, 415.

(121) Gouterman, M.; Snyder, L. C.; Wagniere, G. H. *Journal of Molecular Spectroscopy* **1963**, *11*, 108.

(122) Ma, H. L.; Jin, W. J. *Spectrochimica Acta Part a-Molecular and Biomolecular Spectroscopy* **2008**, *71*, 153.

(123) Zimmermann, J.; Siggel, U.; Fuhrhop, J. H.; Roder, B. *Journal of Physical Chemistry B* **2003**, *107*, 6019.

(124) Aziz, A.; Narasimhan, K. L.; Periasamy, N.; Maiti, N. C. *Philosophical Magazine B-Physics of Condensed Matter Statistical Mechanics Electronic Optical and Magnetic Properties* **1999**, *79*, 993.

(125) Ohno, O.; Kaizu, Y.; Kobayashi, H. *Journal of Chemical Physics* **1993**, *99*, 4128.

(126) Kasha, M. *Radiation Research* **1963**, *20*, 55.

(127) Levinson, Y. B.; Rashba, E. I. *Reports on Progress in Physics* **1973**, *36*, 1499.

(128) Zhuang, X. D.; Chen, Y.; Liu, Y.; Cai, L. Z.; Lin, Y. *Progress in Chemistry* **2007**, *19*, 1653.

(129) Zheng, C. C.; Xu, X. J.; He, F.; Li, L. D.; Wu, B.; Yu, G.; Liu, Y. Q. *Langmuir* **2010**, *26*, 16730.

(130) Bai, F.; Wu, H. M.; Haddad, R. E.; Sun, Z. C.; Schmitt, S. K.; Skocypec, V. R.; Fan, H. Y. *Chemical Communications* **2010**, *46*, 4941.

(131) Guo, X. M.; Guo, B.; Shi, T. S. *Inorganica Chimica Acta* **2010**, *363*, 317.

(132) Sandanayaka, A. S. D.; Murakami, T.; Hasobe, T. *Journal of Physical Chemistry C* **2009**, *113*, 18369.

(133) Friesen, B. A.; Nishida, K. R. A.; McHale, J. L.; Mazur, U. *Journal of Physical Chemistry C* **2009**, *113*, 1709.

(134) Fathalla, M.; Neuberger, A.; Li, S. C.; Schmehl, R.; Diebold, U.; Jayawickramarajah, J. *Journal of the American Chemical Society* **2010**, *132*, 9966.

(135) Jintoku, H.; Sagawa, T.; Takafuji, M.; Ihara, H. *Organic & Biomolecular Chemistry* **2009**, *7*, 2430.

(136) Lee, S. J.; Hupp, J. T.; Nguyen, S. T. *Journal of the American Chemical Society* **2008**, *130*, 9632.

(137) Hu, J. S.; Guo, Y. G.; Liang, H. P.; Wan, L. J.; Jiang, L. *Journal of the American Chemical Society* **2005**, *127*, 17090.

(138) Wang, Z. C.; Ho, K. C. J.; Medforth, C. J.; Shelnutt, J. A. *Advanced Materials* **2006**, *18*, 2557.

(139) Martin, K. E.; Wang, Z. C.; Busani, T.; Garcia, R. M.; Chen, Z.; Jiang, Y. B.; Song, Y. J.; Jacobsen, J. L.; Vu, T. T.; Schore, N. E.; Swartzentruber, B. S.; Medforth, C. J.; Shelnutt, J. A. *Journal of the American Chemical Society* **2010**, *132*, 8194.

(140) Yoon, S. M.; Hwang, I. C.; Kim, K. S.; Choi, H. C. *Angewandte Chemie-International Edition* **2009**, *48*, 2506.

(141) Zhang, Y. J.; Dong, H. L.; Tang, Q. X.; Ferdous, S.; Liu, F.; Mannsfeld, S. C. B.; Hu, W. P.; Briseno, A. L. *Journal of the American Chemical Society* **2010**, *132*, 11580.

(142) Zhang, Y. J.; Dong, H. L.; Tang, Q. X.; He, Y. D.; Hu, W. P. *Journal of Materials Chemistry* **2010**, *20*, 7029.

(143) Sharma, C. V. K.; Broker, G. A.; Huddleston, J. G.; Baldwin, J. W.; Metzger, R. M.; Rogers, R. D. *Journal of the American Chemical Society* **1999**, *121*, 1137.

(144) Goldberg, I. *Chemical Communications* **2005**, 1243.

(145) Kumar, R. K.; Balasubramanian, S.; Goldberg, I. *Inorganic Chemistry* **1998**, *37*, 541.

(146) Krupitsky, H.; Stein, Z.; Goldberg, I.; Strouse, C. E. *Journal of Inclusion Phenomena and Molecular Recognition in Chemistry* **1994**, *18*, 177.

(147) Dastidar, P.; Stein, Z.; Goldberg, I.; Strouse, C. E. *Supramolecular Chemistry* **1996**, *7*, 257.

(148) Deiters, E.; Bulach, V.; Hosseini, M. W. *Chemical Communications* **2005**, 3906.

(149) Drain, C. M.; Goldberg, I.; Sylvain, I.; Falber, A. *Functional Molecular Nanostructures*; Springer: New York, 2005; pp 55.

(150) Diskin-Posner, Y.; Patra, G. K.; Goldberg, I. *Journal of the Chemical Society-Dalton Transactions* **2001**, 2775.

(151) Shmilovits, M.; Diskin-Posner, Y.; Vinodu, M.; Goldberg, I. *Crystal Growth & Design* **2003**, *3*, 855.

(152) Wang, Z.; Lybarger, L. E.; Wang, W.; Medforth, C. J.; Miller, J. E.; Shelnutt, J. A. *Nanotechnology* **2008**, *19*.

(153) Ali, M.; Kumar, V.; Baker, S. N.; Baker, G. A.; Pandey, S. *Physical Chemistry Chemical Physics* **2010**, *12*, 1886.

(154) Doan, S. C.; Shanmugham, S.; Aston, D. E.; McHale, J. L. *Journal of the American Chemical Society* **2005**, *127*, 5885.

(155) Choi, M. Y.; Pollard, J. A.; Webb, M. A.; McHale, J. L. *Journal of the American Chemical Society* **2003**, *125*, 810.

(156) De Souza, L. A.; Da Silva, A. M.; Junqueira, G. M. A.; Carvalho, A. C. M.; Dos Santos, H. F. *Journal of Molecular Structure-Theochem* **2010**, *959*, 92.

(157) Huang, C. S.; Li, Y. L.; Song, Y. L.; Li, Y. J.; Liu, H. B.; Zhu, D. B. *Advanced Materials* **2010**, *22*, 3532.

(158) Vlaming, S. M.; Augulis, R.; Stuart, M. C. A.; Knoester, J.; van Loosdrecht, P. H. M. *Journal of Physical Chemistry B* **2009**, *113*, 2273.

(159) Sandanayaka, A. S. D.; Araki, Y.; Wada, T.; Hasobe, T. *Journal of Physical Chemistry C* **2008**, *112*, 19209.

(160) Duan, X. F.; Wang, J. L.; Pei, J. *Organic Letters* **2005**, *7*, 4071.

(161) Riley, C. K.; Muller, E. A.; Feldman, B. E.; Cross, C. M.; Van Aken, K. L.; Johnston, D. E.; Lu, Y.; Johnson, A. T.; de Paula, J. C.; Smith, W. F. *Journal of Physical Chemistry C* **2010**, *114*, 19227.

(162) Li, C.; Ly, J.; Lei, B.; Fan, W.; Zhang, D. H.; Han, J.; Meyyappan, M.; Thompson, M.; Zhou, C. W. *Journal of Physical Chemistry B* **2004**, *108*, 9646.

(163) Cho, K.; Kerber, W. D.; Lee, S. R.; Wan, A.; Batteas, J. D.; Goldberg, D. P. *Inorganic Chemistry* **2010**, *49*, 8465.

(164) Liu, G. Y.; Xu, S.; Qian, Y. L. *Accounts of Chemical Research* **2000**, *33*, 457.

(165) Wadu-Mesthrige, K.; Xu, S.; Amro, N. A.; Liu, G. Y. *Langmuir* **1999**, *15*, 8580.

(166) Amro, N. A.; Xu, S.; Liu, G. Y. *Langmuir* **2000**, *16*, 3006.

(167) Liu, M. Z.; Amro, N. A.; Chow, C. S.; Liu, G. Y. *Nano Letters* **2002**, *2*, 863.

(168) Liu, J. F.; Cruchon-Dupeyrat, S.; Garno, J. C.; Frommer, J.; Liu, G. Y. *Nano Letters* **2002**, *2*, 937.

(169) Xu, S.; Liu, G. Y. *Langmuir* **1997**, *13*, 127.

(170) Shi, J. J.; Chen, J. X.; Cremer, P. S. *Journal of the American Chemical Society* **2008**, *130*, 2718.

(171) Seo, K.; Borguet, E. *Langmuir* **2006**, *22*, 1388.

(172) Rosa, L. G.; Liang, J. *Journal of Physics-Condensed Matter* **2009**, *21*.

(173) Piner, R. D.; Zhu, J.; Xu, F.; Hong, S. H.; Mirkin, C. A. *Science* **1999**, *283*, 661.

(174) Smith, R. K.; Lewis, P. A.; Weiss, P. S. *Progress in Surface Science* **2004**, *75*, 1.

(175) Salaita, K.; Wang, Y. H.; Mirkin, C. A. *Nature Nanotechnology* **2007**, *2*, 145.

(176) Ivanisevic, A.; Mirkin, C. A. *Journal of the American Chemical Society* **2001**, *123*, 7887.

(177) Li, Y.; Maynor, B. W.; Liu, J. *Journal of the American Chemical Society* **2001**, *123*, 2105.

(178) Maynor, B. W.; Li, Y.; Liu, J. *Langmuir* **2001**, *17*, 2575.

(179) Xu, D. G.; Watt, G. D.; Harb, J. N.; Davis, R. C. *Nano Letters* **2005**, *5*, 571.

(180) Bakshi, M. S.; Kaura, A.; Miller, J. D.; Paruchuri, V. K. *Journal of Colloid and Interface Science* **2004**, *278*, 472.

(181) Lapkowski, M.; Zak, J.; Kolodziej-Sadlok, M.; Guillerez, S.; Bidan, G. *Synthetic Metals* **2001**, *119*, 417.

(182) O'Neil, K. D.; He, H. M.; Keech, P.; Shoesmith, D. W.; Semenikhin, O. A. *Electrochemistry Communications* **2008**, *10*, 1805.

(183) Luo, J.; Jones, V. W.; Han, L.; Maye, M. M.; Kariuki, N. N.; Zhong, C. J. *Journal of Physical Chemistry B* **2004**, *108*, 9669.

(184) Fonseca, L.; Perez-Murano, F.; Calaza, C.; Rubio, R.; Santander, J.; Figueras, E.; Gracia, I.; Cane, C.; Moreno, M.; Marco, S. *Sensors and Actuators a-Physical* **2004**, *115*, 440.

(185) Ostadrahimi, A. H.; Dabringhaus, H.; Wandelt, K. *Surface Science* **2002**, *521*, 139.

(186) Stockle, R. M.; Suh, Y. D.; Deckert, V.; Zenobi, R. *Chemical Physics Letters* **2000**, *318*, 131.

(187) Pettinger, B.; Ren, B.; Picardi, G.; Schuster, R.; Ertl, G. *Physical Review Letters* **2004**, *92*.

(188) Hayazawa, N.; Inouye, Y.; Sekkat, Z.; Kawata, S. *Chemical Physics Letters* **2001**, *335*, 369.

(189) Ichimura, T.; Hayazawa, N.; Hashimoto, M.; Inouye, Y.; Kawata, S. *Physical Review Letters* **2004**, 92.

(190) Hayazawa, N.; Yano, T.; Watanabe, H.; Inouye, Y.; Kawata, S. *Chemical Physics Letters* **2003**, *376*, 174.

(191) Steidtner, J.; Pettinger, B. *Physical Review Letters* **2008**, 100.

(192) Zhang, W. H.; Yeo, B. S.; Schmid, T.; Zenobi, R. *Journal of Physical Chemistry C* **2007**, *111*, 1733.

(193) George, S.; Lipstman, S.; Goldberg, I. *Crystal Growth & Design* **2006**, *6*, 2651.

(194) Zhang, Y. Q.; Chen, P. L.; Ma, Y. P.; He, S. G.; Liu, M. H. *Acs Applied Materials & Interfaces* **2009**, *1*, 2036.

(195) Zeller, M. V.; Hayes, R. G. *Journal of the American Chemical Society* **1973**, *95*, 3855.

(196) Lavallee, D. K.; Brace, J.; Winograd, N. *Inorganic Chemistry* **1979**, *18*, 1776.

(197) de Jong, J. J. D.; Lucas, L. N.; Kellogg, R. M.; van Esch, J. H.; Feringa, B. L. *Science* **2004**, *304*, 278.

(198) Mateos-Timoneda, M. A.; Crego-Calama, M.; Reinhoudt, D. N. *Chemical Society Reviews* **2004**, *33*, 363.

(199) Berova, N.; Di Bari, L.; Pescitelli, G. *Chemical Society Reviews* **2007**, *36*, 914.

(200) Prins, L. J.; De Jong, F.; Timmerman, P.; Reinhoudt, D. N. *Nature* **2000**, *408*, 181.

(201) Hembury, G. A.; Borovkov, V. V.; Inoue, Y. *Chemical Reviews* **2008**, *108*, 1.

(202) Qiu, Y. F.; Chen, P. L.; Liu, M. H. *Journal of the American Chemical Society* **2010**, *132*, 9644.

(203) Mammana, A.; D'Urso, A.; Lauceri, R.; Purrello, R. *Journal of the American Chemical Society* **2007**, *129*, 8062.

(204) Wan, Q.; Zhang, N. L.; Liu, W. L.; Lin, C. L.; Wang, T. H. *Applied Physics Letters* **2003**, *83*, 138.

(205) Choi, S. H.; Elliman, R. G. *Applied Physics Letters* **1999**, *74*, 3987.

(206) Fan, Z. Y.; Dutta, D.; Chien, C. J.; Chen, H. Y.; Brown, E. C.; Chang, P. C.; Lu, J. G. *Applied Physics Letters* **2006**, 89.

(207) Cirelli, R. A.; Bude, J.; Houlihan, F.; Gabor, A.; Watson, G. P.; Weber, G. R.; Klemens, F. P.; Sweeney, J.; Mansfield, W. M.; Nalamasu, O. *Microelectronic Engineering* **2000**, *53*, 87.

(208) Baba, K.; Deguchi, T.; Yamaki, K.; Miyagi, M. *Electronics Letters* **1997**, *33*, 1062.

(209) Miyanishi, S.; Innami, K.; Naka, T.; Kitazawa, T.; Yagura, M.; Teraguchi, N.; Murakami, Y.; Takahashi, A. *Ieee Transactions on Magnetics* **2008**, *44*, 3360.

(210) Moriz, C.; Lehmann, B.; Meier, W. *Agrarforschung* **2008**, *15*, 288.

(211) Yoon, S. Y.; Kong, S. H.; Lee, H. S.; Lim, C. K.; Kim, H. J.; Oh, H. S.; Park, J. B.; Choa, S. H. *Physica Status Solidi C - Current Topics in Solid State Physics,* **2007**, *4,* 4520.

(212) Hong, J. H.; McMichael, I.; Chang, T. Y.; Christian, W.; Paek, E. G. *Optical Engineering* **1995**, *34*, 2193.

(213) Bashaw, M. C.; Heanue, J. F.; Aharoni, A.; Walkup, J. F.; Hesselink, L. *Journal of the Optical Society of America B-Optical Physics* **1994**, *11*, 1820.

(214) Gallo, J. T.; Verber, C. M. *Applied Optics* **1994**, *33*, 6797.

(215) Saikawa, J.; Kurimura, S.; Shoji, I.; Taira, T. *Optical Materials* **2002**, *19*, 169.

(216) Cumpston, B. H.; Ananthavel, S. P.; Barlow, S.; Dyer, D. L.; Ehrlich, J. E.; Erskine, L. L.; Heikal, A. A.; Kuebler, S. M.; Lee, I. Y. S.; McCord-Maughon, D.; Qin, J. Q.; Rockel, H.; Rumi, M.; Wu, X. L.; Marder, S. R.; Perry, J. W. *Nature* **1999**, *398*, 51.

(217) Strickler, J. H.; Webb, W. W. *Optics Letters* **1991**, *16*, 1780.

(218) Zhou, W. H.; Kuebler, S. M.; Braun, K. L.; Yu, T. Y.; Cammack, J. K.; Ober, C. K.; Perry, J. W.; Marder, S. R. *Science* **2002**, *296*, 1106.

(219) Beljonne, D.; Wenseleers, W.; Zojer, E.; Shuai, Z. G.; Vogel, H.; Pond, S. J. K.; Perry, J. W.; Marder, S. R.; Bredas, J. L. *Advanced Functional Materials* **2002**, *12*, 631.

(220) Rozhok, S.; Piner, R.; Mirkin, C. A. *Journal of Physical Chemistry B* **2003**, *107*, 751.

(221) Weeks, B. L.; Vaughn, M. W.; DeYoreo, J. J. *Langmuir* **2005**, *21*, 8096.

(222) Kern, W. *HandBook of Semiconductor Wafer Cleaning Technology- Science, Technology and Applications*; William Andrew: New York, 1993; pp 10.

(223) Zeira, A.; Chowdhury, D.; Maoz, R.; Sagiv, J. *Acs Nano* **2008**, *2*, 2554.

(224) Mandimutsira, B. S.; Ramdhanie, B.; Todd, R. C.; Wang, H. L.; Zareba, A. A.; Czemuszewicz, R. S.; Goldberg, D. P. *Journal of the American Chemical Society* **2002**, *124*, 15170.

(225) Ramdhanie, B.; Stern, C. L.; Goldberg, D. P. *Journal of the American Chemical Society* **2001**, *123*, 9447.

(226) Kerber, W. D.; Ramdhanie, B.; Goldberg, D. R. *Angewandte Chemie-International Edition* **2007**, *46*, 3718.

(227) Prokop, K. A.; de Visser, S. P.; Goldberg, D. P. *Angewandte Chemie-International Edition* **2010**, *49*, 5091.

(228) Young, T. *Philosophical Transactions of the Royal Society* **1805**, *95*, 65.

(229) Nakajima, A.; Hashimoto, K.; Watanabe, T. *Monatshefte Fur Chemie* **2001**, *132*, 31.

(230) Li, X. M.; Reinhoudt, D.; Crego-Calama, M. *Chemical Society Reviews* **2007**, *36*, 1350.

(231) Yektafard, M.; Ponter, A. B. *Journal of Adhesion Science and Technology* **1992**, *6*, 253.

(232) Liao, K. S.; Wan, A.; Batteas, J. D.; Bergbreiter, D. E. *Langmuir* **2008**, *24*, 4245.

(233) Liao, K. S.; Fu, H.; Wan, A.; Batteas, J. D.; Bergbreiter, D. E. *Langmuir* **2009**, *25*, 26.

(234) Zhang, Y.; Furyk, S.; Sagle, L. B.; Cho, Y.; Bergbreiter, D. E.; Cremer, P. S. *Journal of Physical Chemistry C* **2007**, *111*, 8916.

(235) Nishio, Y.; Chiba, R.; Miyashita, Y.; Oshima, K.; Miyajima, T.; Kimura, N.; Suzuki, H. *Polymer Journal* **2002**, *34*, 149.

(236) Bauduin, P.; Wattebled, L.; Schrodle, S.; Touraud, D.; Kunz, W. *Journal of Molecular Liquids* **2004**, *115*, 23.

(237) Fu, H.; Hong, X. T.; Wan, A.; Batteas, J. D.; Bergbreiter, D. E. *Acs Applied Materials & Interfaces* **2010**, *2*, 452.

(238) Petkov, V. *Materials Today* **2008**, *11*, 28.

VITA

Albert Wan

Department of Chemistry, B2001, TAMU College Station, TX 77843

awan@mail.chem.tamu.edu

Education:

Ph.D., Chemistry, Texas A&M Uinversity, 2011
M.S., Chemistry, National Tsing-Hua University, Taiwan 2004
B.S., Chemistry, National Chung-Hsing University, Taiwan, 2002

Publication:

"Preparation, Size Control, Surface Deposition, and Catalytic Reactivity of Hydrophobic Corrolazine Nanoparticles in an Aqueous Environment." K. Cho, W. D. Kerber, S. R. Lee, A. Wan, J. D. Batteas, D. P Goldberg. *Inorganic Chemistry,* 49, 8465 (2010)

"Parallel Effects of Cations on PNIPAM Graft Wettability and PNIPAM Solubility." H. Fu, XT. Hong, A. Wan, J. D. Batteas, D. E. Bergbreiter. *ACS Applied Material & Interfaces,* 2, 452 (2010).

"Designing Surfaces with Wettability That Varies in Response to Solute Identity and Concentration." KS. Liao, H. Fu, A. Wan, J. D. Batteas, D. E. Bergbreiter. *Langmuir* 25, 26 (2009)

"Superhydrophobic Surfaces Formed Using Layer-by-layer Self-assembly with Aminated Multiwall Carbon Nanotubes." KS. Liao, A. Wan, J. D. Batteas, D. E. Bergbreiter. *Langmuir* 24, 4245 (2008)

Honors and Awards:

2009	Graduate Student Research and Presentation Grant
2007	2nd place & Session winner at the Annual Student Research Week, Texas A&M University